# Liquid Crystal State NMR Quantum Computing - Characterization, Control and Certification

by

Denis-Alexandre Trottier

A thesis
presented to the University of Waterloo
in fulfilment of the
thesis requirement for the degree of
Master of Science
in
Physics - Quantum Information

Waterloo, Ontario, Canada, 2013

I hereby declare that I am the sole author of this thesis. This is a true copy of the thesis, including any required final revisions, as accepted by my examiners.

I understand that my thesis may be made electronically available to the public.

# Abstract

Quantum computers offer the possibility of solving some problems more efficiently than their classical counterparts. The current forerunner in the experimental demonstration of quantum algorithms is Nuclear Magnetic Resonance (NMR). Known for its implementations at liquid state, NMR quantum computing consists of computing on nuclear spins. In the liquid crystal state, dipolar couplings are available, offering an increased clock frequency and a faster recycling of algorithms. Here investigated is the cost at which this comes, namely, a more complicated internal Hamiltonian, making the system harder to characterize and harder to control. In this thesis I present new methods for characterizing the Hamiltonian of dipolar coupled spin systems, and I report experimental results of characterizing an oriented 6-spin system. I then present methods and results concerning the quantum optimal control of this same spin system. Finally, I present experiments and simulations regarding the certification of computational quantum gates implemented in that same dipolar coupled spin system.

# Acknowledgments

Firstly, I would like to sincerely thank Prof. Raymond Laflamme for giving me the opportunity to be part of his research group at the Institute for Quantum Computing. I learned so much during this journey which was transformative at so many levels.

I bear much gratitude to Dr. Jingfu Zhang, my partner in science. Jingfu performed most of the experiments presented in this work. I personally was responsible for the simulations, the design of the experiments, finding the pulse sequences, and analyzing the experimental data. Jingfu also offered me the chance to join the project on Hamiltonian characterization presented in chapter 3. In that chapter, the experimental method to obtain simplified spectra is his idea, and the spectral analysis method is mine. The results presented in that chapter where also discussed with Prof. Raymond Laflamme and Mike Ditty. I also thank SHARCNET for having allowed me to use their clusters to find the pulse sequences presented in chapter 4. In addition, I want to thank Dr. Osama Moussa and Prof. Joseph Emerson for discussions that helped me to understand the twirling certification protocol presented in chapter 5. I must also thank Dr. Jingfu Zhang, Jun Li and Dawei Lu for their help in performing the experiments presented in that chapter.

I am also thankful to Prof. Kevin Resch and Prof. Joseph Emerson for agreeing to be on my defence committee. In addition, I want to thank my teachers, Prof. Raymond Laflamme, Prof. Richard Cleve, and Prof. David Cory. I feel indebted for having had this opportunity to learn quantum information theory from such world's leading scientists.

I would like to acknowledge financial support from Prof. Raymond Laflamme, the Natural Sciences and Engineering Research Council of Canada, the University of Waterloo, and the Fonds Québécois de la Recherche sur la Nature et les Technologies. I feel deeply privileged for this funding which allowed to fully focus on my research.

*To all those who shine light into the dark corners of our understanding.*

# Contents

# List of Tables

# List of Figures

# List of Algorithms

# Chapter 1

# Introduction and Motivation

Astonishing theoretical successes like prime factorization [1] and unsorted database search [2] are powerful motivations to pursue the implementation of Quantum Information Processing (QIP). Although their theoretical power is widely recognized, quantum algorithms can be quite tedious to implement in practice, and the quantum information processing potential of many different physical systems has thus been studied in recent years [3]. The current forerunner in the experimental demonstration of quantum algorithms is Nuclear Magnetic Resonance (NMR). In NMR, a sample of identical molecules is dissolved in a solvent and subject to a strong static magnetic field along the $z$-axis. The molecules are the framework of coupled spins which form the qubits. Currently, NMR quantum computing is mainly known for its implementations at liquid state, *i.e.* with isotropic solvents. For isotropic solvents, mutual couplings among the spins are provided by the scalar couplings. On the other hand, for liquid crystal solvents, the intramolecular dipolar couplings, which have larger magnitudes and longer ranges, survive due to molecular alignment, and lead to a finite number of sharp well resolved spectral lines, making it possible to use such systems for NMR-QIP. More importantly, the liquid crystal state offers an increased clock frequency, and shorter spin-lattice relaxation times which allow for faster recycling of algorithms [5]. At which cost do these advantages come? In simple terms, the advantages offered by dipolar couplings come to the cost of a more complicated internal Hamiltonian, making the system harder to characterize and harder to control in practice.

Why do dipolar couplings make the internal Hamiltonian so more difficult to handle in practice? For strongly coupled spins, the Zeeman and the coupling parts of the Hamiltonian do not commute, and the eigenstates are therefore obtained as linear combinations of product states. In this case, individual spins cannot be treated as qubits, but the $2^N$ eigenstates of a strongly coupled $N$-spin system can still be considered as an $N$ qubit system by using transition selective pulses to construct unitary transformations [6].

Usage of strongly coupled systems for quantum information processing thus requires the consistent labelling of energy levels, which can be achieved by a traditional Z-COSY experiment [4]. Using this approach, the implementation of logic gates, preparation of pseudo-pure states, creation of entanglement, and entanglement transfer have already been experimentally demonstrated in these systems [4, 6]. However, the study of how effectively the evolution under the internal Hamiltonian can be manipulated to implement quantum algorithms is strongly lacking. This research is currently facing serious problems such as the extreme difficulty of measuring the natural Hamiltonian in the first place, and the issue of global coherent control in strongly coupled systems, for which single spin addressability is usually lost. Measuring the Hamiltonian of spin systems dissolved in liquid crystals is currently a hard problem mainly due to the spectral complexity, which exponentially increases with the number of spins. In addition, theoretical calculations and first-order spectral analysis for estimating the dipolar couplings are usually not possible. Traditional spectroscopic methods could be used to obtain the Hamiltonian by spectral fitting. In practice, the fit has to be aided by estimating the solute degree of orientational order, based on phenomenological size and shape models. However, for molecules that are suitable for NMR-QIP, *a priori* knowledge is rarely available, and their structures need to be asymmetric. The problem is thus exacerbated and new methods are required. The goal of this thesis is to present methods that address the issues of Hamiltonian characterization and quantum control for dipolar coupled spin systems. We also present and apply methods for certifing experimental implementations of quantum gates in these systems. In principle, the methods presented in this work apply for dipolar coupled spin systems in general. In this thesis we will be working with the dipolar coupled 6-spin system of 2,3-Difluorobenzaldehyde, which consists of fours protons and two fluorines.

We start in chapter 2 by presenting the background material required to understand liquid crystal state NMR-QIP. By the end of that chapter, the reader should be able to understand and simulate the NMR experiments relevant to this work. We first start by discussing spin objects, and show how they can be used for purpose of quantum information processing. Then, we present how the quantum states of such systems are described in the density operator formalism. The spin-½ interactions, the natural Hamiltonian and the control Hamiltonian in liquid crystal state NMR are then presented. Next, we present the dynamical evolution of spin systems under their natural and control Hamiltonians. Then, we explain a few principles of NMR spectroscopy, and we show how NMR experiments can be simulated on a classical computer. This last part is especially important since we will mainly rely on simulations in order to characterize the natural Hamiltonian and also to design the control Hamiltonian. Finally, we present two experimental methods to simplify NMR spectra, and also one method for preparing a 2-qubit pseudo-pure state.

Chapter 3 addresses the problem of characterizing the natural Hamiltonian of dipolar coupled spin systems. This challenging task is of crucial importance for purpose of quantum information processing since current optimal control algorithms depend on the full information of the Hamiltonian. In that chapter, we propose a new method that addresses the issue of spectral analysis, and we report experimental results of extracting the parameters of the oriented 6-spin system of 2,3-Difluorobenzaldehyde. This is done without using *a priori* knowledge on the molecular geometry or order parameters. The advantages of our method are achieved with the use of a new spectral analysis algorithm, and by the use of simplified spectra obtained by transition selective pulses.

Then, in chapter 4 we address the problem of quantum optimal control for oriented spin systems. Then again, this task is much more difficult than in the case of isotropic solvents. In fact, for simple solutes dissolved in liquid state environments, control sequences to implement specific unitaries can often be written down by hand and optimized in a heuristic way. However, the situation is quite different when dipolar couplings are present, in which case the spectra are highly complicated and single spin addressability is usually lost. Sophisticated pulse sequence design algorithms have been developed in recent years for this kind of problems. The idea is to discretize the amplitudes of the control Hamiltonian into timesteps, and find a control sequence for a particular desired unitary using numerical optimization algorithms. In that chapter, we present the GRAPE (GRadient Ascent Pulse Engineering) algorithm. We also explain how to design experimentally robust pulses, and how the numerical search can be fasten using a subsystem approach. Moreover, we discuss the errors that occur in experimental implementations, and how pulse smoothing and pulse fixing can help to reduce these errors. Then, we present GRAPE pulses for single spin rotations, obtained for 2,3-Difluorobenzaldehyde. We start by considering the full 6-spin system, in which case pulse design is very challenging. Then, we present results for the proton subsystem decoupled from the fluorines.

Having a prototype quantum computing device in hand, we must now determine how faithful it is to an ideal quantum computer. In chapter 5, we present a well-known protocol for certifying experimental implementations of quantum gates. Rather than fully characterizing the experiments via quantum process tomography, we use a twirling protocol to estimate the average fidelity between the experimental and ideal operators. We start that chapter by introducing the notions of average fidelity and averaged quantum channel. Then, we present a method known as twirling, and we show how it can be used to measure the average fidelity for Clifford gates. Next, we present the usual statistical analysis to obtain bounds for the accuracy of the results. We also present our Monte Carlo approach in order to further investigate the accuracy of the twirling protocol. Finally, we apply the twirling protocol for certifying quantum gates implemented with 2,3-Difluorobenzaldehyde at liquid crystal state. We present simulated and experimental results.

# Chapter 2

# NMR of Spins-½ in Liquid Crystals

The spin is a property of particles. Particles having net spin-½ include the proton, neutron, electron, and quarks. As we will see, the dynamics of spin-½ objects can be described using quantum mechanics. In this chapter, we first present the concept of spin and we explain how atomic nuclei with non vanishing nuclear spin can be used for purpose of quantum information processing. Then, we explain how the quantum state of spin systems can be described via their density operator. Restraining ourselves to spin systems in anisotropic environments, *i.e.* liquid crystals, we next present the spin-½ interactions and we give the general natural Hamiltonian of such systems. In addition, we introduce the control Hamiltonian, generated using radio-frequency fields. We then present how the dynamical evolution of the density operator is driven by these Hamiltonians, and we also discuss the effect of decoherence. Then, we explain a few principles of Nuclear Magnetic Resonance (NMR) spectroscopy, and we show how NMR experiments can be simulated on a classical computer. Finally, we present two experimental methods to simplify NMR spectra, and also one method for preparing a 2-qubit pseudo-pure state.

## 2.1 Spin

In this section, we introduce the concept of *spin* and show how atomic nuclei with non vanishing nuclear spin can be used for purpose of quantum information processing. The spin of a particle is a form of quantum angular momentum. For elementary particles, the spin quantum number, denoted $S$, has a fixed value and is an intrinsic property of the particle. For bosons we have that $S$ is a integer, *i.e.* $S \in \{0, 1, 2, \dots\}$, and for fermions we have that $S$ is an half integer, *i.e.* $S \in \{1/2,\ 3/2,\ 5/2, \dots\}$. In general, particles with spin $S$ have $(2S+1)$ sublevels that are degenerated in the absence of an externally applied magnetic field. However, these sublevels may take different energy values if a magnetic field is applied. In the following, we explain how spins can be combined together.

Let us consider a system that is composed of two parts, each being a source of spin angular momentum, with quantum numbers $S_1$ and $S_2$. What is the spin quantum number $S_3$ of the combined system? According to quantum theory, the possible values for the total spin quantum number of the combined system are [7]

$$S_3 \in \{|S_1 - S_2|, |S_1 - S_2| + 1, \dots, |S_1 + S_2|\}. \tag{2.1}$$

Generally speaking, these different total spin states will have different energies, and each of them will behave like a new object with spin quantum number $S_3$. Two examples of such composite systems are the *neutron* and the *proton*, which are both composed of three spin-½ particles, named quarks, stuck together by gluons. In both cases, two of the quarks are antiparallel, implying that the total neutron and proton spins are both 1/2. In this work we are interested in atomic nuclei, which are composed of neutrons and protons.

An *atomic nucleus* is described by three numbers: the *atomic number* which specifies the number of protons inside the nucleus, the *mass number* which specifies the total number of protons and neutrons inside the nucleus, and the *nuclear spin quantum number* $I$ which specifies the total spin quantum number of the nucleus. Then again, the possible values that $I$ can take are given by applying Eq.(2.1). For instance, the $^2$H nucleus contains one proton and one neutron, implying that $I \in \{0, 1\}$. However, these two nuclear spin states have a large energy difference of $\sim 10^{11}$kJ mol$^{-1}$ [7]. For usual NMR experiments, the energies of excited states greatly exceed the energies available from electromagnetic fields. In general, the excited nuclear states may therefore be ignored in practice, and the value of $I$ is constrained be that of the lowest energy state, *i.e.* the ground state.

Let's consider a spin-½ nucleus. In the presence of a magnetic field, the two sublevels, denoted $|\alpha\rangle$ and $|\beta\rangle$, have different energies. The general state of the nucleus is of the form $\alpha|\alpha\rangle + \beta|\beta\rangle$, where $\alpha$ and $\beta$ are complex numbers such that $|\alpha|^2 + |\beta|^2 = 1$. In the next section, we show how to describe the state of an ensemble of spins-½ systems.

## 2.2 State representation

As explained above, spin systems require quantum mechanics to describe them. In fact, the concept of spin can be challenging to grasp beyond understanding how to manipulate the quantum mechanical equations. Therefore, we often rely on the abstract quantum notion of the density operator to describe the state of such spin objects [7]. Since we are working in the framework of NMR experiments, we will consider *ensembles*, which are defined to be collections of independent and identical spins systems. Here, we first explain how the state of non-interacting spins-½ can be described by a density matrix, and we then extend this notion to interacting spins-½ .

Let's consider an ensemble of many (*e.g.* $\sim 10^{22}$) identical and non-interacting spins-½. Keeping track of the state of each individual spin is infeasible in practice, and one has to resort to some kind of statistical description of the ensemble. This is the spirit behind the density operator approach. This method can be understood from the properties of the expectation value of an observable. Consider a single spin in the state $|\psi\rangle$, it then follows that the expectation value of an operator $Q$ is given by $\langle Q\rangle = \langle\psi|Q|\psi\rangle$. Equivalently, one can use the trace operation to rewrite the expectation value as $\langle Q\rangle = \mathrm{tr}(|\psi\rangle\langle\psi|Q)$. Let's now suppose there are two independent (*i.e.* uncoupled) spins, respectively in states $|\psi_1\rangle$ and $|\psi_2\rangle$. Say we measure $Q$ on both spins and then add up the two measurements, the expectation value would be $\langle\psi_1|Q|\psi_1\rangle + \langle\psi_2|Q|\psi_2\rangle = \mathrm{tr}((|\psi_1\rangle\langle\psi_1| + |\psi_2\rangle\langle\psi_2|)\,Q)$. Extending this logic to $N$ independent spins, and defining the *density operator* $\rho$ as

$$\rho = N^{-1}(|\psi_1\rangle\langle\psi_1| + |\psi_2\rangle\langle\psi_2| + \cdots + |\psi_N\rangle\langle\psi_N|), \tag{2.2}$$

it follows that the average contribution of each spin to the macroscopic observation of $Q$ for the entire ensemble is given by $\mathrm{tr}(\rho\, Q)$. This motivates the use of the density operator when it comes to describe ensembles. According to the definition, we see that any density operator $\rho$ has to obey the following properties

i. $\mathrm{tr}(\rho) = 1$,
ii. $\mathrm{tr}(\rho^2) \leq 1$,
iii. $\rho = \rho^\dagger$,
iv. $\rho$ is positive semi-definite.

To further discuss the matrix form of the density operator, we shall introduce the *Pauli matrices* $\{I, X, Y, Z\}$, which are defined as

$$I = \begin{pmatrix} 1 & 0 \\ 0 & 1 \end{pmatrix}, \quad X = \begin{pmatrix} 0 & 1 \\ 1 & 0 \end{pmatrix}, \quad Y = \begin{pmatrix} 0 & -i \\ i & 0 \end{pmatrix}, \quad Z = \begin{pmatrix} 1 & 0 \\ 0 & -1 \end{pmatrix}. \tag{2.3}$$

One can see that the Pauli matrices form a basis such that any $2 \times 2$ complex matrix can be written as a linear combination of them. In particular, considering an ensemble of non-interacting spins-½, the density operator can always be written in the form

$$\rho = \frac{1}{2}I + \frac{p_x}{2}X + \frac{p_y}{2}Y + \frac{p_z}{2}Z, \tag{2.4}$$

where $p_x$, $p_y$ and $p_z$ are real numbers such that $p_x^2 + p_y^2 + p_z^2 \leq 1$, and are connected to the net polarization (or net alignment) of the spins along the $x$-, $y$- and $z$-axis respectively. These quantities are given by

$$p_x = \mathrm{tr}(X\rho), \qquad p_y = \mathrm{tr}(Y\rho), \qquad p_z = \mathrm{tr}(Z\rho). \tag{2.5}$$

To further establish the connection between the conceptual Hilbert space and the actual physical space, it is useful to represent the density matrix $\rho$ in the *Bloch sphere* representation. In the Bloch sphere representation, the state $\rho$ is represented by a point at coordinates $(p_x, p_y, p_z)$ in a unit sphere. States located on the surface of the sphere are called *pure states* and states located within the sphere and called *mixed states*.

The density operator method can be extended to describe the state of ensembles of $n$ interacting spins-½. First, one need to introduce the *product operators* $\{B_j\}_{j=0}^{4^n-1}$. These operators are defined to be tensor products of $n$ Pauli matrices. By convention, we have $B_0 := I^{\otimes n}$, and the other product operators are of the form

$$B_j \in \left\{ \bigotimes_{k=1}^{n} \sigma_k \mid \sigma_k \in \{I, X, Y, Z\} \right\}. \tag{2.6}$$

The product operators form a basis such that any $2^n \times 2^n$ complex matrix can be written as a linear combination of them. For ensembles of $n$ interacting spins, the density operator can in fact always be written in the form

$$\rho = \frac{1}{2^n}I^{\otimes n} + \sum_{j=1}^{4^n-1} \frac{p_j}{2^n} B_j. \tag{2.7}$$

Again, the $\{p_j\}$ are real numbers such that $\sum_j p_j^2 \leq 2^n - 1$, and are given by $p_j = \mathrm{tr}(B_j\rho)$.

In this section, we introduced the notion of density operator, which can be used to described the state of an ensemble of non-interacting or interacting spins-½. We also discussed the matrix form of the density operator. In the following section, we present the natural and control Hamiltonians in liquid crystal state NMR. These drive the dynamical evolution of the spins-½ systems on which they are acting.

## 2.3 Hamiltonians in liquid crystal state NMR

In the framework of quantum mechanics, *Hamiltonians* are used to describes interactions. Consequently, the dynamics of quantum systems, such as interacting spins-½, is dictated by their Hamiltonian. In the NMR experiments under consideration here, the situation is that of an ensemble of identical molecules dissolved in an environment, and subject to a static homogenous magnetic field along the $z$-axis. The molecules are the frameworks within which the interacting spins are trapped, and the molecular structure thus shapes the interactions between the spins. As for the solvent, its state of matter determines the molecular mobilities, possibly averaging out certain molecular interactions. In this section, we explore spin-½ interactions, and the natural Hamiltonian that results for liquid crystal solvents. We also present the control Hamiltonian, generated via the use of radio-frequency fields.

### 2.3.1 Molecules & the liquid crystal state

A *molecule* is an electron cloud containing more than one nucleus, and is in fact the framework inside which the nuclear spins are trapped. The particular geometric configuration of a molecule is determined by the quantum mechanical motion of the electrons. Very often, the motion of molecules can be treated classically, by which we mean that ignoring the quantum nature of molecular motion almost always gives reasonable answers [7]. Most importantly, the molecular mobilities depend on the environment, *i.e.* the solvent, and greatly affect the spin dynamics by possibly averaging out certain spin interactions.

When dissolved into a *liquid crystal*, *i.e.* an anisotropic liquid, the molecules adopt a non-isotropic spatial configuration, meaning that the molecular mobilities depend on the direction in space. In nematic phase liquid crystals (see Figure 2.1), the molecules are shape like ellipses and, on average, they are aligned in space along a particular direction called the *director*. In nematic phase liquid crystals, it is thus easier for the molecules to rotate along an axis parallel to the director than around an axis perpendicular to the director. As a consequence of this motional anisotropy, the dipolar interactions, which would have been averaged out in the liquid state, remain present in the liquid crystal state, leading to much more complicated NMR spectra. Despite this configuration, the molecules are still very mobile and the substance flows under shear forces, leading to averaging out intermolecular interactions [7]. Thus, the dynamics of spins systems dissolved in liquid crystals is driven by the interactions of each single spin with the other spins within the same molecule, and by the interactions between the spins and the external magnetic field.

### 2.3.2 Spin-½ interactions & the natural Hamiltonian

We are now interested in spin-½ interactions, which are electromagnetic in nature. From these interactions, we will derive the natural Hamiltonian for interacting spins-½ in liquid crystal state environments. We will also briefly introduce the control Hamiltonian.

Let's consider the interaction of a single nucleus with electric and magnetic fields. The nucleus interacts with the electric field via its electric charge, and it interacts with the magnetic field via its magnetic moment. The nuclear spin Hamiltonian thus contains two parts: an electric part, which describes how the nuclear electric energy changes as the nucleus rotates, and a magnetic part, which describes how the nuclear magnetic energy changes as the nucleus rotates. For spin-½ nuclei, it can be shown that the electric spin Hamiltonian vanishes because the nuclear electric energy is independent of the orientation of the nucleus in space [7]. On the other hand, the magnetic spin Hamiltonian is still present. Let's consider that a static and homogenous strong magnetic field is present along the $z$-axis. The large interactions with the high magnetic field tend to mask some parts of the internal spin interactions, and we can thus use the so-called *secular approximation*.

The interaction of spin $j$ 's magnetic dipole with the externally applied static magnetic field along the $z$-axis is represented by the Hamiltonian $\mathscr{H}_j^Z$ and is given by $\mathscr{H}_j^Z = \frac{\omega_j^L}{2} Z_j$, where $\omega_j^L$ is called the *Larmor frequency*, and $Z_j$ denotes the Pauli matrix $Z$ at spin location $j$. In practice, this part of the Hamiltonian vanishes due to the fact that we are working in the *rotating frame* [7, 8], *i.e.* the frame rotating at the Larmor frequency.

The Hamiltonian $\mathscr{H}_j^{CS}$ is due to the disturbance of the orbital motion of nearby electrons inducing a magnetic field that adds to the external one and results in shifting the Larmor frequency of spin $j$ by a quantity $2\pi\nu_j$, called *offset frequency* [7, 8],

$$\mathscr{H}_j^{CS} = \pi \nu_j Z_j. \tag{2.8}$$

The Hamiltonian $\mathscr{H}_{jk}^{DD}$ is due to the direct spin-spin coupling via the dipolar interaction, which is characterized by the the dipolar coupling constant $D_{jk}$ [7, 8],

$$\mathscr{H}_{jk}^{DD} = \frac{\pi D_{jk}}{2} \times \begin{cases} 2Z_jZ_k, & \text{if heteronuclear,} \\ (2Z_jZ_k - X_jX_k - Y_jY_k), & \text{if homonuclear,} \end{cases} \tag{2.9}$$

where the $X_jX_k$ and $Y_jY_k$ terms are averaged out in the heteronuclear case due to the large gap between the Larmor frequency of different species [7]. The same holds below.

The Hamiltonian $\mathscr{H}_{jk}^{J}$ is due to the indirect electron-mediated interaction, which is characterized by the scalar coupling constant $J_{jk}$ [7, 8],

$$\mathscr{H}_{jk}^{J} = \pi J_{jk} \times \begin{cases} Z_jZ_k, & \text{if heteronuclear,} \\ (Z_jZ_k + X_jX_k + Y_jY_k), & \text{if homonuclear.} \end{cases} \tag{2.10}$$

The expression of the internal Hamiltonian can then be obtained by adding up these parts for each spins in the molecule, and the natural Hamiltonian thus has the form

$$\mathscr{H}^{nat} = \sum_j \mathscr{H}_j^{CS} + \sum_{j,k>j} \left(\mathscr{H}_{jk}^{DD} + \mathscr{H}_{jk}^{J}\right). \tag{2.11}$$

In this expression, the intermolecular interactions are neglected. In fact, additional terms should be present to take into account those interactions that lead to decoherence. The spin-½ interactions are summarized in Figure 2.1. In addition to the static magnetic field, transverse electromagnetic fields can be applied to control the state of the ensemble. These transverse fields generate the control Hamiltonian, which is next presented.

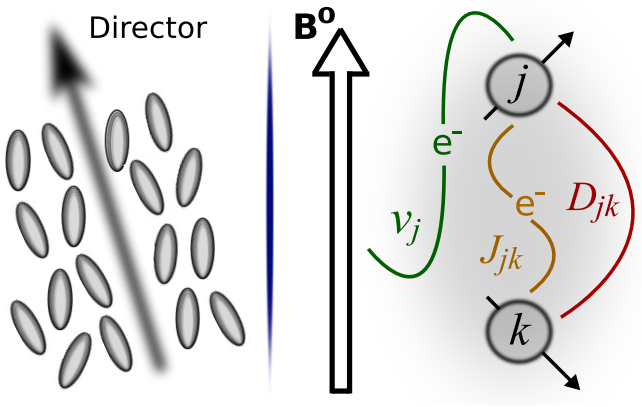


Figure 2.1: **(Left)** Alignment of the molecules along the director in nematic phase liquid crystals. **(Right)** Pictorial representation of the spin interactions.

### 2.3.3 Control Hamiltonian

In principle, quantum control of interacting spins-½ can be implemented by applying radio-frequency (r.f.) fields perpendicularly to the static field. By applying these fields, we can induce transitions whose frequency is resonant with the r.f. field. In practice, each isotope requires his own spectrometer's channel, each of which need an amplifier to achieve control. In the rotating frame, the control Hamiltonian thus has the form [7, 8]

$$\mathscr{H}^{C}(t) = \sum_m \left( x_m(t) \sum_{l_m} X_{l_m} + y_m(t) \sum_{l_m} Y_{l_m} \right), \tag{2.12}$$

where $m$ indexes the different isotopes, and $l_m$ indexes the nuclear spins of isotope $m$. The control amplitudes $x_m(t)$ and $y_m(t)$ are discretized into timesteps, and the sequences for a particular desired unitary evolution are found using the GRAPE algorithm [9], which is explained in details in chapter 4. In the next section, we explain how the state of interacting spins-½ evolve under the natural Hamiltonian, and also in the presence of a control Hamiltonian. This will allow us to understand and simulate NMR experiments.

## 2.4 Time evolution

Here, we first present how the state of spins-½ systems evolves under their natural Hamiltonian, and we then present time evolution in the presence of a control Hamiltonian. The material discussed here will allow us to understand and simulate NMR spectra of spins-½ systems, which is the topic of the next section.

Consider some Hamiltonian $\mathscr{H}(t)$. According to quantum mechanics, the dynamical evolution of the density operator $\rho$ obeys the Schrödinger equation (with $\hbar = 1$)

$$\dot{\rho} = -i[\mathscr{H}(t), \rho(t)], \tag{2.13}$$

where $[A, B] = AB - BA$ is the commutator of matrices $A$ and $B$. This differential equation can be integrated from time $t_0$ to time $t$ to give a solution of the form

$$\rho(t) = U(t, t_0)\rho(t_0)U^\dagger(t, t_0), \tag{2.14}$$

where $\rho(t_0)$ is the density matrix at time $t_0$, and $U(t, t_0)$ is called the *propagator*, calculated by integrating the instantaneous propagator,

$$\begin{aligned} U(t, t_0) &= \sum_{n=0}^{\infty}(-i)^n \int_{t_0}^{t} dt_1 \int_{t_0}^{t_1} dt_2 \ldots \int_{t_0}^{t_{n-1}} dt_n \mathscr{H}(t_1)\mathscr{H}(t_2)\ldots\mathscr{H}(t_n) \\ &:= \mathcal{D}\exp\left[-i\int_{t_0}^{t}\mathscr{H}(\tau)d\tau\right], \end{aligned} \tag{2.15}$$

where $\mathcal{D}$ denotes the Dyson time ordering operator. Let us first consider the specific case where only the natural Hamiltonian is present, *i.e.* $\mathscr{H}(t) = \mathscr{H}^{nat}$.

### 2.4.1 Free evolution

We consider here the case of *free evolution*, which is when only the natural Hamiltonian is present. The total Hamiltonian of the system is thus given by $\mathscr{H}(t) = \mathscr{H}^{nat}$, and is therefore constant in time. One can easily see that Eq.(2.15) then takes the form

$$U(t, t_0) = \exp\left[-i\mathscr{H}^{nat}(t - t_0)\right]. \tag{2.16}$$

Let $\{\Omega_k\}$ and $\{|k\rangle\}$ respectively denote the eigenvalues and corresponding eigenvectors of the natural Hamitonian $\mathscr{H}^{nat}$, it can then be shown that the time evolution of the coherence $\rho_{rs}(t) = \langle r|\rho(t)|s\rangle$ takes the following form [7]

$$\rho_{rs}(t) = \rho_{rs}(t_0)\exp\left[-i(\Omega_r - \Omega_s)(t - t_0)\right]. \tag{2.17}$$

The Hamiltonian 2.11 doesn't take *decoherence* into account. Each molecule is in fact not totally decoupled from the rest of the environment and a damping decay constant $\lambda_{rs}$ must be included to account for relaxation [7], leading to an actual evolution of the form

$$\rho_{rs}(t) = \rho_{rs}(t_0) \exp\left[(-i(\Omega_r - \Omega_s) - \lambda_{rs})(t - t_0)\right]. \tag{2.18}$$

The free evolution is thus fairly simple to understand. However, the dynamics become more complicated in the presence of the control Hamiltonian $\mathscr{H}^C(t)$, which was previously introduced, due to the fact that the total Hamiltonian becomes piecewise constant in time. We consider this case in the following.

### 2.4.2 Controlled evolution

We now consider the case where a control Hamiltonian $\mathscr{H}^C(t)$ is present. The total Hamiltonian of the system is thus given by $\mathscr{H}(t) = \mathscr{H}^{nat} + \mathscr{H}^C(t)$. We mentioned that in practice, $\mathscr{H}^C(t)$ is approximately piecewise constant in time. Hence, it follows that $\mathscr{H}(t)$ is also approximately piecewise constant in time. In other words, the evolution from time $t_0$ to time $t$ is divided into $N$ intervals of length $\Delta t$, and for each timestep $j$ the Hamiltonian $\mathscr{H}(t_j)$ is constant. Thus, the propagator for timestep $j$ is given by

$$U_j = \exp\left[-i\mathscr{H}(t_j)\Delta t\right]. \tag{2.19}$$

The complete unitary $U(t, t_0)$ is then obtained by multiplying all the $U_j$ together,

$$U(t, t_0) = \prod_{j=0}^{N-1} U_j. \tag{2.20}$$

At this point, a relevant question might be asked: do we have complete control? In other words, can the full Hilbert space be explored? There is a simple and intuitive result for this question. In fact, it can be shown that we can fully control any system in which arbitrary single qubit rotations can be implemented and with a two body coupling Hamiltonian connecting all qubits [10]. In practice, achieving quantum control is a serious challenge. The control Hamiltonian as to be engineered using very sophisticated numerical optimization algorithms. Moreover, as we will discuss in chapter 4, for dipolar coupled systems, numerical brute force quickly becomes insufficient as the number of qubit increases, and one has to develop strategies to help the numerical search.

In the following section, we present the basic principles of NMR spectroscopy, and we show how to calculate NMR spectra from the density matrix. This will be very useful in chapter 3, where we will be challenged with the problem of extracting the parameters of the Hamiltonian from NMR thermal spectra.

## 2.5 The NMR experiment

Later, in chapter 3, we will address the problem of extracting the parameters of the natural Hamiltonian from NMR thermal spectra. This will be achieved using home-made computer programs that analyze NMR spectra. In practice, we use methods to simplify the spectra, these are presented in the next section. In this section, we show how to calculate NMR spectra, but first we introduce the NMR thermal equilibrium state.

### 2.5.1 Thermal equilibrium

In NMR, the *thermal equilibrium* state of the system is the maximally mixed state with a small deviation that is due to the externally applied magnetic field which breaks the isotropy of the magnetization distribution and causes the sample to acquires a small net magnetic moment along the external field, *i.e.* along the $z$-axis [7, 8]. Considering an ensemble of $n$-spin systems, the thermal state is described by the density matrix [7]

$$\rho_{th}^{full} = \frac{1}{2^n} I^{\otimes n} + \epsilon \sum_j \gamma_j Z_j, \tag{2.21}$$

where $\gamma_j$ is the gyromagnetic ratios of spin $j$, and $\epsilon$ is a small constant ($\sim 10^{-5}$) depending on the magnitude of the field and the temperature. In an NMR experiment, the identity term is unobservable and unchanged by the dynamics. It is therefore typically dropped and only the second term, called the *deviation density matrix*, is written down. In NMR, the deviation density matrix at thermal equilibrium thus has the following form

$$\rho_{th} \propto \sum_j Z_j. \tag{2.22}$$

By applying an oscillating magnetic field (*r.f. pulse*) of appropriate frequency and duration, the polarization of every single spin can be rotated by an angle $\pi/2$ around the $y$-axis, the macroscopic magnetization is then along the $x$-axis and the deviation density matrix, at time $t = 0$, thus has the form

$$\rho(0) \propto \sum_j X_j. \tag{2.23}$$

The system is then allowed to evolve freely over a time interval $t$. The NMR spectrometer has a set of independent frequency channels, allowing one to access a small number of narrow frequency windows, each of which may be centred on a different reference frequency. By tuning the channels of the different nuclear species around their Larmor frequencies, one is effectively observing the different nuclear species in their respective rotating-frame and the time evolution is given by Eq.(2.18). We now show how to calculate NMR spectra.

### 2.5.2 NMR spectra

We start by describing the acquisition of the NMR signal. The interaction of the net magnetic moment of the sample with the external magnetic field results in the rotation of the macroscopic magnetization in the $xy$-plane. This transverse magnetization decays slowly since the spins gradually get out of phase with each other due to slight fluctuations of the microscopic magnetic fields on different spins. This precessing magnetization can be detected by coils along the $x$-axis and $y$-axis, and the oscillating electric current induced is called *free-induction decay* (FID). The signals along the $x$-axis and $y$-axis may be interpreted as the real and imaginary components of a single complex signal of the form

$$s(t) = s_x(t) - is_y(t), \tag{2.24}$$

where $s_x(t)$ and $s_y(t)$ are respectively the signals along the $x$- and $y$-axis. The quantum mechanical observable associated to the measurement of this signal is given by

$$O = \frac{1}{2}\sum_j \left(X_j - iY_j\right), \tag{2.25}$$

where the summation is over all observed spins. The measured signal is then given by [7]

$$\begin{aligned} s(t) \propto \langle O\rangle = \mathrm{tr}(\rho(t)O) &= \sum_r\sum_s \langle r|\rho(t)|s\rangle\langle s|O|r\rangle \\ &= \sum_r\sum_s \rho_{rs}(t)O_{sr} \\ &= \sum_r\sum_s \rho_{rs}(0)O_{sr}\exp\{[i\Omega_{rs} - \lambda_{rs}]t\}, \end{aligned} \tag{2.26}$$

where $\Omega_{rs} := -\Omega_r + \Omega_s$ and $O_{sr} := \langle s|O|r\rangle$, and where $\{\Omega_k\}$ and $\{|k\rangle\}$ respectively denote the eigenvalues and eigenvectors of the natural Hamitonian. The NMR spectrum is the the Fourier transform of the signal $s(t)$, and takes the form [7]

$$S(\Omega) = \int_0^\infty s(t)\exp\{-i\Omega t\}dt \quad \propto \quad \sum_r\sum_s a_{rs}\left(\frac{1}{\lambda_{rs} + i(\Omega - \Omega_{rs})}\right), \tag{2.27}$$

where $\Omega$ is the frequency, and $a_{rs}$ is the amplitude of the transition between energy levels $r$ and $s$, and given by [7]

$$a_{rs} = \rho_{rs}(0)O_{sr}. \tag{2.28}$$

The above equations show us how to simulate NMR spectra. In particular, we can start thinking about using spectral fitting to extract the parameters of the natural Hamiltonian from NMR thermal spectra. These approaches are discussed in chapter 3. In the next section, we present a few experimental methods that we will use later.

## 2.6 Additional experimental methods

In this section we present a few experimental methods that we will use later in this work. The first two methods are to simplify spectral analysis. The third method shows how we can prepare a pseudo-pure state for a 2-qubit system.

### 2.6.1 Heteronuclear decoupling

Consider a molecule with two species of nuclei: $^1$H and $^{19}$F. Then, there exists a simple method, called *heteronuclear decoupling* [7], to eliminate the heteronuclear couplings and thus simplify spectral analysis. To eliminate the $^1\text{H} - {}^{19}\text{F}$ splitting from $^1$H spectra, one has to acquires the $^1$H NMR signal at the same time as applying an r.f. field at the $^{19}$F Larmor frequency. This is illustrated in Figure 2.2. The $^1\text{H} - {}^{19}\text{F}$ couplings are then averaged out as a result [7]. The same technique can be used to eliminate the $^1\text{H} - {}^{19}\text{F}$ splitting from the $^{19}$F spectra, but by applying the r.f. field on the $^1$H nuclei.

### 2.6.2 Transition selection

In this work, we propose another method to further simplify spectral analysis of heteronuclear systems. The starting point is the fact that it is experimentally possible to excite specific transitions. To do this, one needs to apply a long low-power pulse. To help visualize this, one just have to look at the Fourier transformed sine function

$$\text{FT}[\sin(2\pi\nu_0 t)] = \frac{i}{2}[\delta(\nu+\nu_0) - \delta(\nu-\nu_0)], \tag{2.29}$$

where $\delta(x)$ is the Dirac delta function. One can see that as $\nu_0$ get smaller, the region excited in the frequency domain also gets smaller. The scheme to simplify spectral analysis then goes as follow: a decoupling pulse is applied while exciting a particular transition. The decoupling is then stopped and the excited transition is acquired. Many of those experiments can be done, allowing us to break the full spectrum into subspectra.

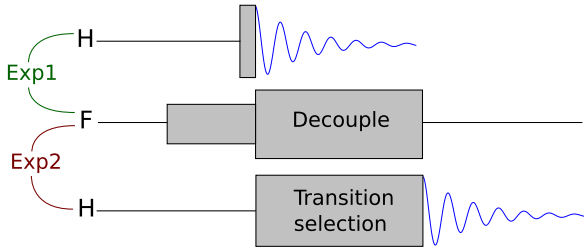


Figure 2.2: Experimental methods to simplify spectral analysis. Heteronuclear decoupling is illustrated as Exp1, and transition selection is illustrated as Exp2. These methods will be used later to simplify spectral analysis and measure the natural Hamiltonian.

### 2.6.3 2-qubit pseudo-pure state preparation

Here, we present a simple method for preparing a pseudo-pure state in a 2-qubit system. The starting point is the observation that the state $|00\rangle\langle 00|$ can be written as

$$|00\rangle\langle 00| = \frac{1}{4}\left(I^{\otimes 2} + Z_1 + Z_2 + Z_1 Z_2\right). \tag{2.30}$$

Therefore, if we can prepare the state's deviations $Z_1$, $Z_2$ and $Z_1 Z_2$, we can prepare a state with deviation proportional to $|00\rangle\langle 00|$. How can we prepare $Z_1$ and $Z_2$? Starting from the thermal state, one can rotate the first spin by $-\pi/2$ around the $x$-axis,

$$Z_1 + Z_2 \to Y_1 + Z_2. \tag{2.31}$$

The first spin can also be rotated by $\pi/2$ instead,

$$Z_1 + Z_2 \to -Y_1 + Z_2. \tag{2.32}$$

We can then add the result of these two experiments to obtain $Z_2$. Obviously, can also obtain $Z_1$ using a similar strategy. Therefore, we can prepare $Z_1$ and $Z_2$. To prepare $Z_1 Z_2$, we start from $Z_1$ and then rotate the first spin by $-\pi/2$ around the $x$-axis,

$$Z_1 \to Y_1. \tag{2.33}$$

We then apply a pulse with propagator given by $e^{iZ_1 Z_2 \pi/4}$,

$$Y_1 \to X_1 Z_2. \tag{2.34}$$

Finally, we rotate the first spin such that

$$X_1 Z_2 \to Z_1 Z_2. \tag{2.35}$$

Thus, we are also able to prepare $Z_1 Z_2$. In practice, we will use this method later when we will certify the experimental implementation of quantum gates in a 2-qubit system.

This marks the end of the first chapter. We have first introduced the concept of spin, and we then explained how the quantum state of spin systems can be described using the density operator approach. We have also presented the spin-½ interactions and we have given the natural and control Hamiltonians in liquid crystal state NMR. Then, we have shown how spin systems evolve under these Hamiltonians. Using this and a few notions of NMR spectroscopy, we have then derived the equations to calculate NMR spectra. Finally, we presented two methods to simplify experimental spectra, and also a method for preparing a 2-qubit pseudo-pure state. In the next chapter, we present and discuss methods for measuring the natural Hamiltonian of dipolar-coupled spin systems.

# Chapter 3

# Characterization of the Hamiltonian

In order to control a spin system for purpose of quantum information processing, measuring its natural Hamiltonian is of critical importance due to the fact that current optimal control algorithms depend on the full information of the Hamiltonian. How can we extract the Hamiltonian's parameters from experimentally measured data? Actually, characterizing the Hamiltonian of dipolar coupled spin systems is usually a difficult task due to the high complexity of their spectra. Currently, molecules with unknown geometrical structure and low symmetry are extremely tedious or impossible to analyze by sheer spectral fitting. In this chapter, we present a novel method that addresses the problem of spectral analysis, and report experimental results of extracting, by spectral fitting, the parameters of an oriented 6-spin system with very low symmetry in structure, without using *a priori* knowledge or assumptions on the molecular geometry or order parameters. The advantages of our method are achieved with the use of a new spectral analysis algorithm - NAFONS (Non-Assigned Frequency Optimization of Nmr Spectra), and by the use of simplified spectra obtained by transition selective pulses. The new method pushes the limit of spectral analysis for dipolar coupled spin systems, and is helpful for related fields, such as quantum computation and molecular structure analysis.

## 3.1 Introduction

Characterizing the Hamiltonian of a system by extracting parameters from experimentally measured data is a kind of inverse problem, one of fundamental problems in physics. In order to control a system, *e.g.* for purpose of quantum information processing [12], this task is critically important, because current optimal control algorithms, such as gradient ascent pulse engineering [9] and strongly modulating pulse [13] algorithms, depend on the full information of the Hamiltonian. In addition, the Hamiltonian of spin systems provides valuable information for molecular structure analysis [14].

In dipolar coupled spin systems, such as molecules dissolved in liquid crystals in NMR experiments [15], the Hamiltonian is not naturally diagonal due to the interaction terms with dipolar couplings, which are usually too strong for the weakly coupling approximation to be satisfied. Consequently, the spectra are usually very complex in multiple-spin systems, where the number of peaks corresponding to single coherence increases rapidly with the number of interacting spins. Furthermore, in liquid crystal solvents, the dipolar couplings depend on the solute's size and shape, and are scaled by the order parameters, which are sensitive to multiple factors, such as the characteristics of the solvents, magnetic fields, temperature, etc, making almost impossible the theoretical calculation for obtaining the dipolar couplings. Moreover, first-order analysis of dipolar coupled spectra is usually not possible, and the Hamiltonian has to be diagonalized numerically.

Measuring the parameters of dipolar coupled spins from NMR spectra is currently a hard problem. One approach, called pure frequency fitting [16–24], is to minimize by least squares the difference between the observable peak frequencies and the simulated transition frequencies. The well-known major drawback of this approach is the requirement of spectral assignment, a manual procedure to determine which experimental peak corresponds to which simulated transition. To avoid spectral assignment, the straightforward strategy is to fit the spectrum, directly obtained from the thermal state via nonselective pulses, using a least squares algorithm. This approach, called line shape fitting [28–34], is associated with immense computational resources and is seriously limited by the huge number of local minima. For this reason, evolutionary algorithms [35–39], which are able to search through many local minima, have been proposed and used for line shape fitting, with impressive but still limited success. In fact, these methods are unable to cope with a large search space, making them suitable mainly for molecules with high symmetry and accurately known geometrical structure [38]. For all of the above methods, proper initial guess and bounds of the parameters are thus required to approach the desired solution. Additional spectra are necessary for this purpose, where Z-COSY [40, 41] and homonuclear decoupling [42–46] techniques are helpful for obtaining crucial clues to estimate certain parameters. In addition, strategies based on multiple quantum coherence NMR [38, 47, 48]

have been developed to reduce the number of local minima, exploiting the fact that the number of higher order transitions is much less than the number of single order transitions. The high order transitions can be observed through 2D experiments. Implementation of such experiments requires to optimize the delay in the preparation period, and therefore usually requires a long measurement time. In addition, the resolution of the second dimension is usually low. Recently, theoretical strategies based on local control techniques were proposed through accessing the system partially, and an experimental demonstration was implemented in three spins with well known Hamiltonian using NMR [49–51].

In this chapter, we present Non-Assigned Frequency Optimization of Nmr Spectra (NAFONS), a pure frequency fit method in which spectral assignment is incorporated into a standard numerical optimization problem that can be addressed by a computer. Our global optimization strategy is based on the injection of random perturbations designed to enable the solver to escape local minima. Another way of thinking about our global optimization strategy is that we use multiple objective functions that have different local minima but that share the same global minimum. Thus, when we reach a local minimum we just have to switch to some other objective function, hoping that by repeating this process we will eventually reach the desired solution. The spectra to be fitted are obtained by standard 1D experiments. In experiment, we apply our algorithm to solve a 6-spin system with low symmetry in structure, without using knowledge on the interspin distances or order parameters, and even without a first-order estimation of the parameters. The parameters of the Hamiltonian are well estimated in a few minutes and with no operator intervention. In addition, our algorithm is compatible with the standard pure frequency fitting approach in the sense that both methods could be combined in a single unified algorithm. This is discussed later in this chapter. We also introduce an experimental method to simplify spectral analysis of heteronuclear systems. This method uses transition selective pulses in order to reduce the complete thermal spectrum into simpler sub spectra.

In the next section, we give the details of our NAFONS algorithm, which is a numerical optimization over the Hamiltonian parameters. We refer the reader to section 2.3.2 for the description of the natural Hamiltonian in liquid crystal state NMR. Given that the dipolar couplings are much larger (up to 2-3 order of magnitudes) than the scalar couplings, we thus firstly search for the $\{\nu_i, D_{ij}\}$, which are stored in a vector $\vec{x}$. We measure the scalar couplings in an isotropic solvent, *e.g.* chloroform, and then use them as initial guess in the anisotropic solvent to further adjust all the parameters. In principle, the fitting cannot distinguish heteronuclear scalar couplings from the corresponding dipolar ones. Thus, not including the heteronuclear scalar couplings in the search might be more appropriate, but here we do not care since most are within the error bars of the dipolar couplings. Many variations of our approach could have been presented. In fact, later in this chapter we discuss how our approach can be unified with standard pure frequency fitting.

## 3.2 The NAFONS algorithm

In NAFONS, transitions assignment is encoded in the objective function, such that at each evaluation of the objective function, the program automatically assigns a group of simulated transitions to the group of experimental ones, and then assigns the individual transitions within the two groups. Spectral assignment can thus vary at any step of the optimization of the parameters, but is assumed to be correct at the optimum, so that the assignment problem is effectively incorporated within the optimization problem.

In practice, we first extract the experimental frequencies of the $N$ peaks with biggest integrals (where $N$ is a suitable and sufficiently large number), and store them in increasing order in a vector $\vec{F}^{exp}$. For example, consider the spectrum illustrated below. Then, for $N = 4$ and $N = 5$, we have $\vec{F}^{exp} = (-1, 0, 1, 3)$ and $\vec{F}^{exp} = (-2, -1, 0, 1, 3)$ respectively.

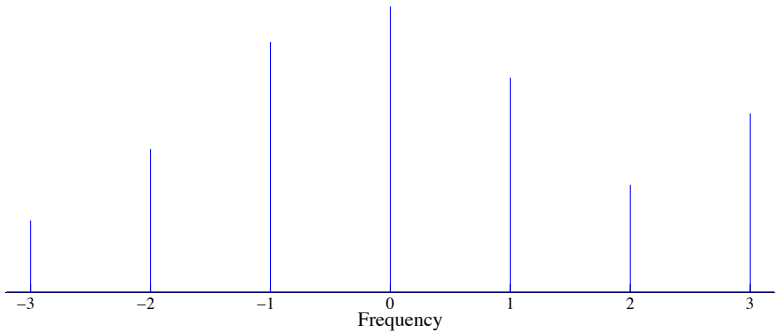


Similarly, we define $\vec{F}^{sim}$ as the vector containing the frequencies, in increasing order, of the $N$ simulated transitions with largest integrals. An important point to make here is that $\vec{F}^{sim}$ depends on the Hamiltonian underlying the simulated spectrum.Obviously, this implies that $\vec{F}^{sim}$ varies during an optimization over the parameters of the Hamiltonian. It is important to point out is that the frequency of the coherences is not the only source of changes in the vector $\vec{F}^{sim}$. In fact, the group of selected coherences can change, and their positions in $\vec{F}^{sim}$ can change as well. For example, consider again the blue spectrum above. Let's say that the parameters used in simulation are a little off from their actual values, and that the simulated spectrum looks like the red spectrum below.

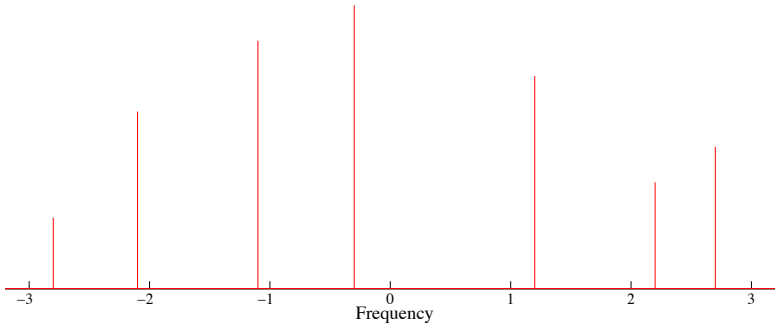


We see that the position of the coherences has changed a little, but the important difference here is that if $N = 4$, then $\vec{F}^{sim} = (-2.1, -1.1, -0.3, 1.2)$. In other words,

the four coherences selected in the red spectrum are not even the same as the four coherences selected in the blue spectrum. This illustrates how much the vector $\vec{F}^{sim}$ can be so fundamentally different from the vector $\vec{F}^{exp}$. The key point here is that we must have $\vec{F}^{sim} = \vec{F}^{exp}$ when the parameters of the simulation are correct. Thus, if the optimization procedure is carried by minimizing the difference between $\vec{F}^{sim}$ and $\vec{F}^{exp}$, then the spectral assignment problem has effectively been incorporated into a standard optimization problem that can be addressed by a computer rather than a human. At first, finding the global minimum might seem impossible to achieve. In the following, we present a global optimization strategy for solving this problem.

We now present a global optimization strategy for minimizing the difference between $\vec{F}^{sim}$ and $\vec{F}^{exp}$. The optimization procedure is done as follows, starting from an arbitrary Hamiltonian parameters vector $\vec{x}_0$, which is a list of the couplings and offset frequencies.

1 Find a minimizer $\vec{x}^*$ of $f(\vec{x}) = \sum_j \left(F_j^{exp} - F_j^{sim}(\vec{x})\right)^2$

2 Update the initial guess: $\vec{x}_0 = \vec{x}^*$

3 Generate a random vector $\vec{w}$, with each entry chosen uniformly at random in {0,1}

4 Find a minimizer $\vec{x}^*$ of $f_{\vec{w}}(\vec{x}) = \sum_j w_j (F_j^{exp} - F_j^{sim}(\vec{x}))^2$

5 Update the initial guess: $\vec{x}_0 = \vec{x}^*$

6 Repeat all these steps until the global minimum is reached

**Algorithm 1:** Basic global optimization strategy used in our NAFONS method.

In the NAFONS approach, assignment of the transitions is thus encoded in the objective function using simple rules: for each point of the parameters space, the group of simulated transitions is selected using their integrals, and the assignment is done by sorting the frequencies in increasing order. This is a natural way of optimizing both the parameters and the assignment of the transitions.

We now elaborate on our formulation of the optimization problem to solve, so as to understand the origin of its claimed robustness. The problem to solve is represented as

$$\min_{\vec{x}\in\Omega} \quad f_{\vec{w}}(\vec{x}) = \sum_j w_j (F_j^{exp} - F_j^{sim}(\vec{x}))^2, \tag{3.1}$$

where $\vec{x}$ is the vector of parameters, $\Omega$ is the search domain, $\vec{F}^{exp}$ is the vector of sorted experimental frequencies, $\vec{F}^{sim}$ is the vector of sorted simulated frequencies and $\vec{w}$ is a vector of random weights. The goal is to find a $\vec{x}^*$ that is a solution to problem (3.1) for any value of $\vec{w}$. In principle, this is possible only for the optimal solution, in which case

all of the experimental and simulated peaks should be in (quasi) exact agreement. In this case, we should have $\vec{F}^{exp} = \vec{F}^{sim}$, or equivalently $(\vec{F}^{exp} - \vec{F}^{sim}) = \vec{0}$, and thus follows that for any $\vec{w} \in \mathbb{R}^N$ we have $\sum_j w_j (F_j^{exp} - F_j^{sim})^2 = 0$.

In a sense, this formulation of the problem is a way of avoiding suboptimal solutions by using the fact that the number of objective functions that we could globally minimize to get the Hamiltonian is infinite. In other words, it is not the typical approach in which one wants to minimize a particular function. Here, we consider a large number of objective functions which do not share the same suboptimal solutions, but that do share a same optimal solution, and that overlap mainly for low error suboptimal solutions. This approach is also supported by the fact that the problem is greatly overdetermined, due to the redundancy of single order quantum coherence spectra, so that we could choose that only a few elements of $\vec{w}$ are non-zero and still have a valid objective function $f_{\vec{w}}$.

We review here the global optimization strategy used in our method. To solve problem (3.1), we start from a guess $\vec{x}_0$ and then find a minimizer $\vec{x}^*$ of $f(\vec{x}) = \sum_j (F_j^{exp} - F_j^{sim}(\vec{x}))^2$. Then, the solution $\vec{x}^*$ is used as the initial guess for minimizing a randomly modified objective function of the form $f_{\vec{w}}(\vec{x}) = \sum_j w_j (F_j^{exp} - F_j^{sim}(\vec{x}))^2$, where the elements of $\vec{w}$ are chosen randomly to be either 0 or 1. If the solution $\vec{x}^*$ is a global minimizer of $f$, then the solver will not modify the solution, otherwise the solver continues the optimization with the modified objective function $f_{\vec{w}}$. These two steps can be done repeatedly in a loop. To generalize this scheme, one could chose to solve a randomly modified problem $M$ times at each iteration of the loop, so that a loop has the form

$$\begin{aligned} \text{Solve} \quad & \min_{\vec{x}\in\Omega} \; f(\vec{x}) = \sum_j (F_j^{exp} - F_j^{sim}(\vec{x}))^2, \\ \text{Solve} \times M \quad & \min_{\vec{x}\in\Omega} \; f_{\vec{w}}(\vec{x}) = \sum_j w_j (F_j^{exp} - F_j^{sim}(\vec{x}))^2, \end{aligned} \tag{3.2}$$

where the vector $\vec{w}$ is generated randomly for each different minimization. The equilibrium state of this process is the commonly shared optimal solution.

To solve each minimization problem, we used an interior-point approach [52], and also found that including pattern searches [53] could help to locate the optimum. Then, when the desired solution is found, a least squares fit [54] of the spectrum line shape is finally done, mainly to adjust the decoherence rates of each spin and the scalar couplings.

In the following section, we present experimental results for characterizing the Hamiltonian of a 6-spin system. We also introduce an experimental method for simplifying the analysis of NMR spectra for heteronuclear spin systems. For this experiment, we also successfully tested a random walk approach in which the loop (3.2) is replaced by a single step taken into the direction that minimizes $f$ followed by an other single step in the direction that minimizes a randomly chosen $f_{\vec{w}}$.

## 3.3 Results for 2,3-Difluorobenzaldehyde

In this section, we present the experimental results for our characterization of the Hamiltonian of the spin system of 2,3-Difluorobenzaldehyde ($C_7H_4F_2O$) molecules dissolved into the liquid crystal ZLI-1132. The molecular structure is schematically represented in Figure 3.1. Experimental data are taken in a Bruker 600 MHz spectrometer. The temperature is controlled at 284K. We measure the Hamiltonian parameters through fitting the following spectra: **1)** fluorine spectrum with proton decoupling, **2)** proton spectrum with fluorine decoupling, **3)** spectra obtained by selective transition pulses based on spectrum 2), **4)** fluorine spectrum without proton decoupling, and **5)** proton spectrum without fluorine decoupling. We use the standard composite decoupling pulses, *i.e.* GARP [55] to decouple fluorine spins, and SPINAL-64 [56] to decouple proton spins. The selective transition pulses are Gaussian shaped pulses with duration of 20 ms.

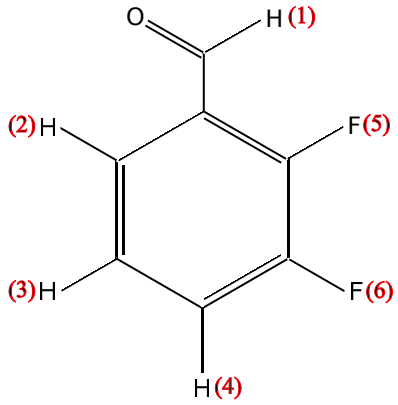


Figure 3.1: Molecular structure of 2,3-Difluorobenzaldehyde and the spin labelling.

For this experiment, the NAFONS approach is implemented in a highly simplified configuration. The optimization is done directly over the chemical shifts and dipolar couplings, *i.e.* without assuming or guessing the molecular geometry and order parameters. In addition, the optimization is done without a proper initial guess (0 Hz for each parameter) and without proper bounds ($\pm$2500 Hz for each parameter). Moreover, the diagonalizations of the Hamiltonian are done with a general QZ algorithm [57]. Finally, the program is implemented in MATLAB and runs on a laptop.

After having obtained the chemical shifts and dipolar couplings with our NAFONS method, we use a standard curve fitting algorithm to fine tune these parameters and also to estimate the scalar couplings. The estimation of the parameters is reported in Table 3.1. The errors are estimated by comparing the values obtained from the different fitted spectra and by using the standard deviation assuming a typical gaussian noise. In the following, we present the details of this experiment.

| | $H_1$ | $H_2$ | $H_3$ | $H_4$ | $F_5$ | $F_6$ |
|---|---|---|---|---|---|---|
| $H_1$ | -1770(3) | -424(3) | -144(3) | -154(2) | -1505(4) | -232(3) |
| $H_2$ | 0.13(0.06) | -149(2) | -2166(8) | -368(4) | -42(4) | -106(2) |
| $H_3$ | -0.03(0.06) | 2.7(0.1) | 172(2) | -931(5) | -62(4) | -46(3) |
| $H_4$ | 0.13(0.08) | 0.61(0.06) | 2.9(0.3) | -234(3) | -236(3) | -384(3) |
| $F_5$ | -0.02(0.06) | 2.8(0.2) | 0.7(0.3) | 4.1(0.2) | -885(3) | -1589(7) |
| $F_6$ | -0.32(0.08) | 0.76(0.03) | 2.5(0.4) | 4.8(0.8) | 7(1) | 948(2) |

Table 3.1: Parameters of the Hamiltonian for 2,3-Difluorobenzaldehyde measured in the liquid crystal solvent ZLI-1132. The scalar couplings, chemical shifts and dipolar couplings (in Hz) are respectively given below, on, and above the main diagonal of the table. The chemical shifts are given with respect to transmitter frequencies, around 600.13 MHz and 564.62 MHz, for proton and fluorine spins respectively.

### 3.3.1 Fluorine spectrum with proton decoupling

The first spectrum to be analyzed is the one of the two fluorines decoupled from the protons. There are two chemical shifts and one dipolar coupling to estimate. The four main transitions are selected for the optimization, and convergence is easily reached within a second. In fact, this problem is very simple and can even be solved analytically (see Appendix A). The agreement between the simulation and the experiment shown as Figure 3.2 indicates a reliable estimation of the parameters. It can be seen that there is a "junk" peak in the experimental spectrum, possibly due to the imperfection of decoupling. The results for the chemical shifts (in Hz) of $F_5$ and $F_6$ are: $-894(2)$ and $937(2)$ with respect to a transmitter frequency. The result for the dipolar coupling (in Hz) is: $-1595(7)$.

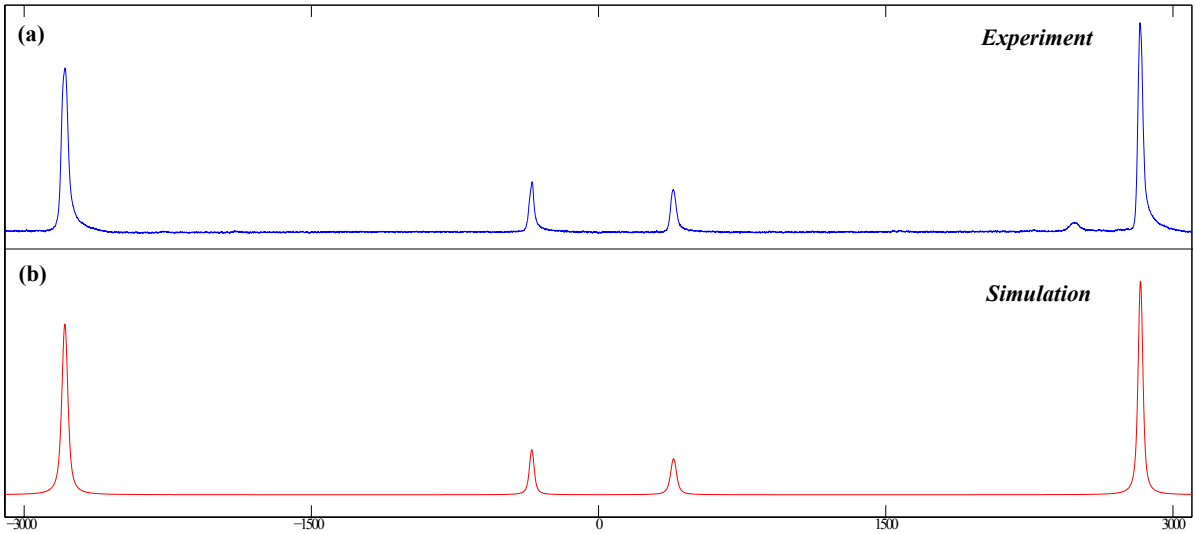


Figure 3.2: Fluorine spectrum with proton decoupling, obtained in **(a)** experiment, and by **(b)** simulation. The agreement indicates a reliable estimation of the parameters.

### 3.3.2 Proton spectrum with fluorine decoupling

The next spectrum to be analyzed is the one of the protons decoupled from the fluorines. The 26 transitions with biggest integrals are selected for an optimization. For several trials, convergence is usually reached within 10 minutes. The mean error for the coherences frequency is 0.25 Hz, and is probably due to line-overlap, which is not taken into consideration in pure frequency fitting. The chemical shifts (in Hz) for $H_1$, $H_2$, $H_3$ and $H_4$ are respectively: $-1783(2)$, $-158(1)$, $165(1)$ and $-242(1)$. The agreement between the simulation and the experiment shown as Figure 3.3 indicates a reliable estimation of the couplings in Table 3.1. Some small differences in the relative heights of the transitions are present, and might be explained as the imperfection in our way of modelling decoherence.

The estimation of the parameters is again supported by the molecular structure shown in Figure 3.1. The coupling is stronger for neighbor nuclear spins. The shape of the experimental spectrum supports these values as well. Around -2000 Hz, the cluster of transitions with strong decoherence corresponds to $H_1$. These transitions are closely distributed around the chemical shift value, due to the fact that the couplings involving $H_1$ are small ($< 450$ Hz). The two sets of 4 transitions with high amplitudes on the extreme left and extreme right of the spectrum both correspond to a mix of $H_2$ and $H_3$ transitions. They are at the extremities of the spectrum due to the large coupling (-2166 Hz) between $H_2$ and $H_3$. The transitions corresponding to $H_4$ are distributed on a width of $\sim$1600 Hz around the centre of the spectrum. This is mainly due to the coupling between $H_3$ and $H_4$ (-931 Hz). The chemical shifts (up to a scaling factor) are further verified by a 2D experiment using Lee Goldburg decoupling technique [58, 59].

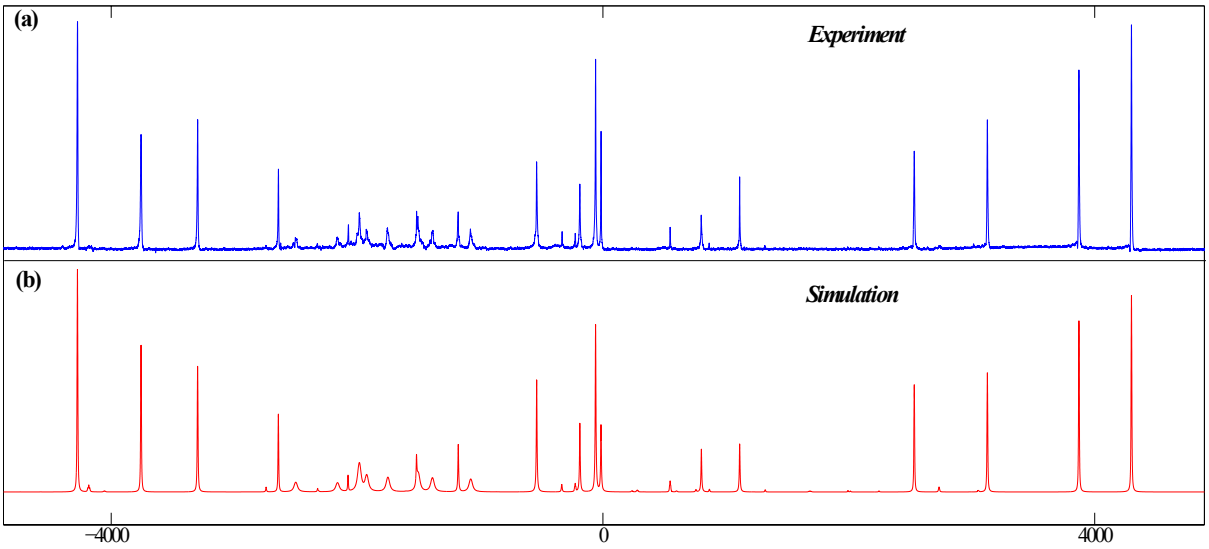


Figure 3.3: Proton spectrum with fluorine decoupling, obtained in **(a)** experiment and by **(b)** simulation. The agreement indicates a reliable estimation of the parameters.

### 3.3.3 Measuring dipolar couplings between heteronuclear spins

We now introduce a new experimental method for simplifying the analysis to measure dipolar couplings between heteronuclear spins. As we will see, this is a very powerful method when it applies. Having previously obtained the protons chemical shifts and protons homonuclear couplings, shown in Table 3.1, the proton Hamiltonian can be diagonalized, and each eigenvector can be expressed in the computational basis, *i.e.* $\{|0\rangle, |1\rangle\}$, so as to build the map between transitions and energy levels. We can exploit transition selective pulses to individually excite certain transitions in the spectrum shown in Figure 3.3(a). The goal is to make easier the numerical analysis for estimating the dipolar couplings between protons and fluorines. There are about ten well resolved peaks in Figure 3.3(a) that can be well addressed by Gaussian shaped pulses with 20 ms. Five experimental spectra obtained through transition selective pulses are shown as the spectra in Figures 3.4(b)-(f). Figure 3.4(a) is the same spectrum as in Figure 3.3(a), and is at the top of Figure 3.4 for identifying the peaks in Figures 3.4(b)-(f). Figure 3.4(g) shows the full proton spectrum without fluorine decoupling.

We select the five transitions mentioned above, each of which corresponds to a density matrix that can be written as the external product of the eigenstates involved in the transition, represented as

$$\rho_{ij}^{H} = |E_i\rangle\langle E_j|, \tag{3.3}$$

where $|E_i\rangle$ and $|E_j\rangle$ denote eigenstates of the proton Hamiltonian. Then, we switch off the decoupling channel for fluorine spins, and take the spectrum with the couplings between heteronuclear spins. The spectra corresponding to spectra in Figures 3.4(b)-(f) are respectively shown in Figures 3.4(h)-(l). The corresponding states are represented as

$$\rho_{ij} = \rho_{ij}^{H} \otimes I_2, \tag{3.4}$$

where $I_2$ denotes a $4\times4$ identity matrix, representing the state of the two fluorine spins. We use the $\{\rho_{ij}\}$ as the input states to simultaneously analyze the spectra shown in Figures 3.4(h)-(l) and extract all the heteronuclear dipolar couplings. Here, by *simultaneously analyzing* the spectra, we mean that the objective functions for the different spectra are combined into a single one, which is minimized by the algorithm. Then again, we use our NAFONS approach to do this optimization. The chemical shifts are allowed to vary $\pm\,50\,\mathrm{Hz}$ from their values obtained with decoupling pulses. For several trials, convergence is usually reached within 10 minutes. We now have all the parameters of the Hamiltonian, and we are thus ready to see if the full proton and the full fluorines spectra match with their corresponding simulation. This is the final step of the analysis.

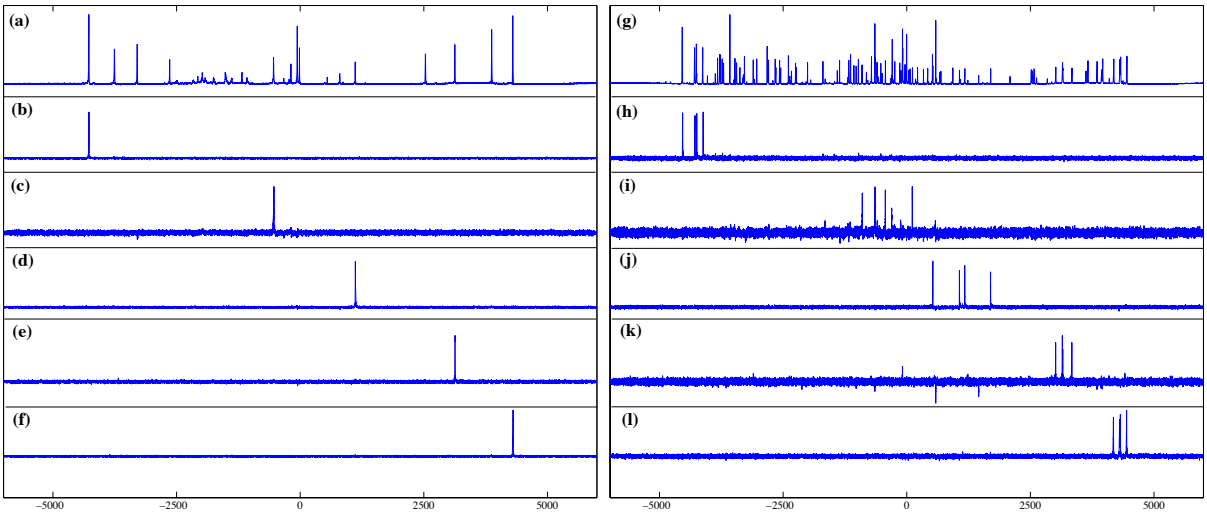


Figure 3.4: Spectra for extracting the dipolar couplings between heteronuclei. **(a)** Full proton spectrum with fluorine decoupling and **(b)-(f)** corresponding subspectra obtained by transition selective pulses. **(g)** Full proton spectrum without fluorine decoupling and **(h)-(l)** corresponding subspectra obtained by the same transition selective pulses.

### 3.3.4 Complete fluorine and proton spectra

We now analyze the complete fluorine and proton spectra. Having all the parameters of the natural Hamiltonian, we use these parameters to fit the complete fluorine and proton spectra using least squares on the spectral line shape. This is done mainly to adjust the decoherence rates of the spins and the scalar couplings. In fact, during this line shape fit, the Hamiltonian parameters all change less than 1% from the values previously obtained. These changes are most probably due to line-overlap, which is not taken into consideration during the pure frequency fit. In other words, this least squares fit of the spectral line shape is mainly to fine tune the parameters and visualize the agreement between the simulation and the experiment. In fact, as it will be discussed in the next section, least squares fitting of the spectral line shape is rarely helpful for dipolar coupled spin systems, unless very good initial guesses are available.

The results for the fluorine and proton spectra are shown respectively in Figure 3.5 and Figure 3.6. Then again, the parameters of the Hamiltonian are listed in Table 3.1. The $T_2^*$ (in ms) for $H_1$, $H_2$, $H_3$, $H_4$, $F_5$ and $F_6$ are respectively: 80.2(0.3), 65.8(0.2), 60.4(0.3) 62.4(0.2), 11.6(0.3) and 15.9(0.1). The agreement between the simulation and the experiment is again very good, showing that we do in fact have an accurate estimate of the Hamiltonian of 2,3-Difluorobenzaldehyde in the liquid crystal ZLI-1132.

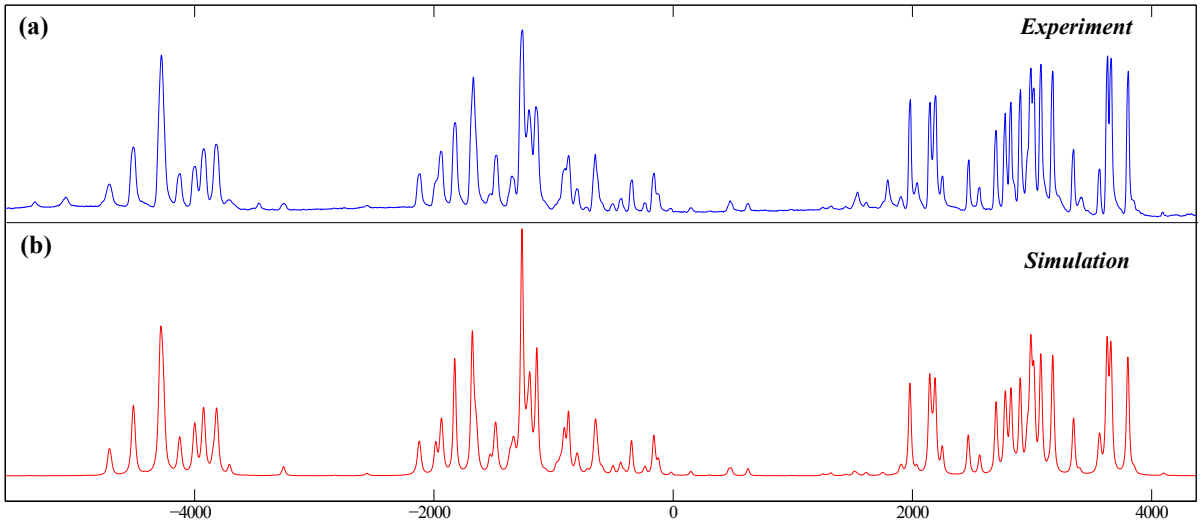


Figure 3.5: Fluorine spectrum without proton decoupling, obtained in **(a)** experiment and by **(b)** simulation. The occasional difference in heights is probably due to our modelling of decoherence (see text). The agreement indicates a reliable estimation of the parameters.

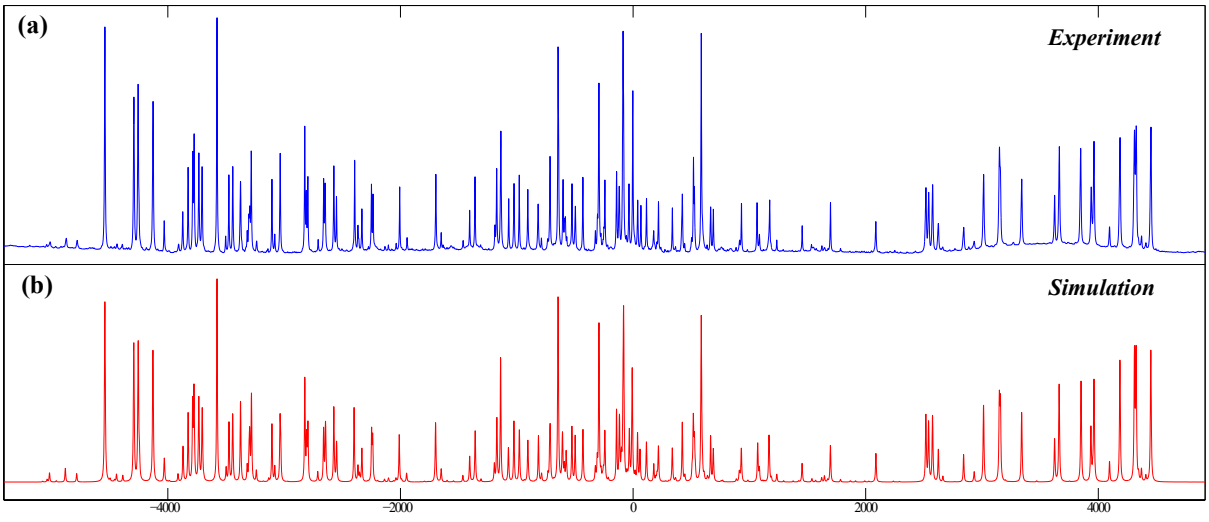


Figure 3.6: Proton spectrum without fluorine decoupling, obtained in **(a)** experiment and by **(b)** simulation. The occasional difference in heights is probably due to our modelling of decoherence (see text). The agreement indicates a reliable estimation of the parameters.

This concludes of presentation of the experimental results obtained for the characterization the Hamiltonian of 2,3-Difluorobenzaldehyde in the liquid crystal ZLI-1132. Solving such a spin system is considered to be a hard problem, and it thus shows the potential of the methods presented in this chapter. In the next section, we explicitly compare our methods to other methods in the literature.

## 3.4 Discussion

In this section, we compare our NAFONS approach to other spectral analysis approaches in the literature. There are three main types of methods in the literature: pure frequency fitting, total line shape fitting and integral transform fitting. We discuss the weaknesses of each of these methods. Doing this will make it clear that our approach successfully addresses fundamental problems in spectral analysis of dipolar coupled spin systems. We also discuss how exactly our experimental method to simply the analysis of heteronuclear spin systems helps the numerical search for the correct parameters of the Hamiltonian.

In the approach introduced by Castellano and Bothner-By [16], the differences between the observable peak frequencies and the simulated transition frequencies are minimized using a least squares algorithm. The well-known major drawback of this method is the requirement of spectral assignment, to establish which experimental peak correspond to which simulated transition. In traditional programs such as LAOCOONOR [20], PANIC [21] and LEQUOR [22], both the parameters and the spectral assignment have to be adjusted by the operator before each trial fitting. An estimated Hamiltonian is therefore required such that a sufficient number of transitions can initially be assigned for subsequent iterations that aim to refine the parameters and enlarge the set of assigned transitions, using the intelligence, intuition and patterns recognition ability of an experimented human user. The assignment step requires a great deal of time and effort by the user, and cannot be easily automated because only the operator can discriminated between the different assignments. Successful attempts of automating the assignment procedure have been reported in programs such as PAREMUS [23] and MIMER [24], but these are limited to simple solutes in isotropic solvents. Thus, in traditional pure frequency fitting algorithms, the procedure of spectral assignment is still the most decisive and difficult step, rapidly rendering them impossible to apply, especially when the molecular geometry and orientational parameters are unknown or difficult to guess.

Automatic methods which do not require spectral assignment have been developed as an alternative. These approaches, called integral transform (IT) and total line shape (TLS), use the full spectral line shape. In the IT approach, introduced by Diehl, Sýkora and Vogt [25], the spectrum is transformed into a small set of coefficients by means of linear integral transforms using orthogonal bases. The differences between the coefficients obtained from the experimental spectrum and those obtained from the simulated one are minimized with a standard optimization routine. In the TLS approach, the total line shape of the NMR spectrum is fitted. The idea was first demonstrated by Glidewell, Rankin and Sheldrick [28], and also studied by Heinzer [29]. A matrix method derived from a general formulation of the least squares problem was then developed by Stephenson and Binsch [30, 31]. The originality in their method was the use of cross-correlation

functions to smooth the landscape, other techniques such as spectrum broadening [34] and integral curves [35] have also been proposed for this purpose. This method, and its subsequent modifications - DAISY [32] and WIN-DAISY [33], were later improved by the use of Genetic Algorithms (GA's) [35–39], which are able to search through many basin of attractions. It is known that for GA's, if the search ranges become too large, there is insufficient coverage of the parameter space to locate the global minimum [38]. Some improvements can be obtained by the use of Evolutionary Strategies (ES's), which usually converge faster than GA's [38]. Evolutionary algorithms such as GA's and ES's are thus suitable only for molecules with high symmetry and with accurately known geometrical structure [38]. In general, both the IT and TLS approaches suffer from severe limitations: they are computationally very much slower than frequency fitting [23, 26, 27]; their global optimization strategy is either absent or operational only in small search spaces; the operator has hardly any means of interacting with the program to increase its efficiency. Due to these limitations, automatic analysis is not routinely employed [48], and the Castellano-Bothner-By approach is still by far the most widely used [20], despite the requirement of spectral assignment.

The originality of our approach can now be seen: it is a pure frequency fit program which incorporates the spectral assignment problem into a standard numerical optimization problem that can be addressed by a computer. In contrast with traditional automatic methods, evaluation of the objective function does not require the expensive computation of the spectral line shape. Moreover, our global optimization strategy, based on the injection of randomness, is able to cover a large search space without getting trapped in local minima. The most interesting feature of our approach is perhaps its compatibility with operator interventions. In fact, at any moment, the operator could pause the program, so as to visually compare the spectra and possibly choose to impose constraints on the spectral assignment, gradually removing the suboptimal attractors from the landscape. The intelligence of the operator can thus be effectively injected into the search. For these reasons, we think that this new approach successfully addresses the fundamental problems usually encountered in spectral analysis.

It is also relevant to emphasis the relationship between the experimental method presented in section 3.3.3 and the computational method. The experimental method allows to select specific transitions so as to minimize the complexity of the analysis to be done. Not only the number of transitions is much less, but the number of possible assignments for these remaining transitions is also reduced. For this experiment, only 21 transitions are used to extract the heteronuclear dipolar couplings, but only $4!\cdot5!\cdot4!\cdot4!\cdot4!$ assignments are possible instead of $21!$. The experiment also makes it possible to identify which transitions should be used for the analysis, otherwise the presence of overlap becomes an obstacle to this step.

## 3.5 Conclusion

We proposed a new method for solving NMR spectra of solutes dissolved in liquid crystals, and applied it to solve a 6-spin system with very low symmetry in structure and without the use of *a priori* knowledge or assumptions on the interspin distances or order parameters, which is in contrast with the results in previous experiments [14,17–20,30,31,33,35–39,48]. Our method includes a new spectral analysis program - NAFONS, and experimental techniques to simplify spectral analysis for extracting the dipolar couplings between heteronuclear spins. In contrast with traditional pure frequency fitting methods [16–24], NAFONS does not require spectral assignment, and is thus fully automatic. In contrast with line shape fitting methods [28–39], evaluation of our objective function does not involve the expensive computation of the spectral line shape, and the global optimization strategy can cope with a large search space. We believe that our results should be helpful to implement spectral analysis of dipolar coupled systems, and can be extended to larger systems. Using these methods, it should now be much easier to create a library of molecules for chemical structure analysis and other filed depending on the full Hamiltonian such as quantum computing. In the next chapter, we present how the 6-spin system introduced in this chapter can be controlled using pulse sequences design algorithms.

# Chapter 4

# Quantum Optimal Control

In the previous chapter we have successfully measured the Hamiltonian of an oriented 6-spin system. How can we control this system in practice? For simple solutes dissolved in liquid state environments, control sequences to implement specific unitaries can often be written down by hand and optimized heuristically. The situation is quite different for dipolar coupled spin systems, for which the spectra are usually very complicated and single spin addressability is lost. As a consequence, even pulse sequences for single spin rotations can rarely be designed analytically. In recent years, sophisticated pulse sequence design algorithms have been developed as a result, marking the emergence of a new field known as *quantum optimal control*. The idea behind this approach has already been introduced in chapter 2, were we presented the control Hamiltonian in section 2.3.3, and the evolution under this Hamiltonian in section 2.4.2. In particular, we also mentioned that the amplitudes of the control Hamiltonian could be discretized into timesteps, and that the control sequences for a particular desired unitary evolution could be found using numerical optimization algorithms. In this chapter, we present such an algorithm, known as GRAPE (GRadient Ascent Pulse Engineering). We also explain how to design experimentally robust pulses, and how the numerical search can be fasten using a subsystem approach. Moreover, we discuss the errors that occur in experimental implementations, and how pulse smoothing and pulse fixing can help to reduce these errors. Then, we present GRAPE pulses for single spin rotations, obtained for 2,3-Difluorobenzaldehyde. We start by considering the full 6-spin system, in which case pulse design is very challenging. Then, we present results for the proton subsystem decoupled from the fluorines.

## 4.1 The GRAPE algorithm

Here, we present the GRadient Ascent Pulse Engineering (GRAPE) algorithm [9]. The purpose of this well-known numerical optimization algorithm is to design pulse sequences that implement desired unitaries for specific systems. As we will see, this approach requires the full knowledge of the natural Hamiltonian, showing the importance of the previous chapter. We also discuss how to design experimentally robust pulses and how the search can be fasten using a subsystem approach. Finally, we discuss experimental errors that occur when GRAPE pulses are implemented in practice, and we show how these errors can be reduced by smoothing the pulses and also by using a method known as pulse fixing.

As described in section 2.4.2, the evolution of a spin system is driven by both its natural Hamiltonian $\mathscr{H}^{nat}$ and the control Hamiltonian $\mathscr{H}^{C}(t)$. In practice, the control Hamiltonian consists of a sum of control knobs $\{\mathscr{H}_j\}$ with control amplitudes $\{u_j(t)\}$,

$$\mathscr{H}^{C}(t) = \sum_j u_j(t)\mathscr{H}_j. \tag{4.1}$$

The particular form of the control Hamiltonian for NMR implementations was given is section 2.3.3. In practice, each $u_j(t)$ is piecewise constant in time. To be more precise, the time evolution is divided into $N$ timesteps of length $\Delta t$. For the sake of notation, in the following we will write $u_j(k)$ to denote the value of $u_j$ during timestep $k$.

Assuming that we have universal control over the system, it follows that for any desired unitary there exist a control sequence to implement it. How can we find such a control sequence? This is the problem addressed by optimal control theory. The first step is to define a metric for optimality. Given the control amplitudes $\{u_j(t)\}$ and a good model for the system and apparatus, we can simulate the unitary on a classical computer to obtain $U_{sim}$. The simulated gate can then be compared to the desired gate $U_{goal}$. Given that globals phases do not matter, it follows that a good choice for the fidelity function is

$$\Phi = \frac{\left|\mathrm{tr}\left(U_{goal}^{\dagger}U_{sim}\right)\right|^2}{D^2}, \tag{4.2}$$

where $D$ is the dimension of the Hilbert space. Given this fidelity function, one can then start thinking about using numerical optimization to search for the best pulse. Of course, the result is only as good as the search method is at finding global maxima. Moreover, finding a "good" pulse sequence does not imply that a better one does not exist. These are common problems in global optimization. However, the real problem for pulse finding in particular is the cost of the fitness function: evaluating it requires simulating the quantum evolution. This is where the clever part of the method is: to update control $u_j(k)$, we

take the derivative of $\Phi$ with respect to $u_j(k)$ using *back-propagation*. The idea behind back-propagation is to simulate the unitary both backwards starting from the goal unitary and forwards starting from the identity. The unitaries at each point are stored in memory. Using these stored unitaries, instantaneous derivatives of $\Phi$ can be obtained with only a few matrix multiplications, rather than by simulating the entire dynamics.

We now give the details of the GRAPE method. The unitary for timestep $k$ is

$$U_k = \exp\left[-i\Delta t\left(\mathscr{H}^{nat} + \sum_j u_j(k)\mathscr{H}_j\right)\right]. \tag{4.3}$$

To first order, we have

$$\frac{\delta U_k}{\delta u_j(k)} \approx -i\Delta t \mathscr{H}_j U_k, \tag{4.4}$$

where we require $\left|\Delta t\left(\mathscr{H}^{nat} + \sum_j u_j(k)\mathscr{H}_j\right)\right| \ll 1$ for this approximation to be accurate. The total unitary for all $N$ timesteps can then be calculated as

$$U_{sim} = U_{N-1}U_{N-2}\ldots U_1 U_0. \tag{4.5}$$

To first order in $\Delta t$, the gradient of $\Phi$ can then be calculated as

$$\frac{\delta\Phi}{\delta u_j(k)} = \frac{1}{D^2}\left[\mathrm{tr}\left(\left(U_{k+1}^{\dagger}\ldots U_{N-1}^{\dagger}U_{goal}\right)^{\dagger}\frac{\delta U_k}{\delta u_j(k)}U_{k-1}\ldots U_0\right) + c.c.\right]. \tag{4.6}$$

On the left side of the derivative is the partial propagator backwards in time, and on the right side is the one forwards in time. By storing these into memory, the gradient information can be calculated much faster, leading to a much more efficient search of the direction in which the control parameters should be modified. We can then use a simple steepest-ascent algorithm. A basic example of a GRAPE algorithm is given below.

1 Guess the initial controls $\{u_j(k)\}$

2 **while** $\Phi < \Phi_{thr}$ **do**

  Calculate $\{\delta\Phi/\delta u_j(k)\}$ using Eq.(4.6) and Eq.(4.4)

  Update all the controls as $u_j(k) \to u_j(k) + \epsilon\frac{\delta\Phi}{\delta u_j(k)}$, where $\epsilon$ is a small step size

**end**

**Algorithm 2:** Basic GRAPE algorithm. Here, $\Phi_{thr}$ is the fidelity threshold.

The pulse finder program used in this work was developed by C. A. Ryan and closely follows the GRAPE approach, but with some modifications [11, 60]. In the following, we present an approach to search for experimentally robust pulses, and we also discuss how breaking the spin system into subsystems can help to fasten the numerical search.

### 4.1.1 Robust pulses & the subsystem approach

There exists an approach to search for experimentally robust pulses. This is required due to the presence of several sources of errors that reduce the fidelity of the pulses in experiments. The most relevant error sources are inhomogeneities across the sample in the static field and the r.f. field. Moreover, the parameters of the natural Hamiltonian could be difficult to measure with high accuracy, or they might also have changed slightly since their measurement. To handle these experimental errors, we can define a new fidelity function which is the average fidelity of the pulse simulated over a range of parameters [11, 60].

Pulse finding can be very difficult, but there exists a subsystem approach to fasten the search [11, 60]. The idea is to decompose the system into subsystems, such that for each subsystem $A$ the desired unitary can be factored as $U_{goal} = U^A \otimes U^{A^C}$, where $A^C$ is the complement of subsystem $A$, and $U^S$ denotes a unitary acting only on system $S$. We can then define the fitness function as a weighted sum of the fitness function for each subsystem, and simulate the subsystems individually to reduce the computational time. Obviously, the subsystems must be defined such that the dominant dynamics is captured.

### 4.1.2 Smooth pulses & pulse fixing

The GRAPE algorithm presented above assumes that the control amplitudes can be varied arbitrarily and that unlimited power is available. This is of course not true experimentally. For example, the finite slew rate of the amplifier will lead to a switching transient, and we must also ensure that the power starts and ends at zero. There exists a solution to this problem that also has the advantage of speeding up the search [11, 60]. In practice, one finds that having many timesteps is rarely needed to find high fidelity pulses. This implies that we can start by finding a high fidelity pulse using relatively long timesteps (but such that the approximate gradient is still accurate). Then, we can digitally smooth the pulse with shorter timesteps, and use this smooth version of the pulse as the starting point for a new numerical optimization. This process can be repeated many times if required.

Do the r.f. control fields at the sample match what they are supposed to be? In practice, the actual pulse sequence can differ largely from the intended one. This is due in part to bandwidth constraints of the probe-resonant circuit, and to non-linearities in the pulse generation and amplification. This problem can be solved by *pulse fixing*, *i.e.* measuring the field at the sample and using a feedback loop to iteratively adjust the controls so that the field at the sample matches the simulation. The details can be found in [11, 60].

In the next section, we present GRAPE pulses for 2,3-Difluorobenzaldehyde, which is the molecule that we characterized in the previous chapter. Specifically, we are interested in single qubit rotations. These will be used in chapter 5 to certify quantum gates.

## 4.2 Results for 2,3-Difluorobenzaldehyde

In this section we present the GRAPE pulses obtained for 2,3-Difluorobenzaldehyde. We start with the results for the full 6-spin system, in which case pulse design is quite a challenge. In fact, we were unable to find pulses with fidelity above 95%. In addition, these pulses are neither robust nor smooth. Then, we present results for controlling the proton subsystem while applying a decoupling pulse. The results are much better, as we were able to find robust smooth pulses with 98% fidelity for all single-spin $\pi/2$ rotations. In practice, the pulses are found using large clusters, so as to run as many trials as possible.

### 4.2.1 Pulses for the full system

For the full 6-spin system, pulse design is in fact very tedious. Our goal was to obtain all six single-spin $\pi/2$ rotations about the $x$-axis. We could then obtain the single-spin $\pi/2$ rotations about the $y$-axis simply by changing the phase of the pulse.

Although we were able to find all pulses, these are neither robust nor smooth, with fidelity that never surpasses 95%. The pulses found have timestep's lengtht $\Delta t = 1\mu s$ and total length $4ms$. When using the subsystem approach, the subsystems are $\{H_1, F_5, F_6\}$ and $\{H_2, H_3, H_4\}$. One can see from Table 3.1 that this definition of the subsystems captures the dominant dynamics. In general, the pulses were found as follows:

**1)** Find a 99% fidelity pulse with $\Delta t = 4\mu s$, using the subsystem approximation.

**2)** Use this pulse as the initial guess for finding a 95% fidelity pulse with $\Delta t = 4\mu s$.

**3)** Smooth the pulse with $\Delta t = 2\mu s$ and optimize its fidelity to reach 95%.

**4)** Smooth the pulse with $\Delta t = 1\mu s$ and optimize its fidelity to reach 95%.

We tested one of these pulses experimentally, mainly in order to further confirm our estimation of the Hamiltonian. The fluorine spectrum for the implementation (without pulse fixing) of a $\pi/2$ rotation about the $x$-axis on $F_5$ is shown in Figure 4.1, were we also show the spectrum obtained by simulating the same GRAPE pulse. By comparing the two spectra, we can see that the agreement is reasonable despite the fact that the pulse is not robust or smooth and that it is implemented without pulse fixing. Thus, we can reasonably conclude that we do in fact have an accurate estimate of the natural Hamiltonian. Still, the fact that we were unable to find robust smooth pulses discourages us from attempting to perform complicated experiments using the full 6-spin system. In fact, by applying a heteronuclear decoupling pulse, we can use 2,3-Difluorobenzaldehyde as a 2-qubit system or a 4-qubit system. In the following, we present results for finding GRAPE pulses acting on the protons, when these are decoupled from the fluorines.

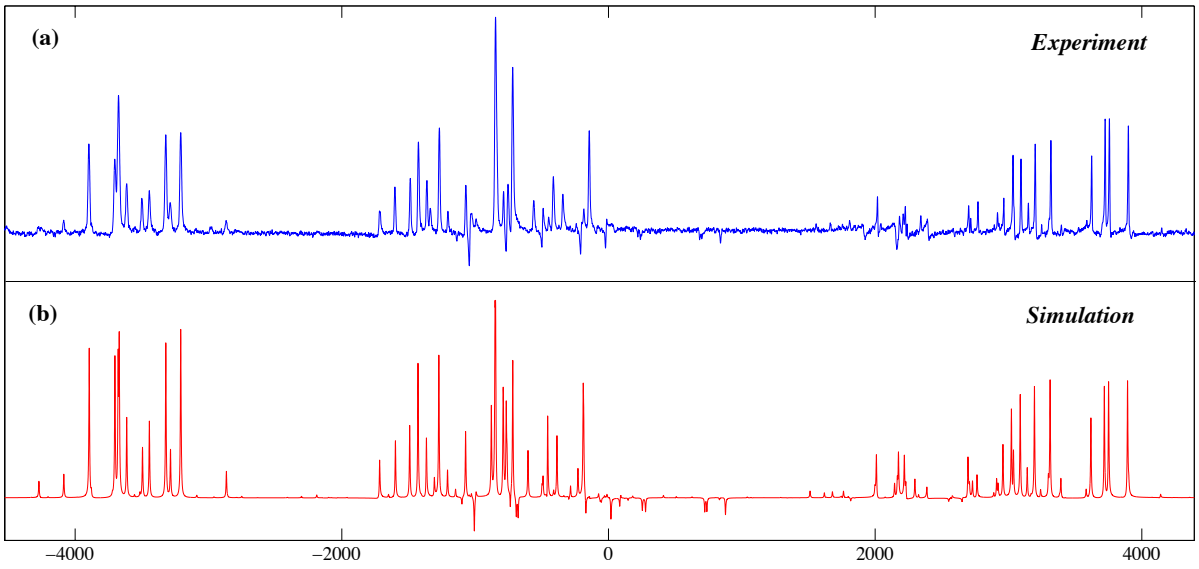


Figure 4.1: Fluorine spectrum after a $\pi/2$ rotation about the $x$-axis on $F_5$, obtained in **(a)** experiment and by **(b)** simulation of the GRAPE pulse. The pulse is neither robust nor smooth, and is implemented without pulse fixing. Its duration is 4 $ms$ and its fidelity is 95%. These results support our estimation of the natural Hamiltonian.

### 4.2.2 Pulses for the proton subsystem

As we have discussed above, controlling the full 6-qubit system of 2,3-Difluorobenzaldehyde seems to be a very challenging task. However, we can use heteronuclear decoupling to suppress the couplings between protons and fluorines, implying that 2,3-Difluorobenzaldehyde can also be used as a 2-qubit system or as a 4-qubit system. Here we consider the later case, *i.e.* the proton subsystem, and our goal is to obtain all four single-spin $\pi/2$ rotations about the $x$-axis. We can then obtain the single-spin $\pi/2$ rotations about the $y$-axis simply by changing the phase of the pulse. The method and the results for obtaining such GRAPE pulses are explained in the following.

Our objective here is to obtain 98% fidelity pulses with timestep's lengtht $\Delta t = 1\mu s$ and a total duration of $4ms$. The pulses should also be experimentally robust the chemical shifts variations of $\pm$10Hz and r.f. inhomogeneities of $\pm$3% across the sample. The steps to obtain these pulses are as follows:

**1)** Find a 99% fidelity pulse with $\Delta t = 4\mu s$, and then smooth it with $\Delta t = 2\mu s$.

**2)** Optimize the pulse's fidelity to reach 99%, and then smooth the pulse with $\Delta t = 1\mu s$.

**3)** Optimize the pulse's fidelity to reach 99%, and then smooth the pulse.

**4)** Use this pulse as the initial guess for finding a robust pulse with fidelity 98%.

We were able to obtain all four single-spin $\pi/2$ rotations about the $x$-axis. In contrast, directly trying to find a robust pulse was unsuccessful. The pulse shape for a $\pi/2$ rotation of $H_1$ about the $x$-axis is illustrated in Figure 4.2. Due to a lack of equipment, we did not test theses pulses in experiment. The reason is that one of the spectrometer available to us misses the equipment required to implement heteronuclear decoupling. Another spectrometer available to us is equipped to implement heteronuclear decoupling, but not to implement pulse fixing. However, the pulses found here will be used in simulations in chapter 5, were we will present methods for certifying the implementation of gates.

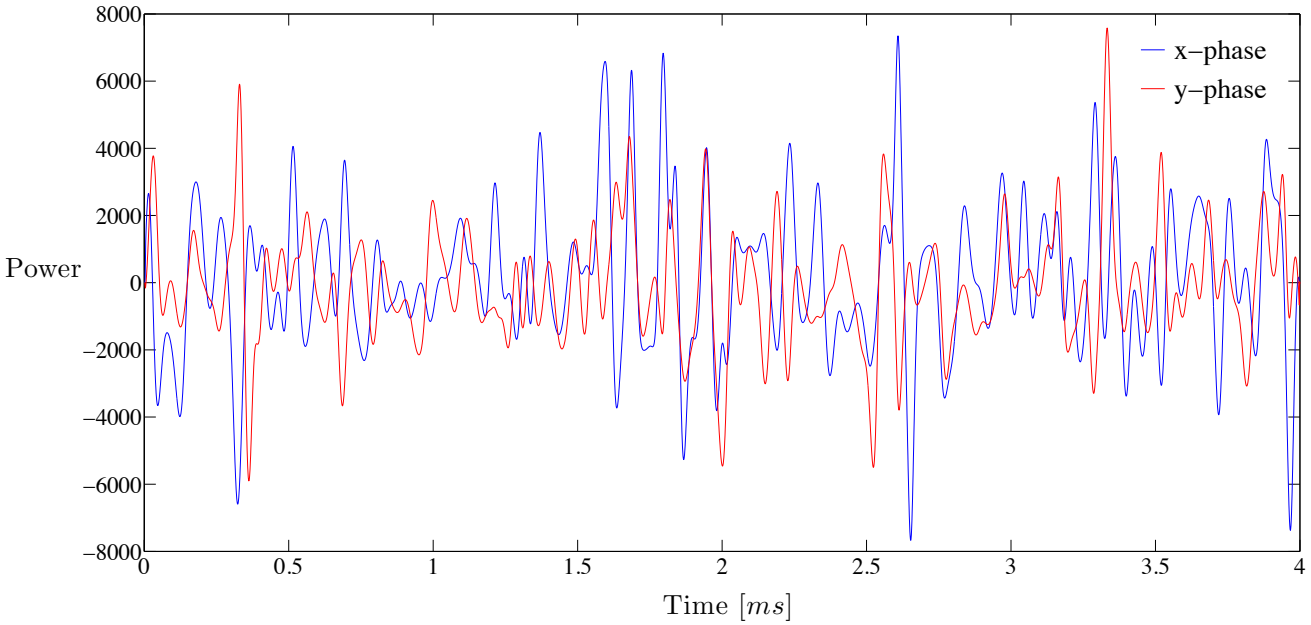


Figure 4.2: Pulse shape for a $\pi/2$ rotation of $H_1$ about the $x$-axis. The power is in units of the angular Rabi frequency. The blue curve is the power for the $x$-phase and the red curve is the power for the $y$-phase. The pulse's duration is $4ms$ and its fidelity is 98%.

In this chapter, we presented the GRAPE pulse sequence design algorithm, and we also explained how to design pulses that are robust to variations in the r.f. amplitudes and Hamiltonian parameters. In addition, we discussed how the numerical search can be fasten using a subsystem approach, and also how pulse smoothing and pulse fixing can help to reduce errors that occur in experimental implementations. Then, we used a GRAPE program in practice to find single-spin $\pi/2$ rotations for the oriented spin system of 2,3-Difluorobenzaldehyde. We first considered the full 6-spin system, in which case we found pulse design to be highly challenging. In fact, we were unable to find pulses with fidelity above 95%, and these are neither robust nor smooth. Then, we considered the proton subsystem decoupled from the fluorines, in which case we were able to find robust smooth pulses with 98% fidelity and $4ms$ length. In the next chapter, we present methods and results for certifying experimental implementations of quantum gates. The goal will be to measure how close the experimental gates are to the desired ideal ones.

# Chapter 5

# Certification of Quantum Gates

In chapter 3 we have proposed a new method for characterizing the Hamiltonian of dipolar coupled spin systems, and used it in experiment to characterize the oriented 6-spin system of 2,3-Difluorobenzaldehyde. Then, in chapter 4, we have presented how this system can be controlled using pulse sequence design algorithms. At this point, we thus have in hand a prototype quantum computing device. How faithful is this implementation to an ideal quantum computer? In other words, how close the implemented operations are to the desired ideal ones? This is the question addressed in this chapter. One approach to answer this question is to fully characterize the experiments via quantum process tomography [61], and calculate the average fidelity between the experimental and ideal operators to quantify how close these are. The main drawback of this approach is that the number of parameters required for complete characterization grows exponentially with the size of the system [62], making it impracticable for moderately large systems. As a result, significant efforts have been made to develop approaches that do not require complete characterization. In this chapter, we present such an approach known as *twirling*. We first start by discussing the concepts of average fidelity and averaged quantum channel. Then, we show how twirling can be used to measure the average fidelity of Clifford unitaries. Following this, we present a statistical analysis to obtain rigorous bounds for the accuracy of the results. We also present our own Monte Carlo approach in order to further investigate the accuracy of twirling experiments. Finally, we present results for 2,3-Difluorobenzaldehyde, obtained in experiments and also by simulations. A quick word about the notation: in the following, we will often denote quantum maps with a special font style, *e.g.* $\mathcal{U}$, $\mathcal{V}$.

## 5.1 Average fidelity & averaged channel

In this section, we discuss the concepts of average fidelity and averaged channel. We also introduce briefly a technique known as twirling, which will be explored in more details in the next section. We first start by explaining what are the types of quantum channels under consideration, and we then define the notions of average fidelity and averaged channel. Finally, we give a simple expression for calculating the average fidelity.

We start with some definitions. In this work, $\mathcal{P}_n$ denotes the *n-qubit Pauli group*

$$\mathcal{P}_n := \left\{ \bigotimes_{j=1}^{n} P_j \;\middle|\; P_j \in \{I,\ X,\ Y,\ Z\} \right\}, \tag{5.1}$$

where $I$, $X$, $Y$ and $Z$ are the usual single qubit Pauli matrices. Also, the *weight* of an operator $P \in \mathcal{P}_n$ is denoted $\mathrm{wt}(P)$ and is defined as the number of non identity terms in its tensor product form, *e.g.* $\mathrm{wt}(I \otimes X) = 1$. Finally, the *quantum channels* under consideration in this work will be completely positive maps of the form

$$\Lambda(\rho) = \sum_{P_i, P_j \in \mathcal{P}_n} [\chi]_{ij} P_i \rho P_j, \tag{5.2}$$

where $\rho$ is a density matrix, and $\chi$ is a matrix of dimension $4^n \times 4^n$ with $\mathrm{tr}(\chi) = 1$, $[\chi]_{ii} \geq 0$, and $[\chi]_{ij} = [\chi]_{ji}{}^*$. By convention, we will always have $P_0 := I^{\otimes n}$. Also, quantum channels with a diagonal $\chi$ matrix will be called *Pauli channels*.

We now introduce the concept of *average fidelity*. First, the *gate fidelity* between two superoperators $\mathcal{U}$ and $\tilde{\mathcal{U}}$ with respect to a state $|\psi\rangle$ is defined as

$$F_{|\psi\rangle}(\mathcal{U}, \tilde{\mathcal{U}}) = \langle\psi|\mathcal{U}^\dagger \circ \tilde{\mathcal{U}}(|\psi\rangle\langle\psi|)|\psi\rangle. \tag{5.3}$$

To get an expression independent of $|\psi\rangle$, we average over a unitarily invariant distribution of pure states to obtain the average fidelity between $\mathcal{U}$ and $\tilde{\mathcal{U}}$

$$\bar{F}(\mathcal{U}, \tilde{\mathcal{U}}) = \int d\mu(\psi) \langle\psi|\mathcal{U}^\dagger \circ \tilde{\mathcal{U}}(|\psi\rangle\langle\psi|)|\psi\rangle, \tag{5.4}$$

where $d\mu(\psi)$ is the unitarily invariant distribution of pure states known as the *Fubini-Study measure* [63]. We are interested in the noisy part of $\tilde{\mathcal{U}}$, so we define

$$\tilde{\mathcal{U}} = \Lambda \circ \mathcal{U}, \tag{5.5}$$

where $\Lambda$ is the channel representing the undesired part of the evolution. It follows that

$$\bar{F}(\mathcal{U}, \tilde{\mathcal{U}}) = \int d\mu(\psi) \langle\psi|\mathcal{U}^\dagger \circ \Lambda \circ \mathcal{U}(|\psi\rangle\langle\psi|)|\psi\rangle = \int d\mu(\psi) \langle\psi|\Lambda(|\psi\rangle\langle\psi|)|\psi\rangle, \tag{5.6}$$

where the last equality is due to the fact that $d\mu(\psi)$ is unitarily invariant. We see that the average fidelity depends only on the error channel $\Lambda$, *i.e.* $\bar{F}(\mathcal{U},\tilde{\mathcal{U}}) = \bar{F}(\Lambda)$. Also, a random state can be generated from a fixed state by applying a random unitary. Thus, we can equivalently average over a distribution of random unitaries invariant under conjugation

$$\bar{F}(\Lambda) = \int d\mu(V)\langle\psi|\mathcal{V}^\dagger \circ \Lambda \circ \mathcal{V}(|\psi\rangle\langle\psi|)|\psi\rangle, \tag{5.7}$$

where $d\mu(V)$ is a unitarily invariant distribution of random unitaries known as the *Haar measure* [63]. Defining the *averaged channel* as

$$\bar{\Lambda} = \int d\mu(V)\mathcal{V}^\dagger \circ \Lambda \circ \mathcal{V}, \tag{5.8}$$

one can see that the average fidelity of $\Lambda$ is in fact the gate fidelity of $\bar{\Lambda}$ with respect to the identity operation. The channel $\bar{\Lambda}$ is also known as the *Haar twirl* of $\Lambda$.

It is possible to obtain an analytical expression for the average gate fidelity. The starting point is to find a set of unitary gates $\{V_i\}$ and a probability distribution $\Pr(V_i)$ such that

$$\bar{F}(\Lambda) = \int d\mu(V)\langle\psi|\mathcal{V}^\dagger \circ \Lambda \circ \mathcal{V}(|\psi\rangle\langle\psi|)|\psi\rangle = \sum_i \Pr(V_i)\langle\psi|\mathcal{V}_i^\dagger \circ \Lambda \circ \mathcal{V}_i(|\psi\rangle\langle\psi|)|\psi\rangle. \tag{5.9}$$

Such mathematical objects are called *unitary 2-designs*, and one example of them is the $n$-qubit Clifford group $\mathcal{C}_n$ [64]. In other words, averaging over $\mathcal{C}_n$ and averaging over the Haar measure lead to the same average fidelity. When we average a channel $\Lambda$ over the Clifford group $\mathcal{C}_n$, it can be shown that the averaged channel, denoted $\bar{\Lambda}_{\mathcal{C}_n}$, acts as [65]

$$\bar{\Lambda}_{\mathcal{C}_n}(|\psi\rangle\langle\psi|) = p|\psi\rangle\langle\psi| + (1-p)\frac{I^{\otimes n}}{2^n}, \tag{5.10}$$

where $p = \frac{4^n[\chi]_{00}-1}{4^n-1}$. Calculating the gate fidelity of $\bar{\Lambda}_{\mathcal{C}_n}$ with respect to the identity operator, we find that the average fidelity of $\Lambda$ is given by [65]

$$\bar{F}(\Lambda) = \frac{2^n[\chi]_{00}+1}{2^n+1}. \tag{5.11}$$

Therefore, an estimate of the average fidelity can be obtained by measuring $[\chi]_{00}$.

In this section, we have presented the concepts of average fidelity and averaged channel. We also showed that by averaging over the $n$-qubit Clifford group, we can obtain a simple formula for calculating the average fidelity. According to this formula, in order to estimate the average fidelity of some quantum channel, we need to estimate $[\chi]_{00}$. How can we measure $[\chi]_{00}$ is practice? This is the topic of the next section, where we will show that this can be achieved via a technique known as twirling.

## 5.2 Twirling protocol

In this section, we present the twirling protocol introduced by O. Moussa [66], and we show how it allows us to estimate the average fidelity of Clifford gates. We first introduce a new group of unitary gates, denoted $\mathcal{C}_1\Pi$. Then, we average an error channel $\Lambda$ over this group, and we show that $[\chi]_{00}$ can be written as a linear combination of the eigenvalues of the averaged channel $\bar{\Lambda}_{\mathcal{C}_1\Pi}$. Finally, we show precisely how these eigenvalues can be measured experimentally for NMR systems in particular.

The group $\mathcal{C}_1\Pi$ is defined as the composition of $\Pi_n$ and $\mathcal{C}_1^{\otimes n}$, where $\Pi_n$ is the group of permutation of $n$ qubits and $\mathcal{C}_1^{\otimes n}$ is the $n$ fold tensor product of the 1-qubit Clifford group. The $\mathcal{C}_1\Pi$ twirl of a channel $\Lambda$ is denoted $\bar{\Lambda}_{\mathcal{C}_1\Pi}$, and is defined as

$$\bar{\Lambda}_{\mathcal{C}_1\Pi} = \frac{1}{|\mathcal{C}_1\Pi|} \sum_{\mathcal{V}_i \in \mathcal{C}_1\Pi} \mathcal{V}_i^\dagger \circ \Lambda \circ \mathcal{V}_i. \tag{5.12}$$

It can be seen that twirling over $\mathcal{C}_1\Pi$ transforms $\Lambda$ into a Pauli channel with error probabilities depending only on the weight of the error. In fact, it can be shown that [65]

$$\bar{\Lambda}_{\mathcal{C}_1\Pi}(\rho) = \sum_{\omega=0}^{n} \Pr(\omega) \mathcal{M}_\omega^p(\rho), \tag{5.13}$$

where $\Pr(\omega)$, the probability that a Pauli error of weight $\omega$ occurs, and $\mathcal{M}_\omega^p$ are given by

$$\Pr(\omega) = \sum_{\mathrm{wt}(P_i \in \mathcal{P}_n)=\omega} [\chi]_{ii}, \qquad \mathcal{M}_\omega^p(\rho) = \frac{1}{3^\omega \binom{n}{\omega}} \sum_{\mathrm{wt}(P_i \in \mathcal{P}_n)=\omega} P_i \rho P_i. \tag{5.14}$$

In particular, we have $\Pr(0) = [\chi]_{00}$. We see from Eq.(5.11) that we only need to measure the probability of no error $\Pr(0)$ in order to get an estimate of the average fidelity.

The problem of measuring the average fidelity has been translated into the problem of measuring the probability of no error. How do we measure $\Pr(0)$ in practice? First, we have to make the observation that the elements of $\mathcal{P}_n$ are eigenoperators of $\bar{\Lambda}_{\mathcal{C}_1\Pi}$. This can be understood from Eq.(5.14) and the fact that Pauli operators either commute or anti-commute with each other. In fact, it can be demonstrated that [65]

$$\bar{\Lambda}_{\mathcal{C}_1\Pi}(P) = \lambda_\omega P, \quad \text{where } P \in \mathcal{P}_n \text{ and } \omega = \mathrm{wt}(P). \tag{5.15}$$

The eigenvalues $\{\lambda_\omega\}$ are real numbers in the interval $[-1, 1]$ and depend only on the weight of their associated Pauli operator [65]. By default, we have $\lambda_0 = 1$. It can be

demonstrated that the relationship between the $\{\lambda_\omega\}$ and the $\{\Pr(\omega)\}$ is [65]

$$\lambda_\omega = \sum_{\omega'=0}^{n} [\Omega]_{\omega,\omega'} \Pr(\omega'), \qquad \Pr(\omega) = \sum_{\omega'=0}^{n} [\Omega^{-1}]_{\omega,\omega'} \lambda_{\omega'}, \tag{5.16}$$

where the matrices $\Omega$ and $\Omega^{-1}$ are given by [65]

$$[\Omega]_{\omega,\omega'} = \left[ \sum_{L=0}^{n} \frac{\binom{n-\omega}{\omega'-L}\binom{\omega}{L}}{\binom{n}{\omega'}} \frac{3^L + (-1)^L}{3^L} \right] - 1 \tag{5.17}$$

$$\left[\Omega^{-1}\right]_{\omega,\omega'} = \frac{3^{\omega+\omega'}\binom{n}{\omega}\binom{n}{\omega'}}{4^n} [\Omega]_{\omega,\omega'}. \tag{5.18}$$

In particular, for $\Pr(0)$, this implies that

$$\Pr(0) = \sum_{\omega=0}^{n} \frac{3^\omega \binom{n}{\omega}}{4^n} \lambda_\omega. \tag{5.19}$$

The problem of measuring the average fidelity has been translated into the problem of measuring the eigenvalues $\{\lambda_\omega\}$ of the twirled channel $\bar{\Lambda}_{\mathcal{C}_1\Pi}$. How can this be achieved? If we would have access to the twirled channel $\bar{\Lambda}_{\mathcal{C}_1\Pi}$, then we could measure the eigenvalues by doing $n$ different experiments, each using one of the following $n$ input state's deviations

$$\rho_\omega = Z^{\otimes\omega} I^{\otimes n-\omega}, \quad \omega \in \{1, \ldots, n\}. \tag{5.20}$$

In each experiment, we would send the input state through the averaged channel and then measure its expectation value, *i.e.* its projection onto itself, to get the corresponding eigenvalue. Obviously we do not actually have access the averaged channel, rather we only have access to the original channel $\Lambda$. Let's look at the expression of a specific $\lambda_\omega$, and let $\mathrm{wt}(P) = \omega$. Remembering that the definition of $\bar{\Lambda}_{\mathcal{C}_1\Pi}$ is given by Eq.(5.12), it follows that

$$\begin{aligned}
\lambda_\omega = \frac{1}{2^n}\mathrm{tr}\left(P\bar{\Lambda}_{\mathcal{C}_1\Pi}(P)\right) &= \frac{1}{2^n|\mathcal{C}_1\Pi|} \sum_{v_i \in \mathcal{C}_1\Pi} \mathrm{tr}\left(P v_i{}^\dagger \Lambda(v_i P v_i{}^\dagger) v_i\right) \\
&= \frac{1}{2^n|\mathcal{C}_1\Pi|} \sum_{v_i \in \mathcal{C}_1\Pi} \mathrm{tr}\left(\Lambda(v_i P v_i{}^\dagger) v_i P v_i{}^\dagger\right) \\
&= \frac{1}{2^n 3^\omega \binom{n}{\omega}} \sum_{\mathrm{wt}(P_i \in \mathcal{P}_n)=\omega} \mathrm{tr}\left(\Lambda(P_i)P_i\right).
\end{aligned} \tag{5.21}$$

where the last line follows from the fact that there are only $3^\omega\binom{n}{\omega}$ different values of $P_i = v_i P v_i{}^\dagger$ for $v_i \in \mathcal{C}_1\Pi$. We see that $\lambda_\omega$ is the average of a uniformly distributed random variable $T_\omega$ that can take any of the $3^\omega\binom{n}{\omega}$ values in the set

$$\mathcal{T}_\omega = \{t_i \mid t_i = \tfrac{1}{2^n}\mathrm{tr}\left(\Lambda(P_i)P_i\right),\ P_i \in \mathcal{P}_n,\ \mathrm{wt}(P_i) = \omega\}. \tag{5.22}$$

The problem of measuring $\lambda_\omega$ has been translated into the problem of measuring the elements of $\mathcal{T}_\omega$. We now present the experimental procedure to achieve this. Let's consider an $n$-qubit system, and assume that the available initial states are those in the set

$$\mathcal{D} = \{\pi_k Z^{\otimes\omega} I^{\otimes n-\omega} {\pi_k}^\dagger |\ \omega \in \{1,\dots,n\},\ \pi_k \in \Pi_n\}, \tag{5.23}$$

where $\Pi_n$ is the group of permutation of $n$ qubits. In other words, we can start the experiment with any state in the set $\mathcal{D}$. In addition, we will assume that only single-spin $\pi/2$ rotations are available. Now, let's say that we want to measure $t_i = \frac{1}{2^n}\mathrm{tr}\,(\Lambda(P_i)P_i)$, where $P_i \in \mathcal{P}_n$ and $\mathrm{wt}(P_i) = \omega$. We proceed as follows: we start with the operator $P \in \mathcal{D}$ that has weight $\omega$ and that has its identity terms at the same positions than the identity terms of $P_i$. For example, if $P_i = XIIY$, then we would start with $P = ZIIZ$. Next, we find the sequence of single-spin $\pi/2$ rotations, here we denote this sequence by $v_i$, such that $P_i = v_i P {v_i}^\dagger$. Finally, we measure the expectation value of $P_i$. The circuit summarizing this protocol is illustrated below in Figure 5.1

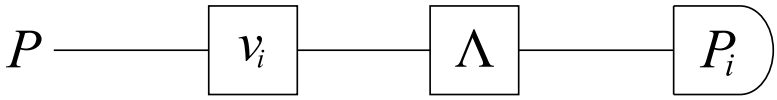


Figure 5.1: Circuit to measure $t_i = \frac{1}{2^n}\mathrm{tr}\,(\Lambda(P_i)P_i)$, where $P_i \in \mathcal{P}_n$ such that $\mathrm{wt}(P_i) = \omega$. Here, $P \in \mathcal{D}$ has weight $\omega$ and, in the tensor product form, its identity terms are at the same positions than the identity terms of $P_i$. The operator $v_i$ represents a sequence of single-spin $\pi/2$ such that $P_i = v_i P {v_i}^\dagger$.

In the scheme presented above, it is implied that $\Lambda$ is the error associated to an experimental implementation of the identity gate. However, as it is shown in [66], this scheme can be extended to the case for which the gate to be certified is an element of the Clifford group. This can easily be understood. Let $\Lambda$ be the error associated to some unitary gate $\mathcal{U}$, and let's assume that we only have access to the imperfect implementation of $\mathcal{U}$. For the following scheme to work, we will see that $\mathcal{U}$ has to be an element of the Clifford group, and that its imperfect implementation can be written in the form $\tilde{\mathcal{U}} = \mathcal{U} \circ \Lambda$. Then, by inserting the identity gate as $\mathcal{U}^\dagger \circ \mathcal{U}$ in the circuit of Figure 5.1, it can be seen that this circuit can be written as in Figure 5.2.

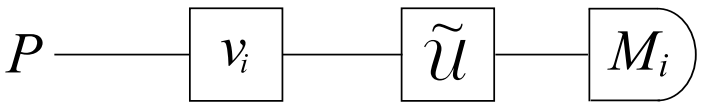


Figure 5.2: Modification of the circuit of Figure 5.1 by inserting the identity gate as $\mathcal{U}^\dagger \circ \mathcal{U}$, where $\mathcal{U}$ is a Clifford and $\tilde{\mathcal{U}} = \Lambda \circ \mathcal{U}$ is its faulty implementation. The measurement $M_i = \mathcal{U}(P_i)$ is also a Pauli operator. This circuit is equivalent to that of Figure 5.1.

In the context of NMR implementations, the circuit of Figure 5.2 needs to be slightly modified in order to account for the fact that we can't measure operators that do not correspond to (-1)-coherences. In other words, it won't always be possible to directly perform the measurement in Figure 5.2. However, there is a workaround using *readout pulses*. Let's say that a Pauli operator $M_i$ can't be directly observed. Then, we can still apply a readout pulse $R$ and then measure a different operator $O_i = RM_iR^\dagger$, where $R$ is chosen so that $O_i$ can be observed in a NMR experiment. Due to the fact that $M_i$ is a Pauli operator, single-spin $\pi/2$ rotations are sufficient to map $M_i$ to another Pauli operator that can be observed. Thus, $R$ is a sequence of single-spin $\pi/2$ rotations and $O_i$ is a Pauli operator. The above explanation is summarized in Figure 5.3

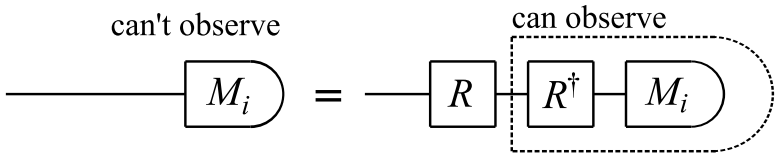


Figure 5.3: Here, $M_i \in \mathcal{P}_n$ is an operator that can't be observed directly in an NMR experiment. However, we can find a sequence $R$ of single-spin $\pi/2$ rotations so that the Pauli operator $O_i = RM_iR^\dagger$ can be directly observed in an NMR experiment.

To account for this experimental constraint, we have to modify the circuit of Figure 5.2. The corrected circuit uses readout pulses and is illustrated in Figure 5.4.

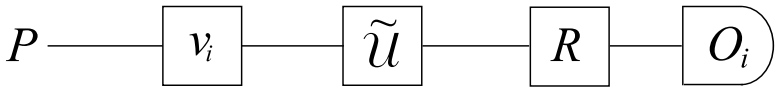


Figure 5.4: Modification of the circuit of Figure 5.2 using a readout pulse $R$ consisting of single-spin $\pi/2$ rotations, and such that the Pauli operator $O_i = RM_iR^\dagger$ can be directly measured in the context of an NMR implementation.

Thus, by repeating the experiment of Figure 5.4 with different $v_i$, we can measure each of the elements of the set $\mathcal{T}_\omega$, and thus estimate the eigenvalue $\lambda_\omega$. Repeating this procedure for all eigenvalues, we can then calculate the probability of no error with Eq.(5.19). Given that $\Pr(0) = [\chi]_{00}$, we can then calculate the average fidelity using Eq.(5.11).

In this section, we have presented a twirling protocol to estimate the average fidelity of Clifford gates. Although in practice we only have access to noisy measurements, repetitions can be used to decrease the noise. Therefore, in the following sections we won't consider the presence of noise in the measurements. How many elements of $\mathcal{T}_\omega$ do we need to measure in order to estimate $\lambda_\omega$ to some desired accuracy? Two approaches will be explored in order to answer this question. The first one uses an analytical result known as the Hoeffding's inequality. The second approach uses Monte Carlo simulations.

## 5.3 Statistical analysis

In the previous section, we have shown that the average fidelity of Clifford gates can be estimated by measuring the eigenvalues of the $\mathcal{C}_1\Pi$ twirled channel. We also showed that each of these eigenvalues can be written down as the statistical mean of a set of measured expectation values. In principle, measuring all of these expectation values is unnecessary if one only desires to approximate the mean. How many of these expectation values do we need to measure in order to reach a desired accuracy? This is the question addressed in the section. We will follow the work of J. Emerson et al. [67] and use two known results in probability and statistics: the Hoeffding's inequality, and the union bound.

The *Hoeffding's inequality* [68] is a general result in probability and statistics that we are going to use in this section. It states that if $x_1, \ldots, x_N$ are independent realizations of a random variable $X$, confined to the interval $[a, b]$ and with statistical mean $\mathbb{E}(X) = \mu$, then for any $\delta > 0$ we have

$$\Pr(|\bar{X} - \mu| > \delta) \leq 2e^{-2\delta^2 N/(b-a)^2}, \tag{5.24}$$

where $\bar{X} = \frac{1}{N}\sum_{i=1}^{N} x_i$ is the estimator of the exact mean $\mu$, and where $\Pr(\mathcal{E})$ denotes the probability of event $\mathcal{E}$. In other words, the Hoeffding's inequality provides an upper bound to the probability that the estimated mean is off by a value greater than $\delta$.

We now apply Hoeffding's inequality to the random variable $T_\omega$, which was defined in the previous section as a uniformly distributed random variable that can take any of the $3^\omega\binom{n}{\omega}$ values in the set

$$\mathcal{T}_\omega = \{t_i \mid t_i = \tfrac{1}{2^n}\mathrm{tr}\left(\Lambda(P_i)P_i\right),\ P_i \in \mathcal{P}_n,\ \mathrm{wt}(P_i) = \omega\}.$$

We see that $T_\omega$ is bounded to the interval $[-1, 1]$. Our goal to estimated the mean $\mathbb{E}(T_\omega) = \lambda_\omega$. Let $t_1, \ldots, t_{k_\omega}$ be independent realizations of $T_\omega$. The estimator of $\lambda_\omega$ is hence $\tilde{\lambda}_\omega = \frac{1}{k_\omega}\sum_{i=1}^{k_\omega} t_i$, and from Hoeffding's inequality it follows that for any $\delta > 0$,

$$\Pr_{\mathcal{E}_\omega} := \Pr\left(|\tilde{\lambda}_\omega - \lambda_\omega| > \delta\right) \leq 2e^{-\delta^2 k_\omega/2}. \tag{5.25}$$

By taking the natural logarithm of each side of this inequality, we see that the number of realizations required to estimate $\lambda_\omega$ to precision $\delta$ with constant probability obeys

$$k_\omega \leq \frac{2\ln(2/\Pr_{\mathcal{E}_\omega})}{\delta^2}. \tag{5.26}$$

This upper bound is sufficient if we want to estimate a single eigenvalue $\lambda_\omega$. We next use the union bound to extend this result to the estimation of the complete set $\{\lambda_1, \ldots, \lambda_n\}$.

The *union bound* [68] is a general result in probability and statistics that applies for an arbitrary set of possible events $\{\mathcal{E}_1, \ldots, \mathcal{E}_n\}$. Let $\Pr_{\mathcal{E}_\omega}$ denote the probability that event $\mathcal{E}_\omega$ happens, and let $\Pr_{\vee\mathcal{E}_\omega}$ denote the probability that at least one of the possible events happens. Then, the union bound states that

$$\Pr_{\vee\mathcal{E}_\omega} \leq \sum_{\omega=1}^{n} \Pr_{\mathcal{E}_\omega}. \tag{5.27}$$

We now apply this result to our particular problem, in which case $\mathcal{E}_\omega$ denotes the event $|\tilde{\lambda}_\omega - \lambda_\omega| > \delta$. In other words, $\mathcal{E}_\omega$ is the event that $\tilde{\lambda}_\omega$ is outside of the precision $\delta$. Similarly, $\vee\mathcal{E}_\omega$ denotes the event that at least one element of $\{\tilde{\lambda}_1, \ldots, \tilde{\lambda}_n\}$ is outside of the precision $\delta$. Applying the union bound and using Eq.(5.25), it follows that

$$\Pr_{\vee\mathcal{E}_\omega} \leq 2 \sum_{\omega=1}^{n} e^{-\delta^2 k_\omega/2}. \tag{5.28}$$

If we make the assumption that $k_1 = k_2 = \cdots = k_n$, then it follows that

$$\Pr_{\vee\mathcal{E}_\omega} \leq 2n\, e^{-\delta^2 k_\omega/2}. \tag{5.29}$$

Then again, taking the natural logarithm of each side, we find that

$$k_\omega \leq \frac{2\ln(2n/\Pr_{\vee\mathcal{E}_\omega})}{\delta^2}. \tag{5.30}$$

The previous result is an upper bound to the number of independent realizations that are required for estimating each element of the set $\{\lambda_1, \ldots, \lambda_n\}$ to precision within $\delta$ with constant probability. We now discuss the practical limitations of this result.

The problem with the approach presented in this section is that it is useful only when $n$ is large enough. This is due to the fact that this approach works for any random variable confined to $[-1, 1]$, *i.e.* the approach is very general. For our particular problem, the set $\mathcal{T}_\omega$ has $3^\omega \binom{n}{\omega}$ elements. Therefore, if the upper bound on $k_\omega$ is bigger than

$$K_\omega = 3^\omega \binom{n}{\omega}, \tag{5.31}$$

then the results obtained in this section are useless from a practical point of view.

In this section, we have shown how Hoeffding's inequality and the union bound can be used to derive an upper bound on the number of measurements required to estimate the eigenvalues of a twirled channel. We have also shown that this upper bound is an asymptotical result that is useful only when the number of qubits $n$ is large enough. In the next section, we will explore an alternate approach based on Monte Carlo simulations.

## 5.4 Monte Carlo simulations

We have seen that the average fidelity of a quantum channel $\Lambda$ can be obtained from the eigenvalues $\{\lambda_0, \ldots, \lambda_n\}$ of its twirled channel $\bar{\Lambda}_{\mathcal{C}_1\Pi}$. By default we have $\lambda_0 = 1$, but we still need to measure the $n$ remaining eigenvalues. In this section we explore how Monte Carlo simulations can help us understand how many measurements we need to do to approximate these eigenvalues. We explore two noisy channel models and study their statistical properties numerically and analytically. We show that there is a relation between the number of measurements required and the spread in the elements of the $\chi$ matrix of the channel. Using this relation, we numerically study worst case scenarios.

Let's first remind us of the problem that we are interested to solve here. As we have see in section 5.2, the eigenvalues of the twirled channel $\bar{\Lambda}_{\mathcal{C}_1\Pi}$ can be written as

$$\lambda_\omega = \frac{1}{3^\omega \binom{n}{\omega}} \sum_{\mathrm{wt}(P_i \in \mathcal{P}_n)=\omega} t_i, \qquad \text{where } \; t_i = \tfrac{1}{2^n} \mathrm{tr}\left(\Lambda(P_i) P_i\right).$$

The terms $\{t_i\}$ can be measured experimentally, but measuring all of them is unnecessary if one only desires to obtain a reasonable approximation. How many of these $t_i$ do we need to measure in order to get a good estimate of $\lambda_\omega$? In the previous section, we saw that Hoeffding's inequality can be applied to this problem, but only to derive an asymptotical result that is useful when the number $n$ of qubits is large enough. Here, we study an alternate approach, based on *Monte Carlo simulations*, that aims to estimate the standard error in the estimator of $\lambda_\omega$ as a function of the number of measurements.

Let us first discuss the notation that we will use in the rest of this section. As the reader already knowns, in probability theory, the average, the variance and the standard deviation of a random variable $X$ are usually denoted respectively by $\mathbb{E}[X]$, $\mathrm{Var}(X)$ and $\mathrm{Std}(X)$. Here, we will extend this notation to deterministic sets and vectors. Let $S = \{s_1, s_2, \ldots, s_N\}$ be a set with deterministic elements, and let $\boldsymbol{v} = (v_1, v_2, \ldots, v_M)^\top$ be a vector with deterministic components. Then, we have the following notation rules

$$\begin{aligned}
\mathbb{E}_S[S] &= \frac{1}{N}\sum_{i=1}^{N} s_i, & \mathbb{E}_V[\boldsymbol{v}] &= \frac{1}{M}\sum_{i=1}^{M} v_i, \\
\mathrm{Var}_S(S) &= \frac{1}{N}\sum_{i=1}^{N} s_i^2 - \mathbb{E}_S[S]^2, & \mathrm{Var}_V(\boldsymbol{v}) &= \frac{1}{M}\sum_{i=1}^{M} v_i^2 - \mathbb{E}_V[\boldsymbol{v}]^2, \\
\mathrm{Std}_S(S) &= \sqrt{\mathrm{Var}_S(S)}, & \mathrm{Std}_V(\boldsymbol{v}) &= \sqrt{\mathrm{Var}_V(\boldsymbol{v})}.
\end{aligned}$$

The reason for this notation is that we will often store the possible outcomes of uniformly distributed random variables into sets or vectors. Thus, this notation provides a shortcut when we want to denote statistical properties of such random variables.

We now return to the problem of estimating an eigenvalue $\lambda_\omega$ of the twirled channel. The set of all possible measurements for a given $\lambda_\omega$ is

$$\mathcal{T}_\omega = \{t_i \mid t_i = \tfrac{1}{2^n}\mathrm{tr}\left(\Lambda(P_i)P_i\right),\ P_i \in \mathcal{P}_n,\ \mathrm{wt}(P_i) = \omega\}.$$

In section 5.2, we have shown that $\mathbb{E}_S[T_\omega] = \lambda_\omega$. Now let's choose at random $k_\omega$ different elements of this set. In other words, we choose a random subset $\mathcal{I} \subset \mathcal{T}_\omega$ such that $|\mathcal{I}| = k_\omega$. The average value $\mathbb{E}_S[\mathcal{I}]$ of this subset is a realization of the *estimator* of $\lambda_\omega$. The estimator of $\lambda_\omega$ is denoted $\tilde{\lambda}_\omega$ and is itself a random variable, meaning that if we repeat the process of choosing a random subset of $\mathcal{T}_\omega$ and take its average value, then for $k_\omega$ small enough we will most likely get a different value than the one previously obtained. Obviously, we have $\mathbb{E}[\tilde{\lambda}_\omega] = \lambda_\omega$ for any value of $k_\omega$, and here we are interested in the uncertainty in the estimator as a function of $k_\omega$. Specifically, we will study the standard deviation of $\tilde{\lambda}_\omega$ as a function of $k_\omega$. Of course, without the ability to make educated assumptions about the specific quantum channel to be certified, the best we can do is to study a large number of randomly chosen channels. Here, we will consider Pauli channels with average fidelity $\bar{F} \in [0.7, 1]$, and we will later show why this analysis should be sufficient. In the following, we describe a first approach to generate such random Pauli channels.

Many algorithms for generating quantum channels could have been explored, and many types of channels with different properties could have been studied. The goal here is to show how the general procedure works, and propose models that are relevant. In the following, we present one way of generating random Pauli channels with desired average fidelity. The first step in generating a random Pauli channel is to choose uniformly at random its average fidelity $\bar{F}$ in the interval $[0.7, 1]$, and then calculate the probability of no error as $\Pr(0) = \frac{(2^n+1)\bar{F}-1}{2^n}$. Next, we choose the other probabilities $\{\Pr(1), \ldots, \Pr(n)\}$ uniformly at random in the interval $[0, 1]$, and then divide them by a same constant such that they sum up to $1 - \Pr(0)$. Then, we have to generate the elements of the $\chi$ matrix, which is a diagonal matrix since we consider Pauli channels. We have already shown that the relationship between the elements of $\chi$ and the probabilities of errors is given by

$$\Pr(\omega) = \sum_{\mathrm{wt}(P_i \in \mathcal{P}_n) = \omega} [\chi]_{ii}.$$

In particular, this implies that $[\chi]_{00} = \Pr(0)$. The strategy to choose the remaining entries of $\chi$ is again to generate random sets with elements in $[0, 1]$ and then normalize them so that they sum up to their corresponding $\Pr(\omega)$. In summary, the idea is to start from the average fidelity of the channel, then choose randomly the elements of $\{\Pr(1), \ldots, \Pr(n)\}$, and finally choose randomly the entries of the $\chi$ matrix. This method for generating random Pauli channels is summarized in the pseudo-code below.

Choose $\bar{F}$ uniformly at random in $[0.7, 1]$

Compute $\Pr(0) = \frac{(2^n+1)\bar{F}-1}{2^n}$

Choose the elements of $\{\Pr(\omega)|\omega = 1, \ldots, n\}$ uniformly at random in [0, 1]

Divide them by a same constant s.t. $\sum_{\omega=1}^{n} \Pr(\omega) = 1 - \Pr(0)$

**for** $\omega = 0 : n$ **do**

  Choose the $\{[\chi]_{ii} \mid \mathrm{wt}(P_i \in \mathcal{P}_n) = \omega\}$ uniformly at random in $[0, 1]$

  Divide them by a same constant s.t. $\sum_{\mathrm{wt}(P_i \in \mathcal{P}_n)=\omega} [\chi]_{ii} = \Pr(\omega)$

**end**

**Algorithm 3:** Pseudo-code to generate a random Pauli channel with $0.7 \leq \bar{F} \leq 1$.

We now describe how we study the standard deviation of the estimator $\tilde{\lambda}_\omega$ as a function of the number of measurements $k_\omega$. The first step is to generate a random Pauli channel using the algorithm described above. Then, for each value of $\omega \in \{1, \ldots, n\}$, we compute the standard deviation of the estimator $\tilde{\lambda}_\omega$ for each value of $k_\omega \in \{1, \ldots, 3^\omega \binom{n}{\omega}\}$. We repeat the whole process a large number of times and we average over a sufficiently large number of random Pauli channels. The details of the algorithm are summarized in the pseudo-code below. The output is the standard deviation of the estimator $\tilde{\lambda}_\omega$ as a function of the number of measurements $k_\omega$. The standard deviation is averaged over a large number of random Pauli channels, and is thus denoted $\overline{\mathrm{Std}}$.

Generate a random Pauli channel $\Lambda$

**for** $\omega = 1 : n$ **do**

  Compute the set $\mathcal{T}_\omega = \{t_i \mid t_i = \frac{1}{2^n}\mathrm{tr}\left(\Lambda(P_i)P_i\right),\ P_i \in \mathcal{P}_n,\ \mathrm{wt}(P_i) = \omega\}$

  **for** $k_\omega = 1 : 3^\omega \binom{n}{\omega}$ **do**

    **for** $j = 1 : N$ **do**

      Choose a subset $\mathcal{I} \subset \mathcal{T}_\omega$ at random and s.t. $|\mathcal{I}| = k_\omega$

      Compute $\mathbb{E}_S[\mathcal{I}]$ and store this value at position $j$ in vector $\tilde{\boldsymbol{\lambda}}_\omega$

    **end**

    Compute $\mathrm{Std}_V(\tilde{\boldsymbol{\lambda}}_\omega)$ and store this value at position $k_\omega$ in vector $\mathbf{std}_\omega$

  **end**

**end**

Repeat a large number of times and average over all random Pauli channels

**Algorithm 4:** Monte Carlo algorithm for estimating the standard deviation of the estimator $\tilde{\lambda}_\omega$ as a function of the number of measurements $k_\omega$. Here, $N$ is a number sufficiently large. The standard deviation is averaged over a large number of channels.

We performed this Monte Carlo simulation considering $n = 4$ qubits and taking the average over 300 random Pauli channels. The results are given in Figure 5.5. We see that the standard deviation is quite small even for small values of $k_\omega$. This is intuitively due to the variance in the elements of the $\chi$ matrix. In fact, we can show that there is a relationship between the variance of $\chi$ and the variance of $\mathcal{T}_\omega$.

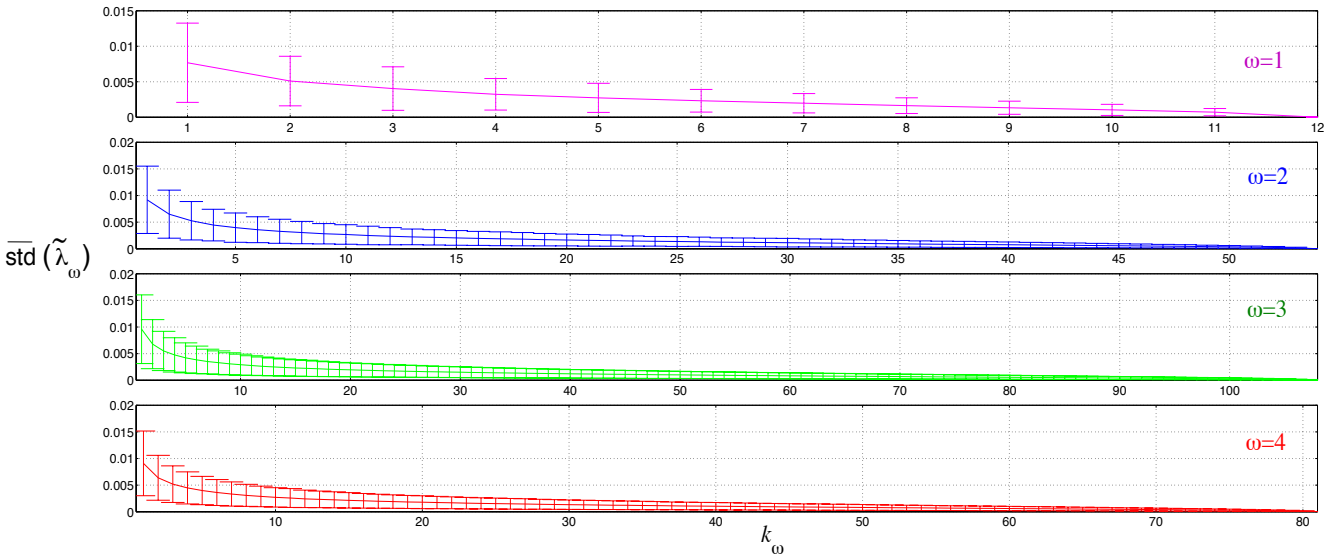


Figure 5.5: Monte Carlo simulations for $n = 4$. Each graph corresponds to a specific value of $\omega$. The $y$-axis is the average standard deviation of the estimator $\tilde{\lambda}_\omega$, and the $x$-axis is the number of measurements. The right limit of each graph is $K_\omega$. The average is taken over 300 random Pauli channels with $0.7 \leq \bar{F} \leq 1$, and the error bar's length is twice the standard deviation over these 300 channels. The average values of $\lambda_\omega$ for these 300 channels from $\omega = 1$ to $\omega = 4$ are 0.858, 0.841, 0.825, and 0.818. The standard error is very low even for small $k_\omega$. We did not plot the variance of $\Pr(0)$ since it depends on many parameters, *i.e.* $k_1$, $k_2$, $k_3$ and $k_4$. From Eq.(5.19), we see that the error bar on $\Pr(0)$ is a linear combination of the error bars from the $\{\tilde{\lambda}_\omega\}$.

We now derive the relationship between the variance in the elements of the $\chi$ matrix and the variance in the elements of $\mathcal{T}_\omega = \{t_i \mid t_i = \frac{1}{2^n}\mathrm{tr}\left(\Lambda(P_i)P_i\right),\ P_i \in \mathcal{P}_n,\ \mathrm{wt}(P_i) = \omega\}$. For a general channel $\Lambda$, we have that

$$\Lambda(P_i) = \sum_{P_j, P_k \in \mathcal{P}_n} [\chi]_{jk} P_j P_i P_k = \sum_{P_j, P_k \in \mathcal{P}_n} (-1)^{c_{ik}} [\chi]_{jk} P_j P_k P_i, \tag{5.32}$$

where

$$c_{ik} = \begin{cases} 0 & \text{if } P_i \text{ and } P_k \text{ commute} \\ 1 & \text{if } P_i \text{ and } P_k \text{ anti-commute.} \end{cases} \tag{5.33}$$

This is due to the fact that Pauli operators either commute or anti-commute with each others. From this, it follows that we can write down $t_i$ as

$$t_i = \tfrac{1}{2^n}\mathrm{tr}\left(\Lambda(P_i)P_i\right) = \sum_{P_j \in \mathcal{P}_n} (-1)^{c_{ij}} [\chi]_{jj}. \tag{5.34}$$

Taking the variance of the set $\mathcal{T}_\omega$, as described at the beginning of this section, we obtain

$$\mathrm{Var}_S(\mathcal{T}_\omega) = \frac{1}{3^\omega \binom{n}{\omega}} \left( \sum_{\mathrm{wt}(P_i \in \mathcal{P}_n)=\omega} {t_i}^2 \right) - {\lambda_\omega}^2. \tag{5.35}$$

From the above equation, it seems that we should be looking for an expression for ${t_i}^2$. From Eq.(5.34), we obviously have that

$$\begin{aligned} {t_i}^2 &= \left( \sum_{P_j \in \mathcal{P}_n} (-1)^{c_{ij}} [\chi]_{jj} \right) \left( \sum_{P_k \in \mathcal{P}_n} (-1)^{c_{ik}} [\chi]_{kk} \right) \\ &= \sum_{P_j, P_k \in \mathcal{P}_n} (-1)^{c_{ij}+c_{ik}} [\chi]_{jj} [\chi]_{kk} \\ &= \sum_{P_j \in \mathcal{P}_n} {[\chi]_{jj}}^2 + \sum_{\substack{P_j, P_k \in \mathcal{P}_n \\ (P_j \neq P_k)}} (-1)^{c_{ij}+c_{ik}} [\chi]_{jj} [\chi]_{kk}. \end{aligned} \tag{5.36}$$

Therefore, it follows that

$$\begin{aligned} \sum_{\mathrm{wt}(P_i \in \mathcal{P}_n)=\omega} {t_i}^2 &= \sum_{\mathrm{wt}(P_i \in \mathcal{P}_n)=\omega} \left( \sum_{P_j \in \mathcal{P}_n} {[\chi]_{jj}}^2 + \sum_{\substack{P_j, P_k \in \mathcal{P}_n \\ (P_j \neq P_k)}} (-1)^{c_{ij}+c_{ik}} [\chi]_{jj} [\chi]_{kk} \right) \\ &= 3^\omega \binom{n}{\omega} \sum_{P_j \in \mathcal{P}_n} {[\chi]_{jj}}^2 + \sum_{\mathrm{wt}(P_i \in \mathcal{P}_n)=\omega} \left( \sum_{\substack{P_j, P_k \in \mathcal{P}_n \\ (P_j \neq P_k)}} (-1)^{c_{ij}+c_{ik}} [\chi]_{jj} [\chi]_{kk} \right) \\ &\approx 3^\omega \binom{n}{\omega} \sum_{P_j \in \mathcal{P}_n} {[\chi]_{jj}}^2, \end{aligned} \tag{5.37}$$

where the last line follows from the fact that the second term is very small (typically less than 2% of the full value), and can thus be neglected to a very good approximation. From Eq.(5.35), it follows that the variance in the elements of $\mathcal{T}_\omega$ is given by

$$\mathrm{Var}_S(\mathcal{T}_\omega) \approx \left( \sum_{P_j \in \mathcal{P}_n} {[\chi]_{jj}}^2 \right) - {\lambda_\omega}^2. \tag{5.38}$$

Now, let $\boldsymbol{\chi}_{diag}$ denote the vector containing the diagonal entries of the $\chi$ matrix. Given that $\chi$ has dimensions $4^n \times 4^n$ and that $\mathrm{tr}(\chi) = 1$, it follows that the variance of $\boldsymbol{\chi}_{diag}$ is

$$\mathrm{Var}_V(\boldsymbol{\chi}_{diag}) = \frac{1}{4^n} \left( \sum_{P_j \in \mathcal{P}_n} {[\chi]_{jj}}^2 \right) - \left( \frac{1}{4^n} \right)^2. \tag{5.39}$$

We see that for a fixed value of $\lambda_\omega$, the variance of $\mathcal{T}_\omega$ increases as the variance in the diagonal entries of $\chi$ increases. For a given set of probabilities $\{\Pr(\omega)\}$, the variance of $\mathcal{T}_\omega$ is therefore maximized by choosing the matrix $\chi$ such that its diagonal entries have maximal variance. This is done by choosing that only $n+1$ entries of the diagonal of $\chi$ are non zero with value equal to one of the elements of $\{\Pr(\omega)\}$. We can now start to think about studying some kind of worst case scenario. Namely, we will still consider random Pauli channels with $0.7 \leq \bar{F} \leq 1$, but the elements of the $\chi$ matrix will now be chosen randomly with the constraint that they must maximize the variance of their distribution. According to our proof, this ensures that the elements of $\mathcal{T}_\omega$ will also have a maximized variance. Moreover, as we have shown above, for a fixed $\lambda_\omega$ we have that $\mathrm{Var}(\mathcal{T}_\omega)$ depends mainly on the variance in the diagonal entries of the $\chi$ matrix. This implies that considering Pauli channels is sufficient. Hence, the Monte Carlo simulation will effectively correspond to a worst case scenario, even if we only consider Pauli channels. This method to generate random Pauli channels is summarized in the pseudo-code below.

1 Choose $\bar{F}$ uniformly at random in $[0.7, 1]$

2 Compute $\Pr(0) = \frac{(2^n+1)\bar{F}-1}{2^n}$

3 Choose the elements of $\{\Pr(\omega)|\omega = 1, \ldots, n\}$ uniformly at random in [0, 1]

4 Divide them by a same constant s.t. $\sum_{\omega=1}^{n} \Pr(\omega) = 1 - \Pr(0)$

5 **for** $\omega = 0 : n$ **do**

  Set $i$ by randomly picking one element of the set $\{i \mid \mathrm{wt}\,(P_i \in \mathcal{P}_n) = \omega\}$

  Set $[\chi]_{ii} = \Pr(\omega)$

**end**

**Algorithm 5:** Pseudo-code to generate a random Pauli channel with $0.7 \leq \bar{F} \leq 1$ and maximized variance. Only $n+1$ entries of $\chi$ are non zero.

We perform the Monte Carlo simulations again, but now using the above algorithm to generate the random Pauli channels, so as to maximize the variance of the estimator $\tilde{\lambda}_\omega$. Again, we choose the same threshold for the average fidelity and we average over 300 random Pauli channels. The results for $n = 4$ qubits are given in Figure 5.6. Although the standard error is increased roughly an order of magnitude with respect to the previous simulations, only half of the total number of measurements seems to be required in order to have an average standard error less than 0.02. Thus, doing half of the experiments should be enough to have at least this kind of statistical accuracy, since this analysis with Pauli channels can be applied to our particular channel to be certified in experiment as we have demonstrated above. In fact, the standard error can be used as the error bar since $\tilde{\lambda}_\omega$ is Gaussian distributed, as it can be observed from Figure 5.7.

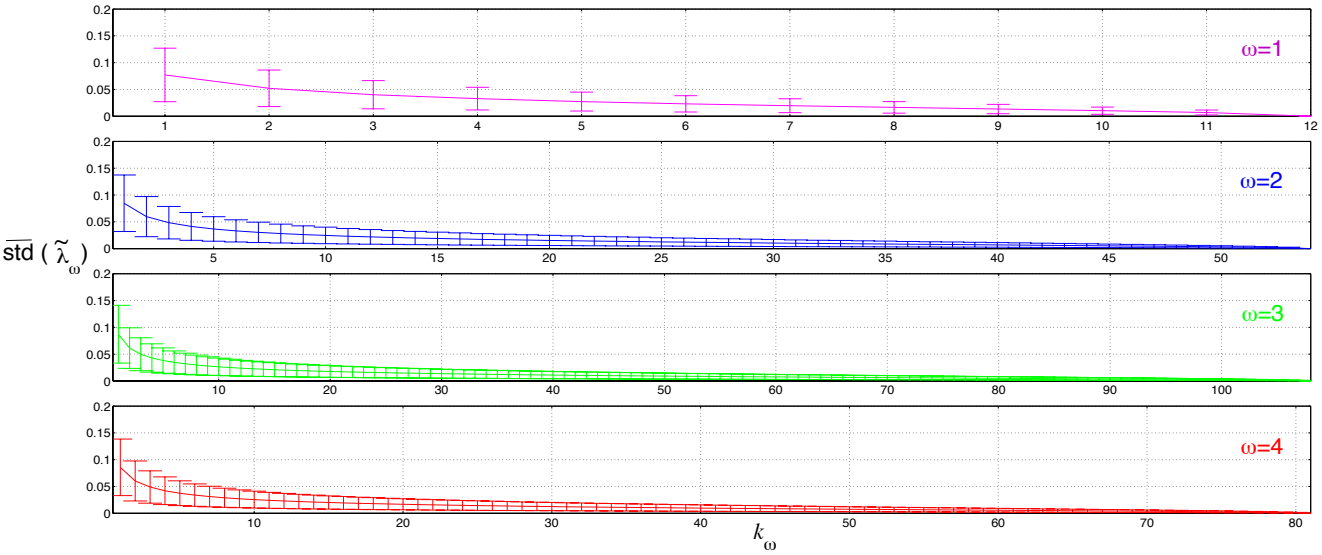


Figure 5.6: Results of the "worst case" Monte Carlo simulations for $n = 4$. Each graph corresponds to a specific $\omega$. The $y$-axis is the average standard deviation of the estimator $\tilde{\lambda}_\omega$, and the $x$-axis is the number of measurements. The right limit of each graph is $K_\omega$. The average is taken over 300 random Pauli channels with $0.7 \leq \bar{F} \leq 1$ and such that the elements of $\chi$ have maximal variance. The average values of $\lambda_\omega$ for these 300 channels from $\omega = 1$ to $\omega = 4$ are 0.864, 0.850, 0.835, and 0.828. The standard error is increased roughly by an order of magnitude compared to Figure 5.5.

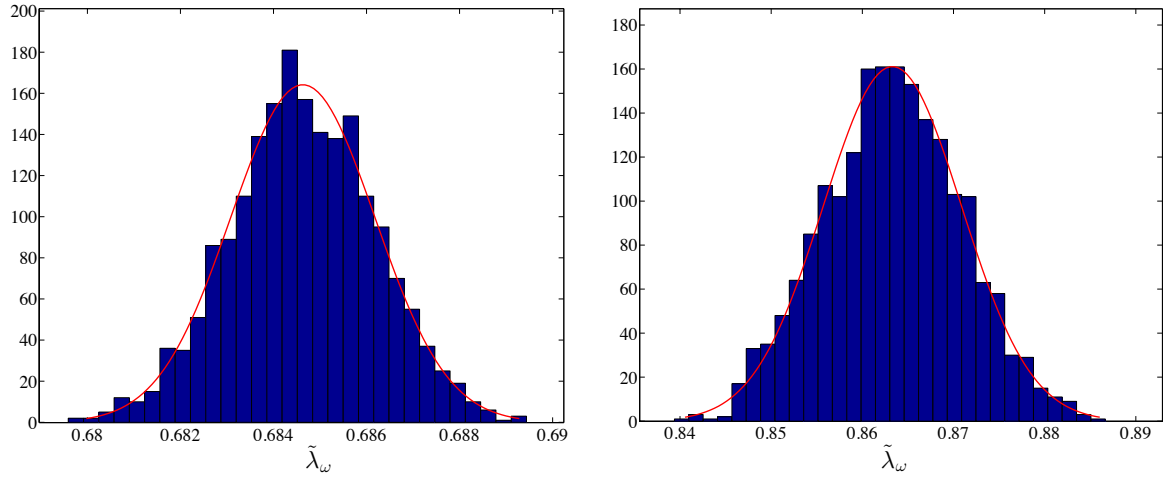


Figure 5.7: Histogram for the distribution of the estimator $\tilde{\lambda}_\omega$ for a 4-qubit random Pauli channel, fitted to a Gaussian distribution. The parameters are $k_\omega = 50$ and $\omega = 3$. The random Pauli channel is generated using **(Left)** Algorithm 3, and **(Right)** Algorithm 5. The two means are different since the two histograms are generated independently.

The histograms displayed in Figure 5.7 give the frequency distribution of the estimator $\tilde{\lambda}_3$ with $k_3 = 50$ for some 4-qubit random Pauli channel. The results are given for a random channel generated using Algorithm 3, and also using Algorithm 5. The two distributions fit well to a Gaussian distribution. Therefore, we could use the confidence interval for Gaussian distributions as the statistical error bar for $\tilde{\lambda}_\omega$.

We now discuss an other important observation to be made from Eq.(5.38). In fact, it can be seen from this expression that the variance in the elements of $\mathcal{T}_\omega$ should be smaller for large values of $\lambda_\omega$. From Eq.(5.16), it can be seen that we have

$$\lambda_\omega = \Pr(0) + \sum_{\omega'=1}^{n} [\Omega]_{\omega,\omega'} \Pr(\omega'), \quad \text{where } |[\Omega]_{\omega,\omega'}| \leq 1. \tag{5.40}$$

It thus follows that as the average fidelity approaches 1, $\Pr(\omega > 0)$ approaches 0 and $\lambda_\omega$ therefore approaches 1 as well. From Eq.(5.38) we conclude that as the average fidelity approaches 1, the variance in the elements of $\mathcal{T}_\omega$ approaches zero. From this observation, we conclude that for channels with an average fidelity that is expected to be high, less measurements should be required. In fact, we can prove and illustrate this point by deriving an upper bound for the variance in $\mathcal{T}_\omega$ as a function of the average fidelity.

First, let's derive a lower bound for $\lambda_\omega$ using Eq.(5.40). We can achieve this by letting $[\Omega]_{\omega,\omega'} = -1$, even though this is not actually true, it does allow us to derive a valid lower bound for $\lambda_\omega$. Using the fact that $\sum_{\omega'=1}^{n} \Pr(\omega') = 1 - \Pr(0)$, we find that

$$\lambda_\omega \geq \Pr(0) - (1 - \Pr(0)) = 2\Pr(0) - 1 \tag{5.41}$$

Next, we focus on deriving an upper bound for the term $\sum_j [\chi]_{jj}{}^2$. Using the convention that $[\chi]_{00} = \Pr(0)$, it follows that the first term in the summation is $\Pr(0)^2$. One can easily understand that the case that maximizes $\sum_j [\chi]_{jj}{}^2$ is when there is only one other term that is nonzero. This term must then be equal to $(1 - \Pr(0))^2$. Thus, we conclude that a valid upper bound for $\sum_j [\chi]_{jj}{}^2$ is

$$\sum_j [\chi]_{jj}{}^2 \leq \Pr(0)^2 + (1 - \Pr(0))^2 = 2\Pr(0)^2 - 2\Pr(0) + 1. \tag{5.42}$$

We now have all the pieces that we need to formulate an upper bound for $\mathrm{Var}_S(\mathcal{T}_\omega)$. In fact, assuming the approximation in Eq.(5.37), and using Eq.(5.38) together with the lower bound (5.41) and the upper bound (5.42), we find this upper bound for $\mathrm{Var}_S(\mathcal{T}_\omega)$

$$\begin{aligned}
\mathrm{Var}_S(\mathcal{T}_\omega) &\leq (2\Pr(0)^2 - 2\Pr(0) + 1) - (2\Pr(0) - 1) \\
\Rightarrow \mathrm{Var}_S(\mathcal{T}_\omega) &\leq 2\Pr(0)^2 - 4\Pr(0) + 2 \\
\Rightarrow \mathrm{Var}_S(\mathcal{T}_\omega) &\leq 2(\Pr(0) - 1)^2 \\
\Rightarrow \mathrm{Std}_S(\mathcal{T}_\omega) &\leq \sqrt{2}|\Pr(0) - 1|.
\end{aligned} \tag{5.43}$$

Now, using the expression $\Pr(0) = \frac{(2^n+1)\bar{F}-1}{2^n}$, we can plot this upper bound as a function of $\bar{F}$, so as to verify if the standard deviation is bounded above by lower values as $\bar{F}$ increases. The results for $n = 3$, $n = 4$ and $n = 6$, are illustrated in Figure 5.8.

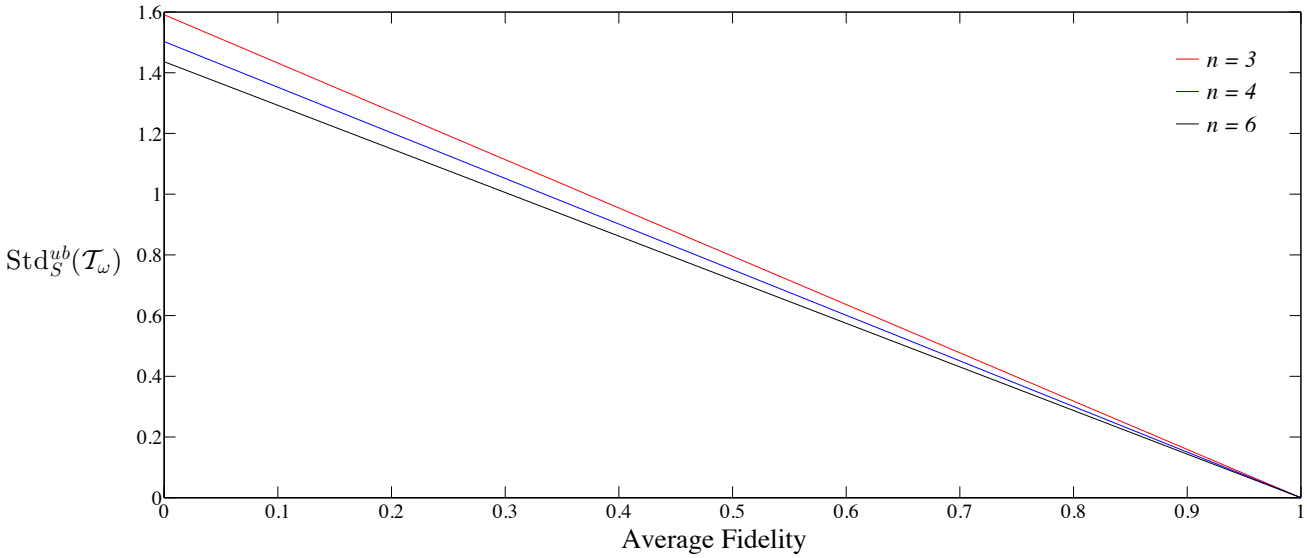


Figure 5.8: Upper bound for the standard deviation of $\mathcal{T}_\omega$ as a function of the average fidelity, assuming the approximation in Eq.(5.37). We see that for $\bar{F} = 1$, the upper bound is at zero, which is a very sensible result. Thus, less experiments should be required for channels with expected high fidelities. As the average fidelity decreases, the upper bound increases following a straight line. The results are given for $n = 3$, $n = 4$ and $n = 6$ qubits.

The graph of Figure 5.8 illustrates perfectly that the standard deviation in the elements of $\mathcal{T}_\omega$ is bounded above by smaller values when the average fidelity is higher, demonstrating that in principle less experiments are required to reach the same statistical accuracy when the average fidelity of the channel is expected to be high. Now wether or not we do have access to this kind of information in reality is a different question.

In this section we have explored how Monte Carlo simulations can help us to estimate how many experiments we need to do in order to approximate the eigenvalues of a twirled channel $\bar{\Lambda}_{\mathcal{C}_1\Pi}$. We considered random Pauli channels with average fidelity $0.7 \leq \bar{F} \leq 1$, but other models could have been explored. The choice of these bounds for the average fidelity is justified by the assumption that the average fidelity of the channel to be certified is expected to be in that range. We derived an equation that shows how the variance in the elements of $\mathcal{T}_\omega$ is related to the variance in the diagonal entries of the $\chi$ matrix. We then used this relation to define a worst case Monte Carlo method, so as to get an idea of how many experiments we should do in the worst cases. The purpose of this chapter was to gain a better understanding of the relation between the $\chi$ matrix of the channel $\Lambda$ to be certified, and the number of experiments that we should do to reach a desired accuracy. In practice, it is not necessary to know the number of experimental runs prior to start the experiment. As we perform the experimental runs we can monitor the variance in the data, and decides wether or not we need to do more experiments. In the next section, we will simulate the twirling certification experiment for a 4-qubit system.

## 5.5 Results for 2,3-Difluorobenzaldehyde

In this section, we apply the twirling protocol of section 5.2 to the task of certifying quantum gates implemented with the oriented spin system of 2,3-Difluorobenzaldehyde. We first consider the 4-qubit proton subsystem of the molecule, and simulate a twirling certification experiment using actual GRAPE pulses, the goal here being to study what happens when the single-spin $\pi/2$ rotations used for preparation and readout are imperfect. Then, we consider the 2-qubit fluorine subsystem, and perform the twirling protocol experimentally to certify the implementation of a controlled-NOT (C-NOT) gate.

### 5.5.1 Simulations for the proton subsystem

In section 5.4, we used Monte Carlo simulations to study the statistical accuracy of the twirling protocol assuming that we had perfect single-spin $\pi/2$ rotations and perfect measurements. Here, we now simulate the single-spin $\pi/2$ rotations using the actual GRAPE pulses found in section 4.2.2 for the 4-qubit proton subsystem of 2,3-Difluorobenzaldehyde. We start by capturing the effect of the imperfect single-spin $\pi/2$ rotations by certifying the *do nothing* operation. Then, we simulate a certification experiment for a Clifford gate that is also simulated from a GRAPE pulse sequence. The experiments simulated in this section were not performed due to the lack of equipment discussed in section 4.2.2.

The first certification experiment is more of a calibration procedure that aims to capture the errors in preparation and readout. It is equivalent to certify the do nothing operation, which is a perfect implementation of the identity gate. The form of the circuit describing each experimental run is illustrated in Figure 5.4 where $\tilde{\mathcal{U}} = I^{\otimes 4}$. In practice, each measurement's value is obtained directly by projecting the simulated final state on the appropriate Pauli operator, rather than by fitting the simulated spectrum. There is a total of 255 experiments that could be simulated. We first start by studying the standard deviation of each estimator $\tilde{\lambda}_\omega$ as a function of the ratio $k_\omega/K_\omega$, were $k_\omega$ and $K_\omega$ are respectively the actual and maximum number of simulated experiments for a specific value of $\omega$. The results are presented in Table 5.1, where the standard deviation of $\tilde{\lambda}_\omega$ is denoted $\sigma_{\tilde{\lambda}_\omega}$. We see that the standard deviations are quite small, which should be expected since we are certifying a *perfect* implementation of the identity gate. However, the average fidelity obtained is less than 1 as we discuss next.

Having performed the simulations, we now compute the probability of no error $\Pr(0)$ and the average fidelity $\bar{F}$. Here, we use all possible experimental runs, *i.e.* $k_\omega = K_\omega$. We obtain $\lambda_1 = 0.987$, $\lambda_2 = 0.980$, $\lambda_3 = 0.958$, and $\lambda_4 = 0.947$. Of course, if we would have used perfect single-spin $\pi/2$ rotations, then each eigenvalue would have been equal to 1. Here, we see that $\lambda_1 > \lambda_2 > \lambda_3 > \lambda_4$. This is in fact expected since the number

of single-spin $\pi/2$ rotations required is in general greater for larger values of $\omega$. Using Eq.(5.19), we obtain $\Pr(0) = 0.960$. Finally, we use Eq.(5.11) with $[\chi]_{00} = \Pr(0)$ to obtain $\bar{F} = 0.962$. Next, we certify a Clifford unitary and we will use the average fidelity of the calibration procedure to rescale the measured average fidelity of the Clifford.

| $k_\omega/K_\omega$ | $\sigma_{\tilde{\lambda}_1}$ $10^{-3}$ | $\sigma_{\tilde{\lambda}_2}$ $10^{-3}$ | $\sigma_{\tilde{\lambda}_3}$ $10^{-3}$ | $\sigma_{\tilde{\lambda}_4}$ $10^{-3}$ |
|---|---|---|---|---|
| 1/6 | 1.225 | 3.985 | 4.912 | 5.724 |
| 1/3 | 0.791 | 2.578 | 3.098 | 3.672 |
| 1/2 | 0.571 | 1.828 | 2.195 | 2.576 |
| 2/3 | 0.392 | 1.333 | 1.579 | 1.860 |
| 5/6 | 0.239 | 0.820 | 0.957 | 1.112 |

Table 5.1: Standard deviation of each estimator $\tilde{\lambda}_\omega$. Here, $k_\omega$ is the number of experiments simulated, and $K_\omega$, given by Eq.(5.31), is the maximum number of experiments for a particular value of $\omega$. These results are obtained by simulation of the GRAPE pulses and are for certifying the do nothing operation in the proton subsystem of 2,3-Difluorobenzaldehyde.

We now simulate the twirling protocol for certifying the Clifford unitary illustrated in Figure 5.9. There is no specific reason for choosing this particular unitary, other than the fact that it has recently been proposed for purpose of quantum error correction. The GRAPE pulse obtained for this unitary has a duration of $8ms$ and was obtained following the steps described in section 4.2.2.

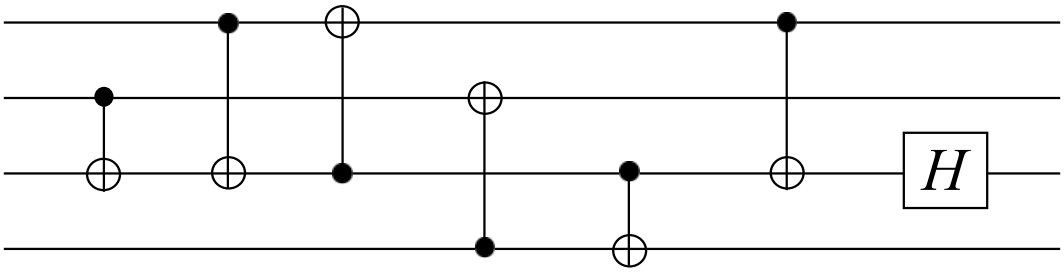


Figure 5.9: Quantum circuit for the Clifford unitary certified in simulation with the 4-qubit proton subsystem of 2,3-Difluorobenzaldehyde. Here, $H$ denotes the Hadamard gate and the other gates are C-NOTs.

Then again, we study the standard deviation of each estimator $\tilde{\lambda}_\omega$ as a function of the ratio $k_\omega/K_\omega$. The results are presented in Table 5.2. Again, to calculate $\Pr(0)$ and $\bar{F}$, we use all possible experimental runs. We find $\lambda_1 = 0.974$, $\lambda_2 = 0.966$, $\lambda_3 = 0.956$ and $\lambda_4 = 0.945$. The probability of no error is thus $\Pr(0) = 0.956$ and the average fidelity is $\bar{F} = 0.958$. Dividing this average fidelity by the one obtained for the calibration procedure, we obtained the average fidelity of the Clifford gate as $\bar{F}_c = 0.996$.

| $k_\omega/K_\omega$ | $\sigma_{\tilde{\lambda}_1}$ $10^{-3}$ | $\sigma_{\tilde{\lambda}_2}$ $10^{-3}$ | $\sigma_{\tilde{\lambda}_3}$ $10^{-3}$ | $\sigma_{\tilde{\lambda}_4}$ $10^{-3}$ |
|---|---|---|---|---|
| 1/6 | 13.488 | 3.851 | 3.867 | 3.821 |
| 1/3 | 7.806 | 2.461 | 2.383 | 2.434 |
| 1/2 | 5.767 | 1.701 | 1.703 | 1.776 |
| 2/3 | 4.052 | 1.228 | 1.219 | 1.262 |
| 5/6 | 2.576 | 0.772 | 0.786 | 0.754 |

Table 5.2: Standard deviation of each estimator $\tilde{\lambda}_\omega$. Here, $k_\omega$ is the number of experiments simulated, and $K_\omega$, given by Eq.(5.31), is the maximum number of experiments for a particular value of $\omega$. These results are obtained by simulation of the GRAPE pulses and are for certifying the Clifford of Figure 5.9 in the proton subsystem of 2,3-Difluorobenzaldehyde.

Then again, we see in Table 5.2 that the standard deviations are quite small. This can easily be understood since the pulses used in simulation all have a fidelity of 98%. As we have shown in section 5.4, a low standard deviation in the estimator $\tilde{\lambda}_\omega$ is expected for gates with high average fidelity. For the Clifford gate illustrated in Figure 5.9, the average fidelity that we obtained in simulation is quite good. This is expected since there are virtually no implementation errors in simulation. Moreover, the $T_2$ effects are negligible for the particular simulations that we performed. In other words, the errors come mainly from the fact that the pulses have a fidelity $\Phi < 1$. Also, due to the fact that $T_2$ errors are negligible in our simulations, we did not design the sequences with the constraint that they must all have the same duration. In experiment, when $T_2$ effects are expected to be comparable to the errors in pulse implementations, we can design identity gates and use them to make all experimental runs have the same duration. However, as mentioned above, doing this is not required in our case.

The goal of this section was mainly to study how the twirling protocol works when the pulses used for preparation and measurements are not perfect. In practice, this implies that we have to perform a calibration procedure to capture the errors in preparation and readout. In this section, we have also shown that we can in fact design a twirling experiment that could be performed in the lab at some point, if the lack of equipment discussed in section 4.2.2 is solved. In other words, we have the GRAPE pulses required to implement the experiments presented here, and the software for designing and analyzing the experiments is also ready. In practice, the design and analysis of the experimental runs is automated with a MATLAB program. In the next section, we present experimental results for the certification of a controlled-NOT gate in the 2-qubit fluorine subsystem of 2,3-Difluorobenzaldehyde. As we will discuss, the results won't be as good as those obtained in this section, mainly due to the fact that we don't use pulse fixing, and that we are performing experiments rather than simulations.

### 5.5.2 Experiments for the fluorine subsystem

We now present experimental results for the fluorine subsystem of 2,3-Difluorobenzaldehyde. We certify the implementation of a C-NOT gate. Then again, the single-spin $\pi/2$ rotations are obtained with our GRAPE algorithm. We also use our algorithm to design pulses for double-spin $\pi/2$ rotations and for the identity gate as well. All of these pulses have a duration of $1.2ms$ and a fidelity of 0.999, averaged over appropriate distributions of chemical shifts and r.f. fields inhomogeneity. We first use randomized benchmarking [66] to get an idea of the average error per gate for the single-spin and double-spin $\pi/2$ rotations. We next present the certification results for the calibration procedure and the C-NOT gate. The measurement values are extracted by fitting the spectra obtained in experiment.

We first use randomized benchmarking [66] to get an idea of the average error per $\pi/2$ rotations. These pulses are not expected to have an experimental fidelity close to their design fidelity since they are implemented without pulse fixing. In this benchmarking experiment, the average fidelity of random pulse sequences that compose to the identity is measured for sequences of different lengths. Because of the fast decay in our spin system, the maximum sequence length that we use is ten. We then fit the average fidelity decay to $F = A_0 p^m + B_0$, where $m$ is the sequence length. Given that $T_1$ is expected to be about $1s$ in our case, we can assume unital gate errors, and thus that $B_0 = 1/2$ [66]. The average error per gate is then given by $r = \frac{1-p}{2}$. We perform the experiment for single- and double-spin $\pi/2$ rotations and obtain the results given in Figure 5.10.

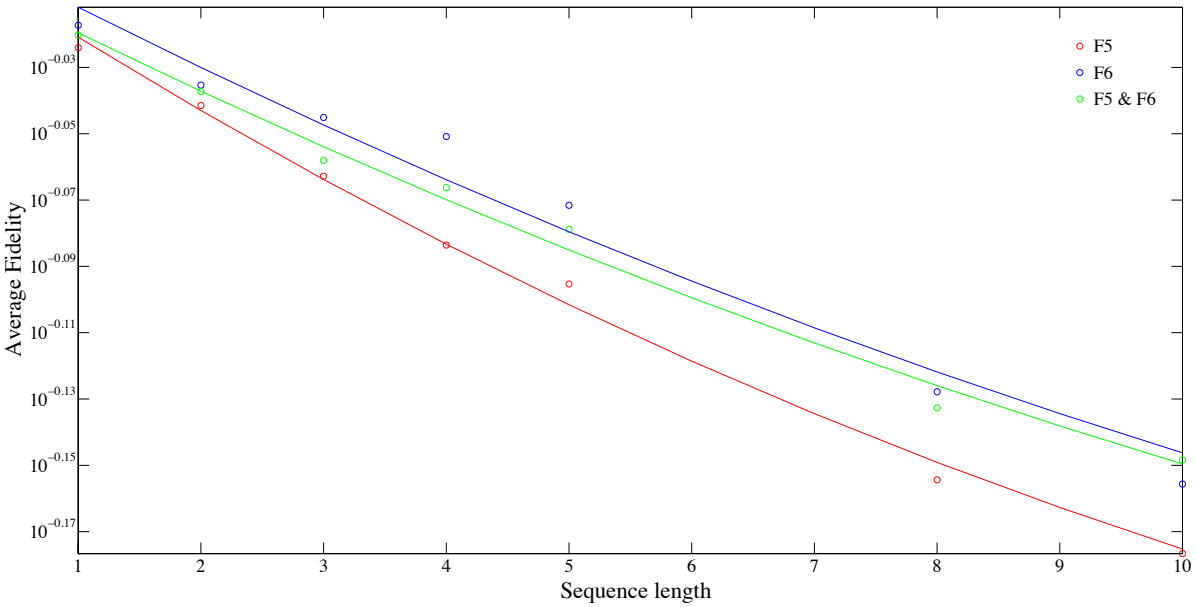


Figure 5.10: Randomized benchmarking of $\pi/2$ rotations. Each of the four first data points is the average fidelity of 4 sequences, and each of the three last data points is the average fidelity of 10 sequences. We find an average error per gate of 0.052 for pulses acting on $F_5$, 0.042 for pulses acting $F_6$, and 0.042 for pulses acting on both $F_5$ and $F_6$.

Here, we do not concern ourself with error bars since the goal is only to get some rough idea of the error per gate. For our single- and double-spin $\pi/2$ rotations, we find an average error per gate of 0.052 for pulses acting on $F_5$, 0.042 for pulses acting $F_6$, and 0.042 for pulses acting on both $F_5$ and $F_6$. Such large errors might be surprising at first, because the design fidelity of the pulses is 0.999, but these errors actually reasonable since the pulses are implemented without pulse fixing. In fact, O. Moussa showed that in a 3-qubit system at solid state, pulse fixing could improve the fidelity very significantly [66].

We now proceed to the calibration step of the twirling certification experiment. This first step aims to capture the errors in preparation and measurements. It is equivalent to certify the *do nothing* operation (*i.e.* doing nothing for a zero amount of time), which is a perfect implementation of the identity gate. The circuit for a generic experimental run is illustrated in Figure 5.11, and the details and experimental results are given in Table 5.3. The error bar for the measurement values is estimated from simulated spectra with gaussian noise added to them. In the table, the notation $(\pi/2)_k^u$ means that a $\pi/2$ rotation is applied to spin $k \in \{1, 2\}$ about the axis $u \in \{\pm x, \pm y, \pm z\}$. In practice, pulses such as $(\pi/2)_1^y(\pi/2)_2^{-x}$ are implemented as a single double-spin $\pi/2$ rotation, and identity pulses are used to make all sequences $2.4ms$ long.

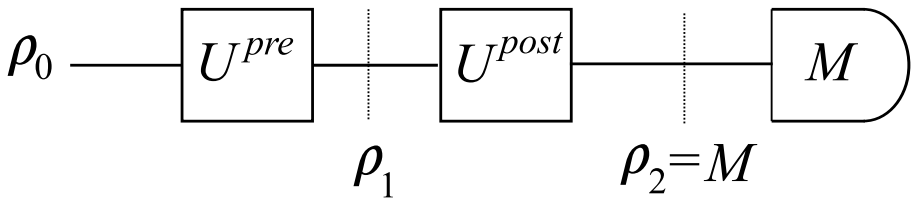


Figure 5.11: Circuit for a generic experimental run for the calibration step. The initial state is denoted $\rho_0$ and is mapped to some Pauli by the preparation operation $U^{pre}$. The readout pulse is denoted $U^{post}$ and the measurement is denoted $M$. We choose that the measurement is equal to the state $\rho_2$, we thus have $\rho_2 = M$. Here, $U^{pre}$ and $U^{post}$ are $1.2ms$ long. The details for the specific values for each experiment are given in Table 5.3.

In practice, the initial states are created using the method explained in section 2.6.3. Using the experimental results of Table 5.3, we calculate that $\lambda_1 = 0.787 \pm 0.002$ and $\lambda_2 = 0.725 \pm 0.002$. This leads to a probability of no error $\Pr(0) = 0.766 \pm 0.002$, and an average fidelity $\bar{F} = 0.813 \pm 0.002$. The average fidelity might seem to be too low, but this is in fact expected. As it was revealed by the randomized benchmarking of $\pi/2$ rotations, in the absence of pulse fixing the average error per $\pi/2$ rotation is about 4-5%, explaining the low average fidelity obtained here.

| Experiment # | $\rho_0$ | $U^{pre}$ | $\rho_1$ | $U^{post}$ | $M$ | $t \pm 0.005$ |
|---|---|---|---|---|---|---|
| 1 | $IZ$ | $(\pi/2)_2^y$ | $IX$ | – | $IX$ | 0.749 |
| 2 | $IZ$ | $(\pi/2)_2^{-x}$ | $IY$ | – | $IY$ | 0.761 |
| 3 | $IZ$ | – | $IZ$ | $(\pi/2)_2^y$ | $IX$ | 0.719 |
| 4 | $ZI$ | $(\pi/2)_1^y$ | $XI$ | – | $XI$ | 0.866 |
| 5 | $ZI$ | $(\pi/2)_1^{-x}$ | $YI$ | – | $YI$ | 0.793 |
| 6 | $ZI$ | – | $ZI$ | $(\pi/2)_1^y$ | $XI$ | 0.835 |
| 7 | $ZZ$ | $(\pi/2)_1^y(\pi/2)_2^y$ | $XX$ | $(\pi/2)_2^{-y}$ | $XZ$ | 0.785 |
| 8 | $ZZ$ | $(\pi/2)_1^y(\pi/2)_2^{-x}$ | $XY$ | $(\pi/2)_2^x$ | $XZ$ | 0.789 |
| 9 | $ZZ$ | $(\pi/2)_1^y$ | $XZ$ | – | $XZ$ | 0.849 |
| 10 | $ZZ$ | $(\pi/2)_1^{-x}(\pi/2)_2^y$ | $YX$ | $(\pi/2)_1^x$ | $ZX$ | 0.672 |
| 11 | $ZZ$ | $(\pi/2)_1^{-x}(\pi/2)_2^{-x}$ | $YY$ | $(\pi/2)_1^x$ | $ZY$ | 0.675 |
| 12 | $ZZ$ | $(\pi/2)_1^{-x}$ | $YZ$ | – | $YZ$ | 0.740 |
| 13 | $ZZ$ | $(\pi/2)_2^y$ | $ZX$ | – | $ZX$ | 0.667 |
| 14 | $ZZ$ | $(\pi/2)_2^{-x}$ | $ZY$ | – | $ZY$ | 0.681 |
| 15 | $ZZ$ | – | $ZZ$ | $(\pi/2)_2^{-x}$ | $ZY$ | 0.668 |

Table 5.3: Details for the specific values of Figure 5.11. The notation $(\pi/2)_k^u$ means that a $\pi/2$ rotation is applied to spin $k \in \{1, 2\}$ about the axis $u \in \{\pm x, \pm y, \pm z\}$. Each sequence is $2.4ms$ long. Here, $t$ is the experiment result of measuring the operator $M$.

In Table 5.3, we see that experiments 8 and 10 have quite different measurement values despite having very similar pulse sequences. The same observation holds for experiments 9 and 13. This might be explained by the imperfection of the decoupling, in which case the differences are due to the different environments of $F_5$ and $F_6$ (*e.g.* the coupling between $H_1$ and $F_5$ is very strong compared to the coupling between $H_4$ and $F_6$).

We now certify the implementation of a C-NOT gate. The circuit for a generic experimental run is illustrated in Figure 5.12, and the details and experimental results are given in Table 5.4. Then again, the error bar for the measurements was estimated from simulated spectra with gaussian noise added to them. Here, we again use identity pulses to make all sequences the same length, *i.e.* $3.6ms$.

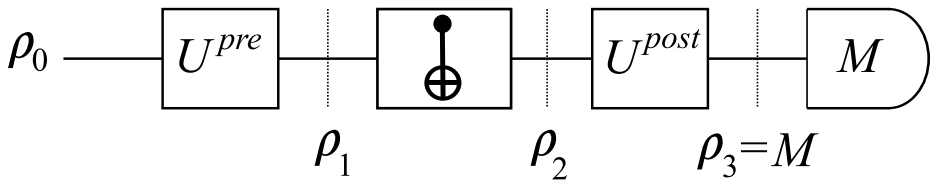


Figure 5.12: Circuit for a generic experimental run for certifying the C-NOT gate. The initial state is denoted $\rho_0$ and is mapped to some Pauli by the preparation operation $U^{pre}$. Then, the C-NOT gate is applied to the state $\rho_1$. The readout pulse is denoted $U^{post}$ and the measurement is denoted $M$. We choose that the measurement is equal to the state $\rho_2$, we thus have $\rho_2 = M$. Here, $U^{pre}$, C-NOT and $U^{post}$ are $1.2ms$ long.

| Experiment # | $\rho_0$ | $U^{pre}$ | $\rho_1$ | $\rho_2$ | $U^{post}$ | $M$ | $t \pm 0.005$ |
|---|---|---|---|---|---|---|---|
| 1 | $IZ$ | $(\pi/2)_2^y$ | $IX$ | $IX$ | – | $IX$ | 0.654 |
| 2 | $IZ$ | $(\pi/2)_2^{-x}$ | $IY$ | $ZY$ | – | $ZY$ | 0.701 |
| 3 | $IZ$ | – | $IZ$ | $ZZ$ | $(\pi/2)_2^y$ | $ZX$ | 0.637 |
| 4 | $ZI$ | $(\pi/2)_1^y$ | $XI$ | $XX$ | $(\pi/2)_1^{-y}$ | $ZX$ | 0.541 |
| 5 | $ZI$ | $(\pi/2)_1^{-x}$ | $YI$ | $YX$ | $(\pi/2)_1^x$ | $ZX$ | 0.616 |
| 6 | $ZI$ | – | $ZI$ | $ZI$ | $(\pi/2)_1^y$ | $XI$ | 0.695 |
| 7 | $ZZ$ | $(\pi/2)_1^y(\pi/2)_2^y$ | $XX$ | $XI$ | – | $XI$ | 0.772 |
| 8 | $ZZ$ | $(\pi/2)_1^y(\pi/2)_2^{-x}$ | $XY$ | $YZ$ | – | $YZ$ | 0.756 |
| 9 | $ZZ$ | $(\pi/2)_1^y$ | $XZ$ | $-YY$ | $(\pi/2)_2^{-x}$ | $YZ$ | 0.602 |
| 10 | $ZZ$ | $(\pi/2)_1^{-x}(\pi/2)_2^y$ | $YX$ | $YI$ | – | $YI$ | 0.598 |
| 11 | $ZZ$ | $(\pi/2)_1^{-x}(\pi/2)_2^{-x}$ | $YY$ | $-XZ$ | – | $-XZ$ | 0.786 |
| 12 | $ZZ$ | $(\pi/2)_1^{-x}$ | $YZ$ | $XY$ | $(\pi/2)_2^x$ | $XZ$ | 0.645 |
| 13 | $ZZ$ | $(\pi/2)_2^y$ | $ZX$ | $ZX$ | – | $ZX$ | 0.528 |
| 14 | $ZZ$ | $(\pi/2)_2^{-x}$ | $ZY$ | $IY$ | – | $IY$ | 0.628 |
| 15 | $ZZ$ | – | $ZZ$ | $IZ$ | $(\pi/2)_2^y$ | $IX$ | 0.629 |

Table 5.4: Details for the specific values of Figure 5.12. The notation $(\pi/2)_k^u$ means that a $\pi/2$ rotation is applied to spin $k \in \{1, 2\}$ about the axis $u \in \{\pm x, \pm y, \pm z\}$. Each sequence is $3.6ms$ long. Here, $t$ is the experiment result of measuring the operator $M$.

Using the results of Table 5.4, we calculate that $\lambda_1 = 0.641 \pm 0.002$ and $\lambda_2 = 0.661 \pm 0.002$. This leads to a probability of no error $\Pr(0) = 0.674 \pm 0.002$, and an average fidelity $\bar{F} = 0.740 \pm 0.002$. In order to factor away the errors and preparation and measurement, we can define the calibrated fidelity as $\bar{F}_c = 0.740/0.813 = 0.910$. Here, we must emphasize that this last step is very tricky. In fact, due to the fact that we do not use pulse fixing, our $\pi/2$ rotations have average errors of about 4-5%. Thus whether or not these errors are factorable is not an easy question and is beyond the scope of this work. Assuming that the errors in preparation and measurements can be factored away, then the average fidelity of the C-NOT gate is about 91%. Then again, this low average fidelity is most likely explained by the fact that we do not use pulse fixing, due to a lack of equipment. Let's now look at the standard deviation of these results. The standard deviation is 0.0589 for the results of experiments 1 - 6 and 0.0898 for the results of experiments 7 - 15. Assuming random Pauli channels with $0.85 < \bar{F} < 0.95$, basic Monte Carlo simulations, such as those of Figure 5.5, tell us that the average standard deviation is about 0.02 for both sets of experiments. On the other hand, worst case Monte Carlo simulations, such as those in Figure 5.6, tell us that it is about 0.09. Here, a strong experimental standard deviation is reasonable since we use imperfect gates for preparations and measurements. Examples of fitted experimental spectra are shown in Figure 5.13.

In this section, we have presented experimental results of certifying the implementation of a C-NOT gate in the fluorine subsystem of 2,3-Difluorobenzaldehyde. A benchmarking

experiment was first performed in order to estimate the average error per $\pi/2$ rotations, and found an average error per gate of about 4-5%. This large error per gate is most likely explained by the fact that we do not use pulse fixing. For the C-NOT gate, assuming that the errors from preparation and measurements can be factored away, we found an average fidelity of about 91%. Again, such a result is reasonable since we do not use pulse fixing.

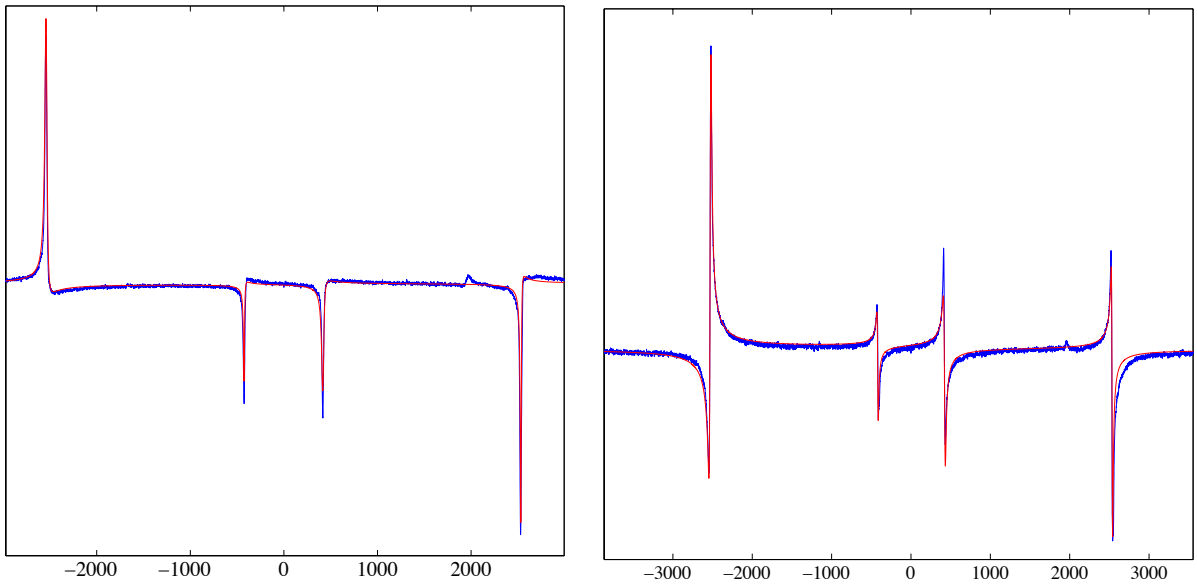


Figure 5.13: Fitting (red) of the experimental spectrum (blue) for **(Left)** experiment # 8 in certifying the identity, and **(Right)** experiment # 9 in certifying the C-NOT. The quality of the fitting for these spectra is representative of the fitting for the other spectra.

This concludes this chapter on certification of quantum gates. We have presented the twirling certification protocol by O. Moussa [66], and explained how it allows us to estimate the average fidelity of Clifford gates. Next, we presented the usual statistical analysis to obtain bounds for the accuracy of this method. We also proposed a Monte Carlo method in order to further investigate the accuracy of twirling experiments. In addition, we derived analytical formula that relate the statistical accuracy of the twirling protocol to the variance in the diagonal entries of the $\chi$ matrix of the channel to be certified. We also showed how quantum channels with average fidelities that are expected to be high will require less experimental runs to reach a same desired statistical accuracy. We then presented experiments and simulations for certifying the implementation of quantum gates in the spin system of 2,3-Difluorobenzaldehyde. For the 4-qubit subsystem, we were not able to perform the experiments due to a lack of experimental equipment. However, we designed the software to design and analyze such experiments, and performed some simulations as a demonstration that we should be able to perform such experiments in practice. For the 2-qubit subsystem, we performed twirling certification experiments, but without pulse fixing. We obtained an average fidelity of 91% for the implementation of a controlled-NOT gate. This result could be improved significantly by using pulse fixing.

# Chapter 6

# Conclusion

Quantum computers have the potential to revolutionize the world of information processing by solving some problems more efficiently than their classical counterparts. Quantum algorithms can however be quite challenging to implement in practice, and the quest is then to search for physical systems that have the potential for the realization of quantum information devices on a large scale. To this day, liquid state NMR has been the forerunner in the experimental demonstrations of quantum algorithms. In liquid state NMR, mutual couplings among the spins are provided by the scalar couplings. In contrast, in the liquid crystal state, the intramolecular dipolar couplings, which have larger magnitudes and longer ranges, survive and can be used for purposes of quantum information processing. More importantly, the liquid crystal state offers advantages such as an increased clock frequency and a faster recycling of algorithms. These advantages come to the cost of a more complicated internal Hamiltonian, which makes the system harder to control and characterize in practice. This thesis has promoted liquid crystal NMR quantum computing by presenting methods and results towards solving these problems.

The main contribution offered in this thesis is that of chapter 3, were we proposed a new method for analyzing NMR spectra of solutes dissolved in liquid crystals, and applied it to solve a 6-spin system with very low symmetry in structure. This was achieved without the use of *a priori* knowledge or assumptions on the interspin distances or order parameters, which is in contrast with the results in previous experiments [14,17–20,30,31,33,35–39,48]. Our method includes a new spectral analysis algorithm - NAFONS. In contrast with traditional pure frequency fitting methods [16–24], NAFONS does not require spectral assignment, and is thus fully automatic. In contrast with line shape fitting methods [28–39], evaluation of our objective function does not involve the expensive computation of the spectral line shape, and the global optimization strategy can cope with a large search space. Our method also includes new experimental techniques to simplify spectral analysis for extracting the dipolar couplings between heteronuclear spins. We believe that our

results should be helpful to implement spectral analysis of dipolar coupled systems, and can be extended to larger systems.

In chapter 4, we presented the well-known GRAPE pulse sequence design algorithm, and we also explained how to design pulses that are robust to variations in the r.f. amplitudes and Hamiltonian parameters. We also discussed how the search can be fasten using a subsystem approach, and also how pulse smoothing and pulse fixing can help to reduce errors occurring in practical implementations. In that chapter, we explored how well these methods can be used in practice to control spin systems dissolved in liquid crystals. We worked with the same 6-spin system that was characterized in the previous chapter, and the goal was to find single-spin $\pi/2$ rotations. First considering the full 6-spin system, we found pulse design to be highly challenging in this case. In fact, we were unable to find pulses with fidelity above 95%, and these were neither robust nor smooth. Then, we restricted ourselves to the 4-qubit subsystem, in which case we were able to find robust smooth pulses with 98% fidelity and $4ms$ length. Thus, even with the GRAPE algorithm, controlling oriented spin systems can be very tedious, and we think that new methods will be required in order to control larger systems.

In chapter 5, we presented a known twirling certification protocol [66] and showed how it can be used to measure the average fidelity of Cliffords. Following this, we presented the usual statistical analysis to obtain bounds for the accuracy of this method. We also presented our own Monte Carlo approach in order to further investigate the accuracy of twirling experiments. In addition, we derived equations that relate the statistical accuracy of the twirling protocol to the variance in the diagonal entries of the $\chi$ matrix of the channel to be certified. We also showed how quantum channels with average fidelities that are expected to be high will require less experimental runs to reach a same desired statistical accuracy. We then presented experiments and simulations for certifying the implementation of quantum gates in our 6-spin system. For the 4-qubit subsystem, we were not able to perform the experiments due to a lack of experimental equipment. However, we designed the software to design and analyze such experiments, and performed some simulations as a demonstration that we should be able to perform such experiments in practice. For the 2-qubit subsystem, we performed twirling certification experiments, but without pulse fixing. We obtained an average fidelity of 91% for the implementation of a controlled-NOT gate. This result could be improved significantly by using pulse fixing.

# APPENDICES

# Appendix A

# Strongly-coupled spin-½ pairs

We solve here the case of dipolar coupled spin-½ pairs. We show how one can calculate the NMR spectrum by diagonalizing the natural Hamiltonian. In particular, we can use the equations derived here to verify the experimental parameters obtained in section 3.3.1.

We start by giving the natural Hamiltonian of the system, which is described in section 2.3.2. For a 2-qubit system, the natural Hamiltonian takes the form

$$\mathscr{H}^{nat} = \pi\nu_1 Z_1 + \pi\nu_2 Z_2 + \frac{\pi D}{2}(2Z_1Z_2 - X_1X_2 - Y_1Y_2) + \pi J(Z_1Z_2 + X_1X_2 + Y_1Y_2). \quad \text{(A.1)}$$

In matrix form, the Hamiltonian is block-diagonal,

$$\mathscr{H}^{nat} = \frac{1}{2}\begin{pmatrix} \Omega_A + \omega_A & 0 & 0 & 0 \\ 0 & \Omega_B - \omega_A & \omega_B & 0 \\ 0 & \omega_B & -\Omega_B - \omega_A & 0 \\ 0 & 0 & 0 & -\Omega_A + \omega_A \end{pmatrix}, \quad \text{(A.2)}$$

where

$$\begin{aligned} \Omega_A &= 2\pi(\nu_1 + \nu_2), & \Omega_B &= 2\pi(\nu_1 - \nu_2), & \text{(A.3)} \\ \omega_A &= 2\pi(D + J), & \omega_B &= 2\pi(2J - D). & \text{(A.4)} \end{aligned}$$

We can use using basic methods to diagonalize the Hamiltonian and thus obtain its eigenvalues and eigenvectors. The eigenvalues are given by

$$\begin{aligned} \Omega_1 &= \frac{1}{2}(\Omega_A + \omega_A), & \Omega_2 &= -\frac{1}{2}\omega_A + \frac{1}{2}\sqrt{{\omega_B}^2 + {\Omega_B}^2}, \\ \Omega_4 &= \frac{1}{2}(-\Omega_A + \omega_A), & \Omega_3 &= -\frac{1}{2}\omega_A - \frac{1}{2}\sqrt{{\omega_B}^2 + {\Omega_B}^2}. & \text{(A.5)} \end{aligned}$$

The corresponding eigenvectors are given by

$$|1\rangle = \begin{pmatrix} 1 \\ 0 \\ 0 \\ 0 \end{pmatrix}, \qquad |2\rangle = \begin{pmatrix} 0 \\ \cos\frac{\kappa}{2} \\ \sin\frac{\kappa}{2} \\ 0 \end{pmatrix}, \qquad |3\rangle = \begin{pmatrix} 0 \\ -\sin\frac{\kappa}{2} \\ \cos\frac{\kappa}{2} \\ 0 \end{pmatrix}, \qquad |4\rangle = \begin{pmatrix} 0 \\ 0 \\ 0 \\ 1 \end{pmatrix}, \tag{A.6}$$

where $\kappa$ is defined such that

$$\tan\kappa = \frac{\omega_B}{\Omega_B}. \tag{A.7}$$

With the eigenvalues and eigenvectors of the Hamiltonian, the signal can now be calculated. First, from the eigenvalues we can calculate the signal frequencies keeping in mind that only single-quantum transitions are allowed. We obtain

$$\Omega_{21} = \frac{\Omega_A}{2} + \omega_A - \frac{1}{2}\sqrt{{\omega_B}^2 + {\Omega_B}^2}, \tag{A.8}$$

$$\Omega_{31} = \frac{\Omega_A}{2} + \omega_A + \frac{1}{2}\sqrt{{\omega_B}^2 + {\Omega_B}^2}, \tag{A.9}$$

$$\Omega_{42} = \frac{\Omega_A}{2} - \omega_A + \frac{1}{2}\sqrt{{\omega_B}^2 + {\Omega_B}^2}, \tag{A.10}$$

$$\Omega_{43} = \frac{\Omega_A}{2} - \omega_A - \frac{1}{2}\sqrt{{\omega_B}^2 + {\Omega_B}^2}, \tag{A.11}$$

where

$$\Omega_{rs} := -\Omega_r + \Omega_s. \tag{A.12}$$

Next, the amplitudes can be calculated by applying the approach described in section2.5.2,

$$a_{21} = \frac{1}{2}(1 + \sin\kappa), \tag{A.13}$$

$$a_{31} = \frac{1}{2}(1 - \sin\kappa), \tag{A.14}$$

$$a_{42} = \frac{1}{2}(1 + \sin\kappa), \tag{A.15}$$

$$a_{43} = \frac{1}{2}(1 - \sin\kappa). \tag{A.16}$$

The NMR signal and spectrum can then be obtained by the calculation explained in 2.5.2. One notices that $\kappa = 0$ corresponds to the weak coupling case, for which the amplitudes are all equal. On the other hand, $\kappa = \pi/2$ is the case of magnetic equivalence. The equations derived here can be applied to verify the results of section 3.3.1.

# Bibliography


[1] P. W. Shor. Polynomial-Time Algorithms for Prime Factorization and Discrete Logarithms on a Quantum Computer. *SIAM Journal on Computing*, 26(5):1484-1509, 1997

[2] L. K. Grover. Quantum Mechanics Helps in Searching for a Needle in a Haystack. *Physical Review Letters*, 79(2):325-328, 1997.

[3] T. D. Ladd, F. Jelezko, R. Laflamme, Y. Nakamura, C. Monroe, and J. L. O'Brien. Quantum computers. *Nature*, 464:45-53, 2010.

[4] R. Das, R. Bhattacharyya, and A. Kumar. Quantum information processing by NMR using a 5-qubit system formed by dipolar coupled spins in an oriented molecule. *Journal of Magnetic Resonance*, 170:310-321, 2004.

[5] C. S. Yannoni, M. H. Sherwood, D. C. Miller, I. L. Chuang, L. M. K. Vandersypen, and M. G. Kubinec. Nuclear magnetic resonance quantum computing using liquid crystal solvents. *Applied Physics Letters*, 75(22):3563, 1999.

[6] T. S. Mahesh, N. Sinha, A. Ghosh, R. Das, N. Suryaprakash, M. H. Levitt, K. V. Ramanathan, and A. Kumar. Quantum information processing by NMR using strongly coupled spins. *Current Science*, 932:85, 2003.

[7] M. H. Levitt. *Spin Dynamics: Basics of Nuclear Magnetic Resonance*. 2nd edition, John Wiley & Sons Ltd, 2008.

[8] I. S. Oliveira, T. J. Bonagamba, R. S. Sarthour, J. C. C. Freitas, and E. R. deAzevedo. *NMR Quantum Information Processing*. Elsevier, 2007.

[9] N. Khaneja, T. Reiss, C. Kehlet, T. Schulte-Herbruggen, and S. J. Glaser. Optimal Control of Coupled Spin Dynamics: Design of NMR Pulse Sequences by Gradient Ascent Algorithms. *Journal of Magnetic Resonance*, 172:296-305, 2005.

[10] J. Dodd, M. Nielsen, M. Bremner, and R. Thew. Universal quantum computation and simulation using any entangling hamiltonian and local unitaries. *Physical Review A*, 65(4):040301, 2002.

[11] C. A. Ryan. *Characterization and Control in Large Hilbert Spaces*. PhD thesis, University of Waterloo, 2008.

[12] M. Nielsen, and I. Chuang. *Quantum Computation and Quantum Information*. Cambridge University Press, 2000.

[13] E. M. Fortunato, M. A. Pravia, N. Boulant, G. Teklemariam, T. F. Havel, and D. G. Cory. Design of strongly modulating pulses to implement precise effective Hamiltonians for quantum information processing. *Journal of Chemical Physics*, 116:7599, 2002.

[14] N. Suryaprakash. Structure of molecules by NMR spectroscopy using liquid crystal solvents. *Concepts in Magnetic Resonance*, 10(3):167-192, 1998.

[15] J. W. Emsley, and J. C. Lindon. *NMR Spectroscopy using Liquid Crystal Solvents*. Pergamon Press, 1975.

[16] S. Castellano, and A. A. Bothner-By. Analysis of NMR Spectra by Least Squares. *Journal of Chemical Physics*, 41(12):3863, 1964.

[17] T. S. Mahesh, and D. Suter. Quantum-information processing using strongly dipolar coupled nuclear spins. *Physical Review A*, 74(6):062312, 2006.

[18] S. Arumugam, A. C. Kunwar, and C. L. Khetrapal. NMR spectrum of benzo[b]furan in a nematic phase. *Organic Magnetic Resonance*, 18(3):157-158, 1982.

[19] S. Berger, and S. Braun. *200 and more NMR experiments*. Wiley-VCH, 2004.

[20] P. Diehl, H. P. Kellerhals, and E. Lustig. *NMR Basic Principles and Progress*, vol. 6. Springer-Verlag, 1972.

[21] J. Vogt. *ASPECT 2000 NMR simulation/iteration PANIC*. Bruker Report, part 3:23-25, 1979.

[22] P. Diehl, H. P. Kellerhals, and W. Niederberger. The structure of toluene as determined by NMR of oriented molecules. *Journal of Magnetic Resonance*, 4(3):352-357, 1971.

[23] S. S. Golotvin, and V. A. Chertkov. Pattern recognition of the multiplet structure of NMR spectra. *Russian Chemical Bulletin* (English Translation), 46(3):423-430, 1997.

[24] O. Manscher, K. Schaumburg, and J. P. Jacobsen. A Discussion of the Error Analysis in LAOCOON-like Iterative Programs. *Acta Chemica Scandinavia*, A35:13-24, 1981.

[25] P. Diehl, S. Sýkora, and J. Vogt. Automatic analysis of NMR spectra: An alternative approach. *Journal of Magnetic Resonance*, 19(1):67-82, 1975.

[26] R. Laatikainen. Automated analysis of NMR spectra. *Journal of Magnetic Resonance*, 92(1):1-9, 1991.

[27] R. Laatikainen. Dipolar coupling and solvent dependence of 1H, 1H spin-spin coupling in naphthalene. analysis of spectra containing overlapping lines. *Journal of Magnetic Resonance*, 78(1):127-132, 1988.

[28] C. Glidewell, D. W. H. Rankin, and G. M. Sheldrick. Analysis of the proton magnetic resonance spectra of phenol and thiophenol and their methyl, silyl and germyl derivatives. *Transaction of the Faraday Society*, 65:2801-2805, 1969.

[29] J. Heinzer. Iterative least-squares nmr lineshape fitting with use of symmetry and magnetic equivalence factorization. *Journal of Magnetic Resonance*, 26:301-316, 1977.

[30] D. S. Stephenson, and G. Binsch. Automated analysis of high-resolution NMR spectra. I. Principles and computational strategy. *Journal of Magnetic Resonance*, 37(3):395-407, 1980.

[31] D. S. Stephenson, and G. Binsch. The molecular structure of cyclopentene in solution as obtained from a nematic phase proton N.M.R. study. *Molecular Physics*, 43:697-710, 1981.

[32] G. Hägele, M. Engelhardt, and W. Boenigk. *Simulation und Automatisierte Analyse von Kernresonanzspectren*. VCH, 1987.

[33] V. N. Zinin, A. V. Il'yasov, U. Weber, G. Hägele, and H. Thiele. The 19F NMR spectrum of bis-trifluoromethylmercury Hg(CF3)2 in the nematic phase: DAISY - a novel program system for the analysis and simulation of NMR spectra. *Journal of Fluorine Chemistry*, 70(2):289-292, 1995.

[34] S. V. Zubkov, and V. A. Chertkov. Experimental Determination of Pseudorotation Potentials for Disubstituted Cyclopentanes Based on Spin-Spin Coupling Constants. *International Journal of Molecular Sciences*, 4(3):107-118, 2003.

[35] H. Takeuchi, K. Inoue, Y. Ando, and S. Konaka. Efficient Method to Analyze NMR Spectra of Solutes in Liquid Crystals: The Use of Genetic Algorithm and Integral Curves. *Chemical Letters*, 11:1300-1301, 2000.

[36] J. A. Hageman , R. Wehrens, R. de Gelder, W. Leo Meerts, and L. M. C. Buydens. Direct determination of molecular constants from rovibronic spectra with genetic algorithms. *Journal of Chemical Physics*, 113(18):7955, 2000.

[37] W. Leo. Meerts, C. A. de Lange, A. C. J. Weber, and E. E. Burnell. A simple two-step automatic assignment procedure for complicated NMR spectra of solutes in liquid crystals using genetic algorithms. *Chemical Physics Letters*, 441:342-346, 2007.

[38] Ronald Y. Dong. *Nuclear magnetic resonance spectroscopy of liquid crystals*. World Scientific Publishing Company, 2009.

[39] W. Leo. Meerts, C. A. de Lange, A. C. J. Weber, E. E. Burnell. Evolutionary algorithms to solve complicated NMR spectra. *Journal of Chemical Physics*, 130(4):044504, 2009.

[40] H. Oschkinat, A. Pastore, P. Pfändler, and G. Bodenhausen. Two-dimensional correlation of directly and remotely connected transitions by z-filtered COSY. *Journal of Magnetic Resonance*, 69(3):559-566, 1986.

[41] R. C. R. Grace, N. Suryaprakash, A. Kumar, and C. L. Khetrapal. Application of a Modified Z-COSY Experiment for the Analysis of Spectra of Oriented Molecules - The Spectrum of cis,cis-Mucanonitrile. *Journal of Magnetic Resonance*, 107(1):79-82, 1994.

[42] P. Mansfield. Symmetrized pulse sequences in high resolution NMR in solids. *Journal of Physics C*, 4(11):1444, 1971.

[43] P. Mansfield, M. J. Orchard, D. C. Stalker, K. H. B. Richards. Symmetrized Multipulse Nuclear-Magnetic-Resonance Experiments in Solids: Measurement of the Chemical-Shift Shielding Tensor in Some Compounds. *Physical Review B*, 7(1):90-105, 1973.

[44] W.-K. Rhim, D. D. Elleman, and R.W. Vaughan. Analysis of multiple pulse NMR in solids. *Journal of Chemical Physics*, 59(7):3740, 1973.

[45] M. K. Henry, C. Ramanathan, J. S. Hodges, C. A. Ryan, M. J. Ditty, R. Laflamme, and D. G. Cory. Fidelity Enhancement by Logical Qubit Encoding. *Physical Review Letters*, 99(22):220501, 2007.

[46] J. Zhang, M. Ditty, D. Burgarth, C. A. Ryan, C. M. Chandrashekar, M. Laforest, O. Moussa, J. Baugh, and R. Laflamme. Quantum data bus in dipolar coupled nuclear spin qubits. *Physical Review A*, 80(1):012316, 2009.

[47] L. D. Field. Multiple Quantum NMR of Partially Aligned Molecules. *Annual Reports on NMR Spectroscopy*, 59:1-39, 2006.

[48] B. Baishya, and N. Suryaprakash. Spin State Selective Detection of Single Quantum Transitions Using Multiple Quantum Coherence : Simplifying the Analyses of Complex NMR Spectra. *Journal of Physical Chemistry A*, 111:5211-5217, 2007.

[49] D. Burgarth, K. Maruyama, and F. Nori. Coupling strength estimation for spin chains despite restricted access. *Physical Review A*, 79(2):020305(R), 2009.

[50] K. Maruyama, D. Burgarth, A. Ishizaki, K. B. Whaley, and T. Takui. Hamiltonian tomography of dissipative systems under limited access: A biomimetic case study. arXiv:1111.1062v1 [quant-ph].

[51] E. H. Lapasar, K. Maruyama, D. Burgarth, T. Takui, Y. Kondo, and M. Nakahara. stimation of Coupling Constants of a Three-Spin Chain: Case Study of Hamiltonian Tomography with NMR. arXiv:1111.1381v1 [quant-ph].

[52] J. Nocedal, and S. J. Wright. *Numerical Optimization*. 2nd edition, Springer, 2006.

[53] C. Audet, and J. E. Dennis Jr. Analysis of Generalized Pattern Searches. *SIAM Journal of Optimization*, 13(3):889-903, 2003.

[54] T. F. Coleman, and Y. Li. An Interior Trust Region Approach for Nonlinear Minimization Subject to Bounds. *SIAM Journal of Optimization*, 6(2):418-445, 1996.

[55] A. J. Shaka, P. B. Barker, and R. Freeman. Computer-optimized decoupling scheme for wideband applications and low-level operation. *Journal of Magnetic Resonance*, 64(3):547-552, 1985.

[56] T. Bräuniger, P. Wormald, and P. Hodgkinson. Improved proton decoupling in NMR spectroscopy of crystalline solids using the SPINAL-64 sequence. *Monatshefte für Chemie*, 133(2):1549-1554, 2002.

[57] C. B. Moler, and G. W. Stewart. An Algorithm for Generalized Matrix Eigenvalue Problems. *SIAM Journal on Numerical Analysis*, 10(2):241-256, 1973.

[58] R. G. Mavinkurve, H. S. V. Deepak, K. V. Ramanathan, and N. Suryaprakash. Analyses of the complex proton NMR spectra: Determination of anisotropic proton chemical shifts of oriented molecules by a two dimensional experiment. *Journal of Magnetic Resonance*, 185(2):240-246, 2007.

[59] M. Lee, and W. I. Goldburg. Nuclear-Magnetic-Resonance Line Narrowing by a Rotating rf Field. *Physical Review A*, 140(4):1261-1271, 1965.

[60] C. A. Ryan, C. Negrevergne, M. Laforest, E. Knill, and R. Laflamme. Liquid-state nuclear magnetic resonance as a testbed for developing quantum control methods. *Physical Review A*, 78:012328, 2008.

[61] J. F. Poyatos, J. I. Cirac, and P. Zoller. Complete characterization of a quantum process: The two-bit quantum gate. *Physical Review Letters*, 78:390-393, 1997.

[62] I. L. Chuang, and M. A. Nielsen. Prescription for experimental determination of the dynamics of a quantum black box. *Journal of Modern Optics*, 44(11):2455-2467, 1997.

[63] J. Emerson, R. Alicki, and K. Zyczkowski. Scalable noise estimation with random unitary operators. *J. Opt. B: Quantum and Semiclassical Optics*, 7:S347-S352, 2005.

[64] C. Dankert, R. Cleve, J. Emerson, and E. Livine. Exact and approximate unitary 2-designs: constructions and applications. *Physical Review A*, 80(1):012304, 2009.

[65] M. P. da Silva. *Suppression and characterization of decoherence in practical quantum information processing devices*. PhD thesis, University of Waterloo, 2008.

[66] O. Moussa, M. P. da Silva, C. A. Ryan, and R. Laflamme. Practical experimental certification of computational quantum gates using a Twirling procedure. *Physical Review Letters*, 109(7):070504, 2012.

[67] J. Emerson, M. P. da Silva, O. Moussa, C. A. Ryan, M. Laforest, J. Baugh, D. G. Cory, R. Laflamme. Symmetrized characterization of noisy quantum processes. *Science*, 317(5846):1893-1896, 2007.

[68] S. S. Venkatesh. *The Theory of Probability: Explorations and Applications*. Cambridge University Press, 2012.